

In fond memory of

my granny Parvathamma

.....who funded my Amateur Astronomy

Near Infrared Investigations on Regions of Star Formation

**A Thesis Submitted to
The Gujarat University
for**

**THE DEGREE OF DOCTOR OF PHILOSOPHY
in
PHYSICS**

by

M. S. Nanda Kumar

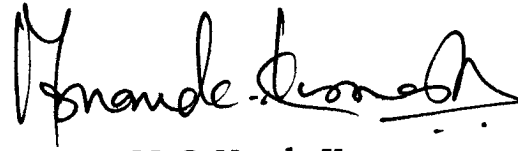
**पुस्तकालय THE LIBRARY
भौतिक अनुसंधान प्रयोगशाला
PHYSICAL RESEARCH LABORATORY
नवरंगपुरा, अहमदाबाद-380 009
NAVRANGPURA, AHMEDABAD-380 009
भारत / INDIA**

**PHYSICAL RESEARCH LABORATORY
NAVRANGPURA
AHMEDABAD 380 009
INDIA**

September 1999

CERTIFICATE

I hereby declare that the work presented in this thesis is original and has not formed the basis for the award of any degree or diploma by any University or Institution.



M. S. Nanda Kumar

(Author)

**Astronomy and Astrophysics Division
Physical Research Laboratory
Navrangpura
Ahmedabad - 380 009
India**

CERTIFIED BY



Prof. B. G. Anandarao

(Thesis Supervisor)

**Professor
Astronomy and Astrophysics Division
Physical Research Laboratory
Navrangpura
Ahmedabad - 380 009
India**

Contents

Acknowledgements	iv
1 Introduction	1
1.1 Star Formation and Near-IR Astronomy	1
1.2 Basic Physics of Star formation	3
1.3 Observational aspects of star forming regions	7
1.3.1 Molecular clouds, clumps and cores	7
1.3.2 Protostars and T Tauri stars	9
1.3.3 Jets & Outflows from YSO's	12
1.3.4 Disks and Unified models	15
1.3.5 Pre-Main-Sequence Companions	16
1.4 References	17
2 Observations and data reduction	20
2.1 The Near-Infrared Sky	21
2.2 PRL Near Infrared Camera: PRLNIC	22
2.2.1 Camera Operating Software	25
2.3 Black Magic for the Black Box: PRLNIC	26
2.3.1 The Problem	26
2.3.2 The Solution	27
2.4 Observation and Data Reduction Procedures	28
2.4.1 Imaging Mode	28
2.4.2 Spectroscopy	31
2.5 Future efforts	33
2.6 References	36
3 Cold Disk Structures in Protostellar Envelopes	37

3.1	Introduction	37
3.2	The L43 dark cloud	38
3.2.1	The CO outflow in L43	39
3.2.2	L43 dense core	41
3.3	RNO 90: A T Tauri Star in L43	43
3.4	Shocked molecular hydrogen from RNO 91	45
3.4.1	Observations and Data Reduction	46
3.4.2	Results	47
3.4.3	Discussion	50
3.5	RNO 91 disk/outflow	53
3.6	Future Work	58
3.7	Summary and Conclusions	60
3.8	References	61
4	Warm and Hot Disk Structures in Protostellar Envelopes	64
4.1	Introduction	64
4.2	The Sample Set	65
4.3	Infrared Spectroscopy of YSO's	66
4.4	Results and Discussion	68
4.4.1	FS Tau	70
4.4.2	DG Tau	72
4.4.3	GM Aurigae	73
4.4.4	DL Tau	74
4.4.5	DO Tau	75
4.4.6	CY Tau	75
4.4.7	V836 Tau	75
4.5	Conclusions	76
4.6	References	77
5	L1340 : A star forming cloud	79
5.1	Introduction	79

5.2	Observations and Data Reduction	80
5.3	L1340 cloud and the Cohen's objects	81
5.3.1	RNO7	82
5.3.2	RNO8	83
5.3.3	RNO9	84
5.4	New Herbig-Haro Objects in L1340	95
5.4.1	HH487	96
5.4.2	HH488	96
5.4.3	HH489	98
5.5	Conclusions	105
5.6	References	106
6	A Near Infrared Imaging Fabry-Perot Spectrometer	107
6.1	Introduction	107
6.2	The Fabry-Perot Interferometer	108
6.3	Imaging Fabry-Perot Spectrometers	110
6.3.1	Scanning and phase correction	111
6.3.2	Wavelength Calibration	113
6.4	Astronomical Observations with an IFPS	114
6.5	Telecentric Configuration	115
6.6	Telecentric vs Classical Configuration	116
6.7	PRL Infrared FP Etalon	117
6.7.1	Characterization	118
6.7.2	Tuning of the FP	119
6.8	Observations and data analysis	120
6.9	High-Resolution Spectrophotometric Imaging in Emission Lines - NIRFPS as a Tunable Filter	122
6.10	References	124
	Epilogue	125
	List of Publications	128

Acknowledgements

This moment of writing the acknowledgements brings to me a strange feeling of happiness and sadness. The happiness of becoming an independent researcher entering an inviting world where there is so much to do....and the sad feeling of having to leave PRL along with a family of teachers and well-wishers who always took the responsibility for whatever I did.

I couldn't be luckier to work with a thesis advisor like Anandarao who has been my 'friend, philosopher and guide' in its true meaning. I have enjoyed every moment of my research career at PRL in working with him during the last 4 years. Being a great self-critic, he has taught me the lesson of self-criticism, which is necessary to a great extent in an independent researcher's life, at every moment of our interaction. His systematic way of working bugs me even today, pointing to my hasty nature. I have learnt a lot from him, particularly the intricacies of Fabry-Perot Interferometers. I am happy to be continuing a scientific collaboration with him after the thesis work.

My first guru at PRL, J.N. Desai, has always been a great source of inspiration to me. A born-scientist, JND has a knack for explaining basic physics in an easily imaginable way. Not bugging his students with mathematical formulae, he can still explain concepts without leaving away the subtle details and depth.

I have greatly profited by scientific interactions with Bo Reipurth, CASA, Colorado, USA, and Rafael Bachiller, OAN, Spain. I am very grateful for their interest in my work and for sharing their observing time to obtain data for my thesis. Collaboration with Chris Davis, JAC, Hawaii, USA, has been very successful and encouraging. I have enjoyed a great company with Dr. A. R. Rao, TIFR, Mumbai, who

has been an infinite source of encouragement and criticism to my academic career and life in general.

I thank N. M. Ashok and T. Chandrashekhar for their interest in my work and for an enjoyable company during the solar eclipse campaign at Neem Ka Thana. They have been very cordial and friendly throughout my stay here. I thank U. C. Joshi for his cordial nature and cooperation as Chairman of the Division. I thank all the staff of PRL for a very friendly and helpful association during the last 6 years. I have enjoyed every moment of my interaction with the workshop staff, particularly A. J. Shroff, Jadhavbhai and Atmarambhai. They have worked with great enthusiasm and on overtime during the fabrication of Fabry-Perot Interferometers and the Coupling unit of the IR camera. I thank our librarians, Uma Desai and Rohini Patil, for their pleasant cooperation in library matters. I thank G. G. Dholakia for all the help at the computer center.

Visits to Gurushikhar for making the observations was always a matter of great pleasure and excitement. The wonderful company of Raj Purohit, A. H. Desai and J. K. Jain during night observing runs has left a pleasant memory. I gratefully thank Patelji for his tireless help in preparing for observations and also for a nice company at all times. Mr. Rajesh Shah's interesting nature and his commitment to work at Gurushikhar never failed to win when the telescope and electronics decided to go on strike. All the staff at Mt. Abu along with several people who work on contract with PRL for transport and maintenance, made the observing trips a pleasing experience. I thank Aparna, Ashish Mahabal, Ashish Karnik (TIFR) for "tips" on IRAF, Sagar Pandit and Sai Krishna Rao for "tips" on anything related to computers.

Personal life and the state of mind greatly influences one's working life. I feel privileged to have enjoyed a very exciting and happy life at PRL hostel. I cherish the pleasant memory of several friends; Manoj, Anshu, Sam, Debu (ET), Jyoti (Gorilla), Poulouse (T-Rex), Abhijit (Chacko), Seema, Biju (Handi), Santhanam, Chetan (Gujju), Brajesh, Praveen Mishra (UuP), Ansu, Biswajoy, Avijit (Gangu), Raju, Yadavji,

Shwetketu for their nice company when they were at PRL. I have enjoyed the company of Ratan, Rishi, Watson (Apparam), Siva (Chiva), Tarun, Prashant, Shajesh, Subbu (Hippo), Soumen, Sunish, Ghosh and Hetu (the horrible). I am particularly thankful to Sam and Siva for their care during the times of my illness. Peter was a great company with guitar and otherwise.

Life would have never been the same at PRL without Jitti, Rajesh, Kulbir, Vinai, Sudhir, Rajneesh, Anirban, Anil Shukla, Aparna, Kunu, Alok, Pattu, Dipu, Sankar, Koushik and Mohit. They have always given me a hope to live and win. Jitti's unconditional support and the friendship of Rajesh, Kulbir and Muthu made me feel the safety and comfort of a family althrough. Vinai, Rajneesh and Sudhir have given me tremendous moral support during the last year. Anil Shukla was ever ready to help, and Dipu's witty arguments never failed to cheer me up. Pattu baby and Anirban have been very affectionate to me. Kunu and Aparna have been very caring and I am priviliged to have their affection. Kamath was the most reliable source of support when needed and was with me during my low times. I thank Sarika and Sanjay for their cheerful company.

I thank Mrs. Janaki Anandaraao, Mrs. Aruna Ashok and Mrs. Vimal Parthasarathy (my music teacher), for nice parties on several occassions.

My personality has been greatly influenced by my teachers and friends who have brought positive changes to my life. S. N. Prasad and A. Venny showed me the exciting world of stars. G. Ramachandran, A. V. Gopalarao, K. S. Mallesh and M. K. Vishwanath have been inspiring teachers who made physics so lively a subject. My family along with Sanjay, Anand and Prasad are supporting pillars to my existence, those who love me and pray for my well-being.

Finally, I appreciate the perseverance of several corrupt and greedy elements, who have entered into the holy world of Scientific Institutions, for keeping my "killer instincts" alive.

Introduction

1.1 Star Formation and Near-IR Astronomy

Even as we enter the next millenium, star and planet formation continues to be a challenging problem in astrophysics. The advent of near-infrared focal plane arrays in the last decade made a huge impact on our understanding of the star formation phenomenon. Near-infrared (NIR) cameras have made it possible to study large areas of star forming regions at high spatial resolutions with a high signal to noise ratio. This has resulted in detailed study of many observational aspects of star formation leading to verification of theories of low mass star formation (low mass stars $\sim 1 M_{\odot}$). Recent “All sky surveys” in the NIR bands have also been possible (2MASS, DENIS) due to the availability of large format focal plane arrays, which has resulted in a census of star formation in the clouds of L1630, Taurus-Auriga, Ophiuchus, and several other well known sites of star formation. It is important to note that star forming regions are some of the brightest infrared sources in the sky. Soon after the advent of infrared focal plane arrays, studies of low mass star formation took the first priority in receiving the attention of researchers, mainly because it provides a zoo of observables in the sky. The time scales involved in the formation of a low mass star is of the order of $\sim 10^6$ yrs which makes it possible to catch the various stages of star formation as an observable phenomenon in the sky. In comparison, the high mass star formation is more rapid ($\sim 10^5$ yrs) and it is therefore difficult to observe the various stages of the high mass star formation in the sky. In the last one decade, this resulted in an enormous amount of data to

gas column densities are constant (self-similarity). This property of GMC's reflects on the fact that as it breaks into smaller and smaller pieces, the physical nature of the clouds remains the same as it originally was. By observations, it is known that GMC's are filamentary in nature. One of the important questions that arises is that if clouds are self-similar then what is the smallest entity in a molecular cloud that finally begins to collapse to form a protostar and what is its size? Recent work by Borranco et al. (1998) and Goodman et al. (1998) has shown that the smallest non-self-similar entity in a molecular cloud is a dense core of sizes $\sim 0.1\text{pc}$ and such cores collapse to form an individual star. Reference to this work will be made again in *Chapters 4 and 5*.

1.3.2 Protostars and T Tauri stars

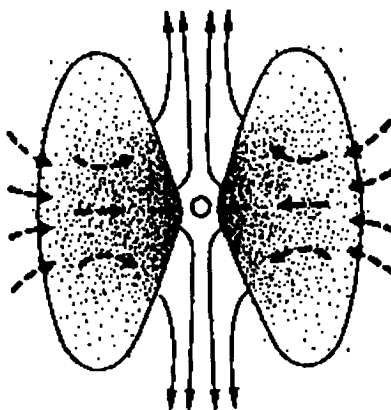
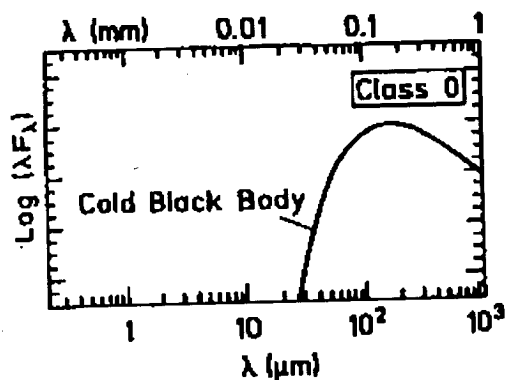
One of the challenges in star formation studies has been to detect the youngest objects possible, so that various phenomena related to infall and collapse could be studied. In an attempt to identify the youth of the candidates for Young Stellar Objects (YSO's), Charles Lada classified them for the first time (Lada & Wilking 1984, Lada 1987) based on their spectral energy distribution (SED) in the infrared wavebands longward of $2\mu\text{m}$ (see Fig 1.1). This was possible mainly because of the availability of the IRAS data for a large number of protostellar sources in the sky. According to his classification, the spectral index, defined in the range longward of $2\mu\text{m}$, as

$$\alpha = \frac{-d\log(\nu F_\nu)}{d\log\nu} \quad (1.6)$$

is positive for the Class I sources, zero or negative for the Class II sources and negative for the Class III sources. The Class I sources peak at $60\text{-}100\mu\text{m}$ and have a SED broader than the black body, with little or no radiation in the near-infrared. These objects are also called embedded sources or protostars and are strongly enshrouded by dust. The Class II sources mostly fall into the class of Classical T Tauri stars (CTTS) and have significant IR and UV excess, they have less circumstellar dust and are known to be associated with jets and disks. The Class III sources have a

photospheric emission spectrum close to that of a single black body and there is no evidence for excess IR radiation. These sources mostly fall into the class of Naked T Tauri stars (NTTS) (Walter 1987) and pre-mainsequence stars.

In the study of protostars the presence or otherwise of two important signatures needs to be proved. Firstly, they should be deriving the luminous energy by the infall kinetic energy indicating the extreme youth of the protostar. Secondly, proof has to be obtained for ongoing infall which comes from the identification of an inverse P-Cygni profile of the emission line observed from the source. Recently it has been pointed out by Andre et al. (1993) that the Class I protostars do not actually derive their luminous energy from kinetic energy of the infall. These authors have identified an earlier stage of objects called the Class 0 protostars that derive their luminous energy by the infall kinetic energy and also show strong signatures of infall. One conspicuous quality of the Class 0 protostars is that their submm luminosities (measured at $350\mu\text{m}$) are higher than their bolometric luminosities. This indicates that a large fraction of the mass is still present in the form of infalling dust and gas, that is traced by the submm emission. On the other hand CTTS and WTTS are optically visible stars. CTTS are strongly characterized by their lithium emission line and the "veiling" of the photospheric features in the blue region of the spectrum. In the near-infrared, they have strong $\text{Br}\gamma$ emission that was thought to arise from disk winds but is now proved to arise from infall in a magnetosphere (Najita et al. 1996) (see Fig 1.3). These stars possess optically thick disks, and are the best candidates to study the dusty circumstellar disks along with associated jets, to obtain an understanding of jet/disk connection. Microjets (Solf 1987) arising from these stars emit strongly in the forbidden emission lines, and are important in the studies of jet/disk relationship. The WTTS are stars with optically thin disks and are believed to have planetary systems that have already formed. These are predicted to be the potential sites to look for new planets.

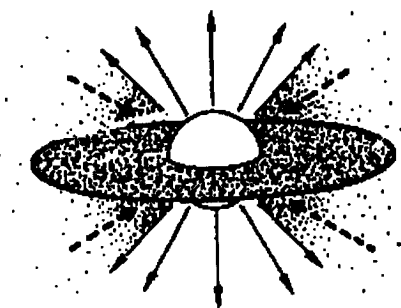
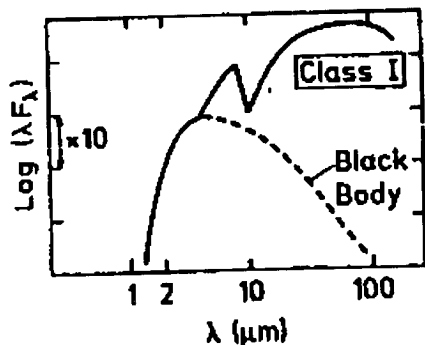


CLASS 0:

*Main
accretion
phase?*

Age $\leq 10^4$ yr

$M_{\text{CS}} \geq 0.5 M_{\odot}$

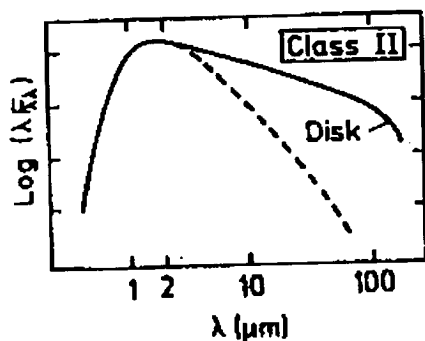


CLASS I:

*Late
accretion
phase?*

Age $\sim 10^5$ yr

$M_{\text{CS}} \leq 0.1 M_{\odot}$

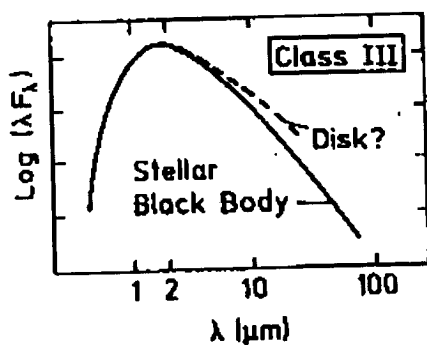


CLASS II:

*Optically
thick
disk*

Age $\sim 10^6$ yr

$\langle M_{\text{disk}} \rangle \sim 0.01 M_{\odot}$



CLASS III:

*Optically
thin
disk?*

Age $\leq 10^7$ yr

$\langle M_{\text{disk}} \rangle < 0.003 M_{\odot}$

Figure 1.1: Spectral Energy Distributions of YSO's from Andre et al. 1993

1.3.3 *Jets & Outflows from YSO's*

The discovery of emission line nebulosities around young stars in the L1630 cloud by Herbig (1951) and Haro (1952) led to the study of mass loss phenomenon in young stars. These nebulosities are now known to be regions of shocked material around young stars and are called the Herbig-Haro objects. It was soon realised that these shocked regions are due to high velocity stellar winds originating from a young star. The discovery of high velocity CO line emission from the nearby molecular clouds and the study of the emission morphology revealed that the high velocity winds associated with the HH objects are traced out by the CO lines and shown to be bipolar in nature (Snell et al. 1980, Rodriguez et al. 1980). Excellent reviews on this topic can be found in Lada (1985) and Bachiller (1996). The different components of the outflow material are traced mainly by emission lines in the millimeter (molecular component), infrared (molecular) and optical (ionized component) wavelengths. Most of the mass in the outflow is traced by the emission lines of CO isotopes indicating that the outflow mass is mainly residing in the molecular component. Generally the outflows are collimated and have standard velocities (a few km/sec to 20km/sec), but there also exist highly collimated, poorly collimated and extremely high velocity(EHV) outflows (Bachiller 1996). They are generally believed to be driven by highly collimated jets that are seen in near-infrared and optical emission lines. Molecular outflows provide estimates on the mass loss rates from the young star and also an idea of the energy that goes out of the system. The size and velocity of the outflows allow us to estimate the age of these outflows which can then be compared with the age of their driving sources. It has been noticed that the maximum outflow activity is associated with the Class 0 protostars as driving sources (Bachiller 1996).

The optical counterparts of collimated outflows are referred to as jets and were discovered by Mundt and Fried (1983). They are called also as the HH jets since the emission from these jets is similar to that seen in the HH objects. Infact the HH objects are emission nebulosities associated with bipolar outflows, like, the

jets, knots and bowshocks. These objects emit in the emission lines indicative of shocked material, the strongest lines being that of the sulphur [SII] (6717\AA and 6736\AA) and $H\alpha$. Studies of the morphology of jets, their collimation factors (the length to width ratio) can indirectly tell us about the physical processes involved in their formation and collimation. Optical jets have collimation factors ranging from 5 to 30 (see Reipurth 1990). The jets are made up of several knots, working surfaces and they terminate in a bowshock. The knots and multiple bowshocks in a single jet indicate that the mass loss is an episodic phenomenon. The size of the jet combined with its proper motion data allows an estimate of the age of the jet as in the case of outflows. The proper motions also help us understand the homogeneity of the surrounding medium and also the tilt angles of these bipolar outflows. This is due to the fact that the two lobes of the jet/outflow plough into two different media and the way they propagate will tell us about the medium itself. As mentioned earlier, a majority of CTTS have microjets associated with them, that extend from less than $1''$ to a few arcseconds from the star. Longslit spectroscopy with the slit placed along the outflow axis can reveal these microjets in the forbidden emission lines allowing kinematic studies (Solf 1987, Hirth et al. 1997). Infrared counterparts of HH jets/bowshocks/knots appear strongly in the emission of the shocked molecular hydrogen at $2.122\mu\text{m}$ and very weakly in the [FeII] emission at $1.645\mu\text{m}$ (Davis & Eisloffel 1995). An excellent example of a pulsed near-infrared jet is HH212 (Zinnecker et al. 1997) which happens to be the best text book example of a near-IR flow. Another class of HH flows identified as giant HH flows or parsec scale flows carry the history of the driving source and its evolution (Reipurth et al. 1998). The parsec scale flows have “S” and “C” shaped symmetries that correspond to the wobbling motion and translation of the driving sources with respect to the parent cloud. Eisloffel & Mundt (1997) have shown similar effects for parsec scale HH jets. Such large scale flows are also believed to pump in a lot of turbulence into the surrounding medium of the young star and may help initiate further star formation.

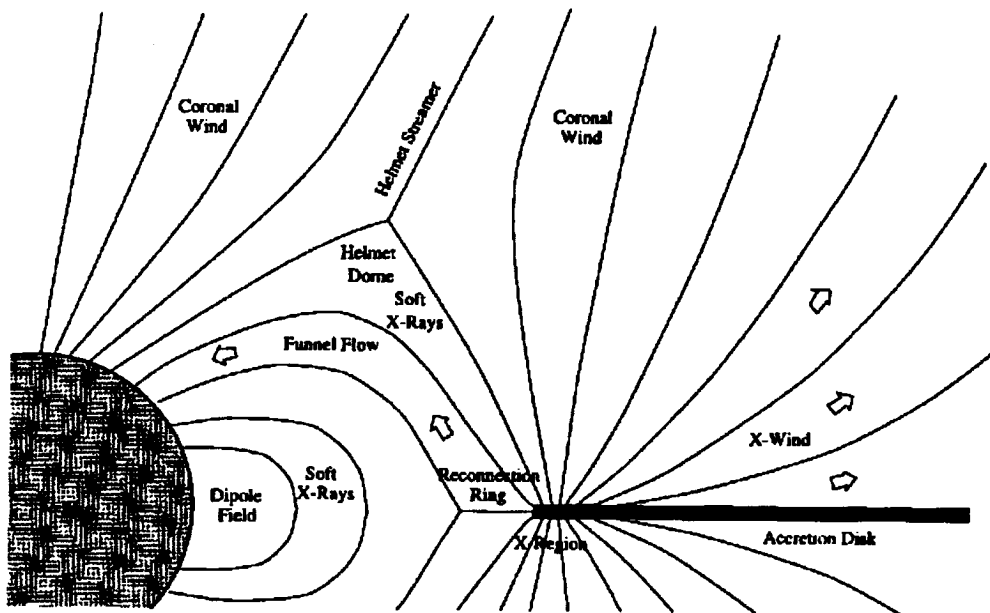


Figure 1.2: Schematic drawing of the X-wind model from Shu, F. H. & Shang, H., 1997, in Eds: Reipurth, B., & Bertout, C., IAU 187 Symposium proceedings, Kluwer Pub. Netherlands

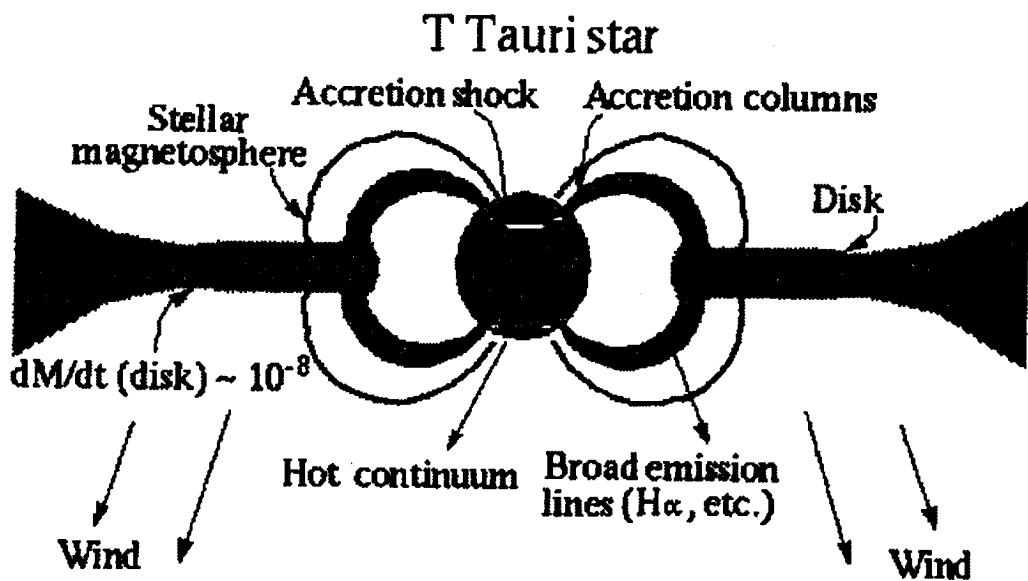


Figure 1.3: Schematic of an accreting T Tauri Star from Hartmann, L., 1997, in Eds: Reipurth, B., & Bertout, C., IAU 187 Symposium proceedings, Kluwer Pub. Netherlands

1.3.4 Disks and Unified models

The amount of information obtained about mass loss from young stars through studies of outflows have to be understood in an unifying theory that explains disks, jets, winds and the evolution of a protostar. Although it was not possible to spatially resolve the disks until recently by millimeter wave interferometers and HST, their existence was inferred by several indirect methods. Important contributions and surveys were made nearly a decade ago (Beckwith et al. 1990). Several basic properties of the disks like mass, temperature and limits on their sizes were estimated using these earlier methods.

The first important fact that has come through the studies of outflows and protostars is that the energetics involved in outflows and accretion process are comparable. The forbidden line emission associated with the outflows from T Tauri stars is seen only from those stars that have near-IR excess which is attributed to disks (See *Chapter 5*). Along with outflows that are known to be ubiquitous among YSO's, disks are also very frequent (80%) in YSO's. The existence of neutral winds in some sources suggests that outflows may not originate from a hot photosphere but from a disk. It is now fairly clear that the circumstellar disks are the energy storage reservoirs that drive the outflows. Several models have been suggested to explain the star/disk/jet connection and the most popular of them is by Shu et al. (1994) called the X-celerator model (see Fig 1.2). According to this model the jet originates at a boundary layer between the disk and the star called the X point. The energy reservoir is due to the stored magnetic energy, angular momentum and the thermal heating from the UV radiation of the star. The model suggests that the energy is transferred to particles at this point which are then flung outwards along the magnetic field lines. The particles are described to be "beads" guided along the threads of magnetic field lines. The theory became popular ever since X rays were discovered from YSO's, since the generation of X rays was predicted at the X point. The mass is supposed to continue to accrete onto the star through funnel flows from the disk.

1.3.5 *Pre-Main-Sequence Companions*

Although it appeared, with the X-celerator model, that there is a unified theory which explained nearly all the observed phenomena of protostars, jets and disks, potential new problems have been pointed out that need to be addressed by theoretical models. It is now well known that nearly 50% of the young stars are binaries (Beckwith et al. 1990). Recent surveys in nearby star forming regions have demonstrated the existence of binaries in young low-mass pre-main-sequence stars. If the young binaries are not identified, then the masses and ages of the binary systems can be substantially misjudged, causing errors in the determination of the Stellar Initial Mass Function and the reconstruction of the star formation history (Zinnecker and Brandner 1997). There have been a class of companions to visible T Tauri stars, called Infrared Companions (IRC's) (Herbst et al. 1995, Koresko et al. 1997). IRC's, as the name suggests, are companions which are invisible or just barely visible in the optical and bright in the infrared. Their brightness in the infrared is attributed to ongoing accretion and is proven by the detection of shocked molecular hydrogen emission in their spectrum (see *Chapter 5*). These facts make it evident that the young companions form prior to the pre-main sequence stage which argues against the random pairing of the field stars and therefore in favour of correlated formation that needs to be explained by models. Further, it is noticed that pairs of non-oriented jets arise from young sources which are putative binaries (Gredel and Reipurth 1993). The misalignment of these jets indicates that the circumstellar disks in binary systems may not always be coplanar. In view of these upcoming evidences, binary formation theories have to be evolved and considerable observational challenges exist in the forth-coming years.

1.4 References

- Andre, P, Ward-Thompson, D., & Barsony, M., 1993, ApJ, 406, 122
- Bok, B. J., 1955, AJ, 60,146
- Bachiller, R., ARAA, 1996, 34, 111
- Beckwith, S. V. W., Sargent, A. I., Chini, R. S., & Gusten, R., 1990, 99, 924
- Borranco, J., & Goodman, A. A., 1998, ApJ, 504, 207
- Dame, T. M., Elmegreen, B. G., Cohen, R. S., & Thaddeus, P, 1986, ApJ Letters, 239, L53
- Davis, C. J., & Eisloffel, J., 1995, A&A, 300, 851
- Elmegreen, B. G., 1985, in Eds. Black, D. C., & Matthews, M. S., Protostars and Planets II, p33, Univ. of Arizona. press, Tucson.
- Eisloffel, J., & Mundt, R., 1997, AJ, 114, 280
- Gredel, R., & Reipurth, B., 1993, ApJ Letters, 407, L29
- Goodman, A. A., Barranco, J. A., Wilner, D. J., & Heyer, M. H., 1998, ApJ, 504,223
- Haro, G., 1952, ApJ, 115, 572
- Herbig, G. H., 1951, ApJ, 113, 697
- Herbst, T. M., Koresko, C. D., Leinert, C. 1995, ApJ, 444 , L93
- Hirth, Mundt, R., & Solf, J., 1997, A&ASS, 126, 437
- Koresko, C. D., Herbst, T. M., & Leinert, Ch., 1997, ApJ, 480, 741
- Larson, R. B., 1969, MNRAS, 145, 271
- Lada, C. J., 1985, ARAA, 23, 267

- Lada, C. J., & Wilking, B. A., 1984, ApJ, 287, 610
- Lada, C. J., 1987, in IAU Symp. no. 115, Eds. Peimbert, M., & Jugaku, J., p1, Dodrecht Reidel, Netherlands.
- Mundt, R., & Fried, J. W., 1983, ApJ, 274, L83
- Mckee, C. F., Ellen, G. Zweibel, et al. 1993, in Eds. Levy, E. H., & Lunine, J. I., Protostars and Planets III, p327, Univ. of Arizona press, Tucson.
- Najita, J., Carr, J. S., & Tokunaga, A. T., 1996, ApJ, 456, 292
- Penzias, A. A., Solomon, P. M., Jefferts, K. B., & Wilson, R. W., 1972, ApJ, 174, L43
- Reipurth, B., 1990, in Eds. Lada, C. J., & Kylafis, N., NATO ASI on Star formation and Early Stellar Evolution,
- Reipurth, B., Bally, J., & Devine, D., 1998, AJ, 114, 2708
- Snell, R. L., Loren, R. B., Plambeck, R. L., 1980, ApJL, 239, L17
- Rodriguez, L. F., Ho, P. T. P., Moran, J. M., 1980, ApJL, 240, L149
- Stahler, S., Shu, F. H., Taam, R. E., 1980, ApJ, 241, 637
- Shu, F. H., Adams, F. C., & Lizano, S., 1987, ARAA, 25, 23
- Shu, F. H., Najita, J., Ostriker, E., Wilkin, F., Steven, R., & Lizano, S., 1994, ApJ, 428, 654
- Scoville, N. Z., Yun, M. S., Clemens, D. P., et al. 1987, ApJSS, 63, 821
- Solomon, P. M., Rivolo, A. R., Barret, J., & Yahil, A., 1987, ApJ, 319, 730
- Solf, J., 1987, A&A, 184, 322
- Walter, F. W., 1987, PASP, 99, 31

- Zinnecker, H., & Brandner, W., 1997, in eds. Docobo et al., Visual Double Stars: Formation, Dynamics and Evolutionary Tracks, 115-125, Kluwer Academic Publishers, Netherlands.
- Zinnecker, H., McCaughrean, M. J., & Rayner, J. T., 1998, Nature, 394, 862

Observations and data reduction

This chapter describes the observations and data reduction made with the country's first operational near-IR (NIR) camera PRLNIC. This is also the first document that describes the specific problems and solutions related to observing with PRLNIC. The techniques of NIR imaging and spectroscopic methods are discussed and documented with a special emphasis on methods that are followed while observing with PRLNIC. The data required for this thesis have been obtained from other facilities also. The data included in *Chapter 5* were obtained with CCD's on the 0.9m telescope at Kitt Peak National Observatory, USA, and with 2.3m telescope at Kavalur Observatory, operated by Indian Institute of Astrophysics, India. *Chapter 3* contains data obtained using the IRCAM3 and UFTI infrared cameras on the 3.8m United Kingdom Infrared Telescope, Mauna Kea, Hawaii, USA. The details of such observations and data reduction are described in the relevant chapters.

The techniques of infrared instrumentation and observation have developed rapidly in the last 15 years and there have been a series of books which reflect the various stages of this growth. The first book on infrared techniques with array detectors was the conference proceedings on Infrared Astronomy held at Hawaii, edited by Wynn-Williams and Eric Becklin (1987). Seven years later a similar conference took place by which time major advancements were seen in the field and the proceedings of this conference contains articles covering many basic aspects of the observational methods (McLean 1994). Excellent articles on several studies in astrophysics that were emerging around the detector arrays have been compiled in a book edited by Elston (1991). A set of review articles on the current and future

direction in various fields of astrophysics with NIR techniques, is covered in the book "Infrared Astronomy" edited by Mampaso et al. (1993), and is the outcome of a Canary Islands Astrophysics School. The most recent reference which gives a detailed review of NIR methods and techniques, is the book "Electronic Imaging in Astronomy" by Mclean (1997).

2.1 *The Near-Infrared Sky*

The near-infrared sky is several magnitudes brighter than the optical sky. The J H & K bands of the NIR are typically 7,8, & 9 magnitudes brighter than the V band of the visible region. If our eyes were to be sensitive to the NIR radiation, then the night sky would appear as bright as the optical twilight sky. The large sky background in NIR is mainly due to the thermal continuum and line emission from the airmass above us and therefore subtraction of background contribution is an important task to be followed while observing in the NIR. This requires an extra background observation for every source observation. Since the airmass at any given geographical location is not stable and keeps changing with time and elevation, it is necessary to observe the background quite frequently depending on the characteristics of the site. The background variations can be as fast as a few seconds or it can remain stable upto a few minutes depending on weather and site conditions.

The biggest difference between the observations in the visible and infrared, particularly at longer wavelengths is noticed while at the telescope. When an infrared image of a relatively faint object is obtained and displayed, almost nothing is seen on the screen except the flat field pattern of the device that is due to the huge background radiation. However, the background contribution alone can be obtained by moving the telescope off the target to a relatively blank area of the sky and repeat the exposure. If the difference of the two images is taken, only then it is possible to 'see' the object on the computer screen.

Background subtraction thus remains an essential part of all IR observations. A standard observing procedure in IR is to obtain images in a sequence of “sky, object, sky, object,...sky”. Nevertheless, the frequency of obtaining the sky images and the techniques of data reduction vary slightly depending on the quality of the site, instrument, season, type of object, type of observation and so on.. One has to establish these procedures for a given instrumental set-up and site by making sufficient amount of observations.

2.2 *PRL Near Infrared Camera: PRLNIC*

PRLNIC is India's first operational infrared camera, a turn key instrument built by Infrared Labs Inc. USA for PRL. The design is based on the Near-Infrared Camera and Multi-Object Spectrograph (NICMOS3) concept and uses a 256×256 HgCdTe detector. The schematic of the camera along with the unit that couples it to the telescope is shown in Figure 2.1. The $f/13$ beam from the Gurushikhar 1.2m telescope is directed by a gold coated 45° mirror, such that it enters the 50 mm entrance aperture of the camera. Figure 2.2 shows the schematic of the LN_2 cooled “cold chamber” of the camera that houses the optical components and the detector. Just after the entrance aperture, the $f/13$ beam can be intruded by a focal reducer using which it can be compressed to an $f/6.5$ beam that changes the camera field of view (FOV) from $2' \times 2'$ to $4' \times 4'$. These options yield plate scales of $0.5''/\text{mm}$ and $1''/\text{mm}$ respectively for the two FOV's. The focal reducer lens is a plano convex doublet that has BaF_2 and Fused Silica components. The beam then enters the filter wheels and is focussed on the cold Lyot stop (aperture). Three Lyot Stops are available, circular and square apertures for imaging and a slit of width $75 \mu\text{m}$ (2 pixel wide) for spectroscopy. The beam emerging out of the Lyot stop is collimated by a section of a parabolic mirror that sends the collimated parallel beam on to a mirror/grating assembly. This assembly can be rotated to switch between a plane mirror or a grating, to enable imaging or spectroscopic modes respectively. This set-up is called

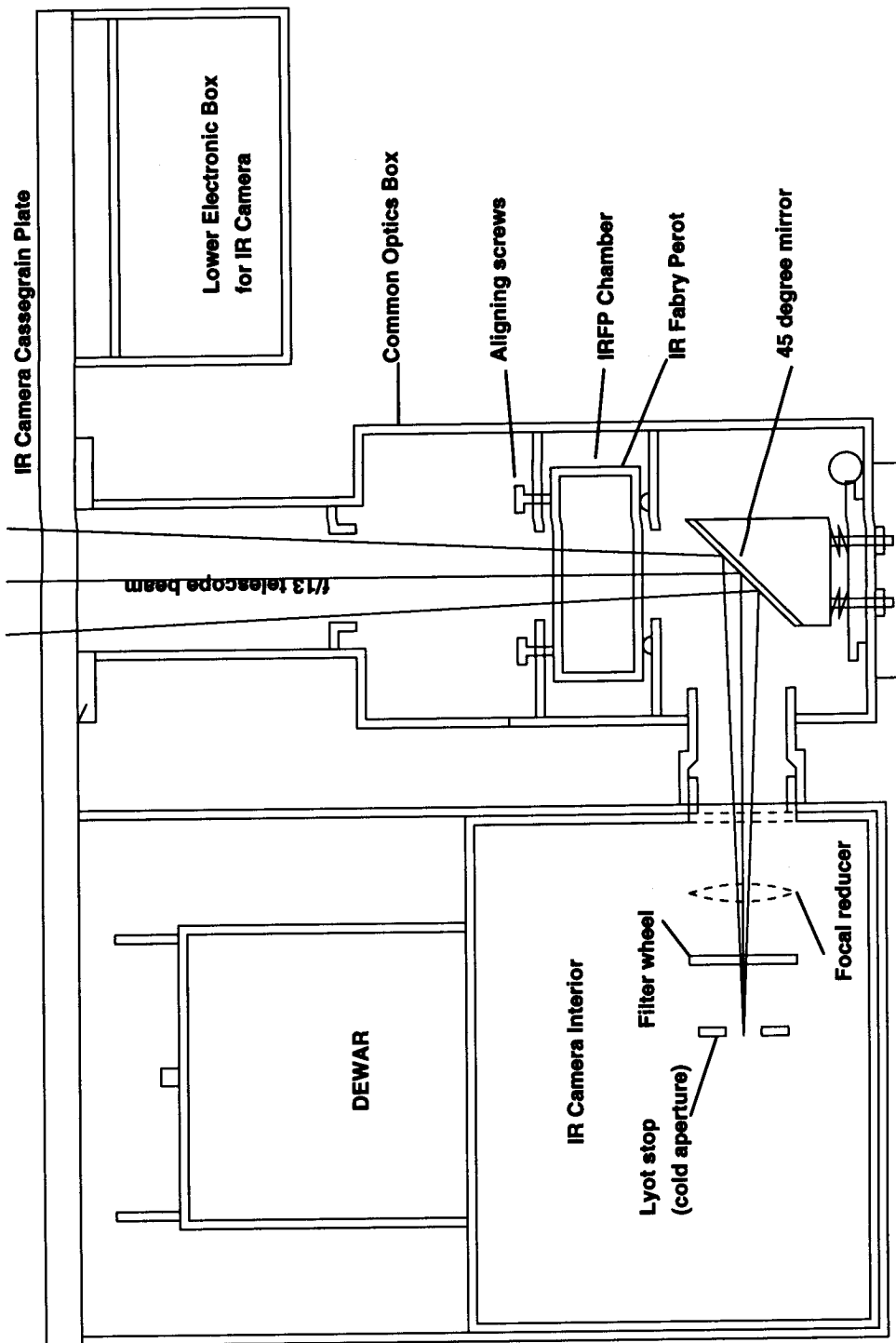


Figure 2.1: Schematic Diagram of the mechanical coupling of PRLNIC

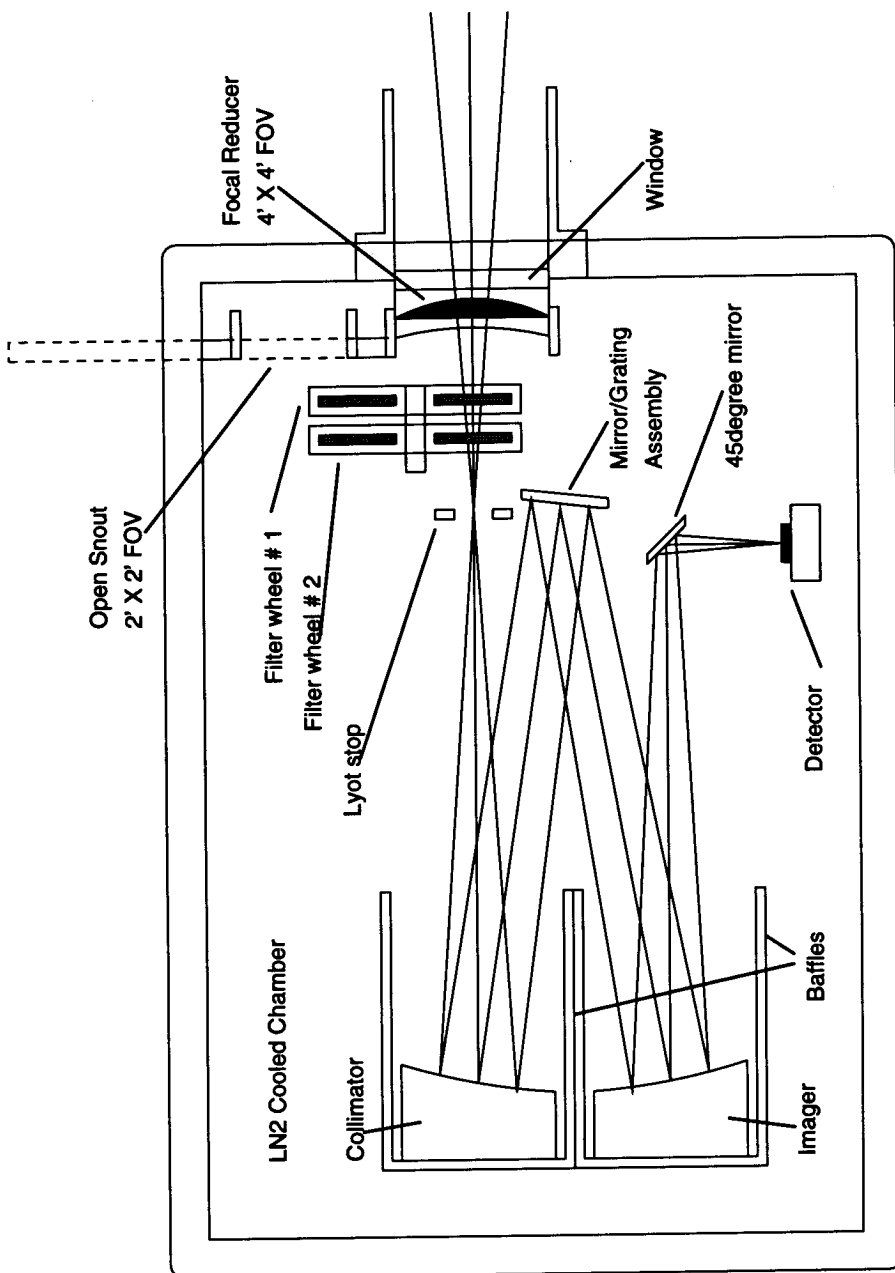


Figure 2.2: Schematic Diagram of the Infrared Camera optics

Table 2.1: Detector Array Characteristics

Detector	256×256 HgCdTe
Pixel size	40 μ m
Readnoise	53 e ⁻
Darknoise	<0.7 e ⁻ /s
ADC	32 bit
Bad Pixels	46
Total yield (Usable Pixels)	99.9%
Linear range	1000-10000 ADU
Sytem Quantum Efficiencies	
K band	28.91%
H band	18.30%
J band	32.75%

the Ebert-Frosty set-up. The parallel beam reflected by the mirror/grating assembly is re-imaged by another section of the parabolic mirror. The converging beam from this parabolic mirror is diverted sideways to fall on the detector, by a small adjustable plane mirror. The characteristics of the detector are summarised in Table 2.1 and a list of available filters are given in Table 2.2. A tunable Fabry-Perot etalon which is an optional instrument, is available as an extremely narrowband filter to operate in the 2-2.5 μ m region, as well as velocity fields at a rather coarse velocity resolution. *Chapter 6* describes the construction, operation and preliminary results of the NIR Fabry-Perot Spectrometer.

2.2.1 Camera Operating Software

The camera operating software as of the date of writing this thesis, is quite primitive and is a locally modified version of the basic software provided by the manufacturer. It provides menu options to choose the image acquiring modes and also to control the camera motors which drive the filter wheels and mirror/grating assembly. The Three modes of acquiring NIR images (see McLean 1997) are available, namely

- a) Single Frame Mode (Staring Mode)- Simple Read.

Table 2.2: List of filters for PRLNIC

Filter Wheel 1	$\lambda_{max}(\mu m)$	$\Delta\lambda(\mu m)$	Filter Wheel 2	$\lambda_{max}(\mu m)$	$\Delta\lambda(\mu m)$
Home			Home		
[FeII]	1.645	0.0375	J	1.253	0.296
H ₂ S(1)	2.1175	0.0429	H	1.659	0.288
NB1	2.1352	0.0428	K	2.185	0.408
Br γ	2.164	0.0443	K'	2.120	0.360
CO	2.3726	0.1013	Blank		
NB2	2.2169	0.0831	Blank		
Open			Blank		

b) Difference Frame Mode (Fowler Sampling)

c) Multiple difference mode (Multiple sampling)

It is possible to choose the reset to read time, integration time and number of frames for each of these modes.

2.3 Black Magic for the Black Box: PRLNIC

The turn key nature of PRLNIC and a possible hardware problem had resulted in several difficulties related to acquiring and analysing the images in the standard procedure suggested in the literature. This section discusses some non-standard, but specific solutions to be followed to overcome the existing problems and still obtain good quality data.

2.3.1 The Problem

When a single frame is acquired with PRLNIC and displayed on the screen, there appear two strips of grey shade levels, occurring one each at the lower and upper half of the detector area. These strips have count levels that are very different from the average count of the frame. As one keeps acquiring the images in single

difference frame mode (frames that are saved as D1, D2, ..in the PC), it can be noticed that the two strips occur at different positions and their intensity levels change or they may totally disappear in some frames. Since the position and width of these strips vary from frame to frame, the effects can not be removed by flat fielding procedure. Luckily, the strips occur only when the detector is reset and therefore the strips go off with time. Therefore, the problem exists only for the first few seconds of acquisition after the detector is reset. There are two Analog to Digital Converters (ADC's) that operate on the detector, with each ADC controlling two quadrants of the four quadrant chip. The problem mentioned above is thought to originate due to a high value of the bias setting of the ADC's.

2.3.2 The Solution

The solution is straight forward, once the behaviour of the problem is understood. Acquire a sequence of exposures in the multiple difference frame mode and throw away the first couple of frames of the resulting set of the multiple frame sequence. For example, if the exposure consists of 10 frames, each with integration time of 60 sec, the frames will be registered on the disk as S1,S2,...S10. While processing it will be required to discard the frame S1 (just to be sure discard S2 also) and use the frames S2/S3-S10. This process should be repeated for every set of exposures made. When a multiple difference frame-set is acquired, the detector is reset, and is read in a non-destructive way at successive intervals of the integration time that is set by the observer. A difference frame is generated by subtracting the successive "reads" from one another. In the process of throwing away the first couple of frames, we are essentially discarding the frames that retain the effects of resetting the detector (the frames containing the strips). This procedure results in the wastage of some observing time. However, the wastage is not much if one is observing in the K or K' bands where the individual exposures are short, say 3-5sec, but can be significant in the narrowband, J and H band imaging. The linear range of the detector is found to be 1000-10000 counts. The optimum exposure times through various filters while using PRLNIC + Gurushikhar 1.2m telescope, are background limited

Table 2.3: Typical Exposure times through various filters

Filter	K	K'	H	J	narrowband
Exposure (in sec)	2	5	25	40	75

and are given in Table 2.3. The exposure times should be such that the maximum counts on the frame is less than 10000 counts with a mean value of 8000-9000 counts. The saturation begins by 12000 counts (some portions of the detector are fully saturated) and at 16000 counts the detector is hopelessly saturated.

2.4 Observation and Data Reduction Procedures

The difficulties of NIR imaging described in section 2.1 are most severe at longer wavelengths which is K band for this camera. H band has less thermal background continuum contribution but a very high contribution from the atmospheric emission lines. A bit of both expertise and experience is required to effectively remove the varying sky background in the K band between 2 and $2.5\mu\text{m}$. The following sections describe the standard observing and data reduction procedures, with an emphasis on the points to be taken care while observing specifically with PRLNIC. The procedures are discussed for both the imaging and spectroscopic modes.

2.4.1 Imaging Mode

The most common and recommended mode for acquiring frames is the 'difference frame mode' which uses a double correlated sampling. In this mode, options are available to obtain single difference frames or multiple difference frames. The large number of background photons fills the detector wells very quickly, which makes it mandatory to acquire images of small exposures and co-add them to obtain the required integration time on the sources. This enforces the choice of the multiple

difference frame mode to acquire NIR images. The standard set of frame required for one complete observation are *Source Frame*, *Sky Frame*, *Flat Frame*, and *Dark Frame* which are used to obtain a 'Final Frame' by using the rule,

$$FinalFrame = \frac{SourceFrame - SkyFrame}{FlatFrame - DarkFrame} \quad (2.1)$$

Dark frames are important while performing good photometry. Several dark frames are to be obtained and median-combined or averaged to form a final dark frame. Since the dark levels fall in the non-linear range of the detectors, it is important to obtain different dark frames of exposure times same as that of the source exposures. The sky frames must be obtained as close in time as possible to the source frames. It is customary to sandwich the source frame between two sky frames of the same exposure as that of the object frames. The 'midpoint frame' obtained by the midpoint of the two adjacent sky frames is the appropriate sky frame for the respective object frame. In a sequence of 'sky1, obj, sky2' the correct sky frame is obtained by performing an operation '(sky1+sky2)/2'. However, this is not very essential and in some cases where photometry is not required, simple subtraction of the immediate sky frame from the object frame may as well be sufficient. Sky subtraction does not take care of the pixel to pixel quantum efficiency variations and therefore a flat field has to be applied even after the sky subtraction. However, the sequence of applying the sky and flat corrections can be different. There are two options to subtract the sky background;

- 1) The object and sky frames are divided by the flat frames after which sky frames are subtracted from the object frames. This will remove the time to time variation of the sky background. This method becomes inevitable if the detector area is covering a large field of view over which the sky background can have a pattern.

- 2) After the object and sky frames are divided by the flat field, a 'Sky Value' derived from the respective sky frames can be subtracted from the object frames. This technique will work only if the background is uniform over the entire detector and

does not have varying patterns. An advantage of this method is a gain in the noise factor that results from the subtraction of a 'SKY VALUE' and not a 'SKY FRAME'.

K and K' bands 2-2.5 μ m

Owing to the high level of background, the K band exposure times are typically 2-4 sec at Gurushikhar observatory depending on the sky conditions. Therefore, it is necessary to acquire a large number of exposures and co-add them to form the final image. For typical integration times of 30 min to 1 hour, the total number of frames can be a couple of thousands. Data storage and transfer of such large number of frames can be very expensive and cumbersome. Some observatories therefore offer the facility to co-add the frames on-line and then store the images to the disk. If the source is not extended beyond one quarter or one half of the chip, then it is best to dither the object within the detector area so that, the necessary sky is obtained in the subsequent source frame itself. Subtracting adjacent frames from one another will remove the sky background. However, if the object is extended to cover more than 70-80% of the detector area, then there is no escape to obtaining obj-sky-obj-sky sequences. Generating a good flat field image is easier when a large number of sky frames(100's or 1000's) are available. Median-combined sky frames will form a good sky-flat. If the object is dithered, or if several sources are observed on a particular night, then a good sky flat is obtained by simply median-combining all the frames taken through a particular filter.

J, H and Narrow bands

The background levels in these bands are relatively much smaller and therefore individual exposures can be longer. This results in less number of frames for median-combining for a given total integration time. Therefore, it is necessary to be careful in obtaining appropriate flats and sky frames which can not be generated using object frames or sky frames as described above. While acquiring the sky frame it is important that an 'empty' area of sky be chosen. Any "source" registered in the sky frame will not be effectively removed by the median-combining procedure, since the total number of available frames for statistics will be small. An independent

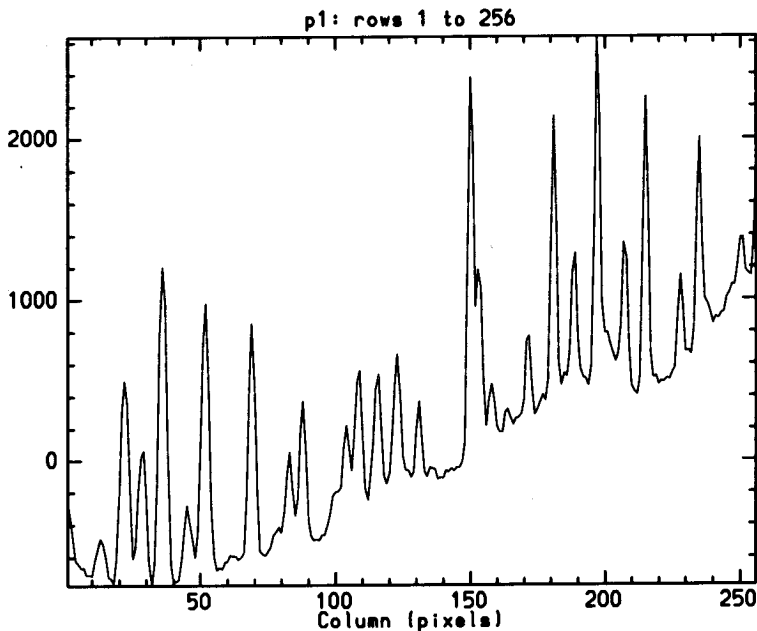


Figure 2.3: Schematic Diagram of the mechanical coupling of PRLNIC

flat frame should be obtained by pointing the telescope at a flat screen or twilight sky. Dithering technique is still valid if the object sizes are small. Great difficulties are encountered, particularly while observing sources close to the galactic center, since finding an “empty sky” becomes very difficult. It may be required to nod the telescope to a sufficiently large offset in order to find a fairly empty region of the sky or an apriori planning of the sky position should be done before the start of the observations. The same techniques apply even to the narrowband imaging, except that the choice of sky is not very difficult since the source brightness is generally cut off due to the narrowband of transmission and also line emission sources are less in number compared to normal continuum sources.

2.4.2 Spectroscopy

One of the important contributions to the near-infrared sky background comes from the telluric lines. A raw spectrum in the H and K bands can illustrate this fact very clearly. Fig 2.3 shows the raw spectrum displaying the intense telluric lines in the 2.1-2.3 μ m region. It is important to subtract these emission lines effectively to obtain the source spectrum. The standard procedures for NIR observing are applied

for spectroscopy as well with the sequence of sky-obj-sky frames. The job of obtaining a sky frame is relatively easier with a long slit as that of PRLNIC, which covers about $4'$ in the wide field mode. For point sources, images are obtained with the source placed at different points along the slit. However, it becomes necessary to nod to an empty sky region while observing extended objects like emission nebulae or galaxies. The atmospheric transmission is not uniform over the entire spectral region of $1\text{-}2.5\mu\text{m}$. It varies with wavelength and the intensity of variation is dependent on the airmass and time of observation for a given site. To correct for this variation, it is necessary to obtain the transmission function particularly at the time of observation. This is done by observing stars whose spectra are well-known. The apriori knowledge of the spectra of the standard stars comes from modelling of the stellar atmospheres. By observing such stars called spectral standards we can get the transmission factor as a function of wavelength that will be utilized in correcting for atmospheric effects. A list of spectral standards and their spectra are given by Lancon & Rocca Volmarange (1992). The convention is to observe G or F type dwarfs as spectral standards for the J, H, and the $2.1\text{-}2.3\mu\text{m}$ region of K band and early type stars(A0) for later part of K band. The G and F type dwarfs can have CO overtone absorption features in their spectra and is therefore not suitable as a spectral standard in the K band. Likewise, the A0 stars have all the hydrogen recombination lines in the J and H bands and are therefore not suitable. While observing in the regions of poor atmospheric transmission, for example, between $2.3 - 2.5 \mu\text{m}$, it is important to observe several standard stars of different spectral types to ensure proper corrections. It is important that the standards be observed as close to the sources as possible, both in time and airmass. Generally the standards should be chosen such that they are within 0.1 airmass to the source. Flats are to be obtained exclusively by illuminating the flat screen by an incandescent lamp. Spectral calibration requires obtaining images with the flat screen illuminated by standard spectral sources like Krypton/Argon/Xenon lamps.

The source frames are differenced with the sky frames to remove the sky emission. It is then divided by a flat frame from which a dark frame has already

been subtracted. Ideally, if one is interested in a good spectro-photometry then it is required to correct for the wavelength dependence of the blackbody source used for flat fielding. Generally, several frames are median-combined to form the final frame. With PRLNIC, the image section of each exposure containing the spectrum is cut, and all the cut pieces are median-combined to form a co-added (integrated) image. The spectrum is extracted from this integrated image using APALL task in IRAF. Similar procedure is followed for the spectrum of the spectral standard star. The spectra of the sources are divided by the spectrum of the standard star observed at similar airmass. The resulting source spectra are multiplied by a blackbody spectrum corresponding to the temperature of the standard star. Spectra obtained with the PRLNIC are discussed in *Chapter 4*. The atmospheric characteristics of Gurushikhar are such, that we have hardly been able to obtain meaningful data beyond $2.4\mu\text{m}$ in any observing run during 1998-1999. The absorption factor is quite high resulting in severe noise beyond $2.4\mu\text{m}$. However, the most important features in this region, namely CO band-heads, fall within the $2.4\mu\text{m}$ range and therefore, nothing much is really lost due to atmospheric effects.

2.5 *Future efforts*

There are several modifications that are essential to standardize and improve the camera. Although "black magic solutions" exist to remove the effects of a high bias level, it is necessary to adjust the bias settings in the hardware and make it possible to use the single difference frame modes as well. This will save a lot of observing time when performing narrow-band imaging and spectroscopy. The existing slit is $75\mu\text{m}$ and is 2 pixel wide. This will subtend a maximum angle of $2''$ in the wide field mode. However, in the wide field mode the lens is in the path of the beam resulting in a relatively low efficiency of transmission. The average seeing at Gurushikhar is $2''$ - $3''$, and with the guiding errors put together, it is important to have a slit of $4''$ that can cover the stellar disk safely during the exposure times. Spectroscopic observations, therefore, calls for an urgent requirement of a second slit (in

particular a slit of $150\mu\text{m}$ width) that will be needed to improve the signal-to-noise ratio. It should also be noted that it is not possible to do spectral flux calibration using standard stars, because of the narrow slit that can not cover the entire seeing disk during the exposure period. Observers are using target source photometry to carry out the flux calibration. Therefore, a second slit which is twice the size of the existing one will enable flux calibration using spectral standards. Several major improvement/ additions in the image acquisition software are required which should be more user-friendly and that can write image headers automatically. An option to sum the images during online observing using median or average programs will help handling enormous amount of data storage memory. This is quite crucial since the K band background levels are high and it is not possible to expose the detector for more than 2-3 seconds in the best of the sky conditions. The common optics box requires a modification asking for widening the entrance aperture. The edges of the $4'$ field get vignetted in its current status, thus, allowing only the central $3.5'$ to be useful while doing accurate photometry. These improvements can make PRL-NIC with Gurushikhar 1.2m telescope, a competent infrared observing facility. A glimpse of its current performance can be seen in Fig 2.3. In Fig 2.3, the total FOV is $8' \times 8'$. The faint bar is seen at the bottom-left quadrant and is the famous orion PDR, while the trapezium is nearly at the center. Several faint finger-like features are seen at the top-right quadrant which are the bunch of Herbig-Haro objects.



Figure 2.4: H_2 Image of Orin Nebula obtained through the $2.122\mu\text{m}$ narrow-band filter. The MOSAIC is composed by tiling four $4' \times 4'$ frames.

2.6 References

- Elston, R., 1991, Ed. *Astrophysics with Infrared Arrays*, ASP conf series, Vol 14.
- Lancon, A., & Rocca-Volmerange, B., 1992, A&A Suppl. Ser, 96,593
- McLean, I. S., 1994, Ed. *Infrared Astronomy with Arrays: The Next Generation*, Kluwer Academic Publishers, Dordrecht, Netherlands.
- McLean, I. S., 1997, *Electronic Imaging in Astronomy, Detectors and Instrumentation*, Wiley-PRAXIS Series in Astronomy and Astrophysics, John-Wiley and Sons Ltd.
- Mampaso, A., Prieto, M., Sanchez, F., 1993, Eds. *Infrared Astronomy*, Cambridge University Press, England.
- Reike, G. H., 1994, *Detection of light from Ultraviolet to the Submillimeter*, Cambridge University Press, Cambridge, England.
- Wynn-Williams, C. G., & Becklin, E. E., 1987, Eds. *Infrared Astronomy with Arrays*, The Institute of Astronomy, University of Hawaii.

Cold Disk Structures in Protostellar Envelopes

3.1 Introduction

Young low mass stars are born in the middle of dense molecular cores that are traced by NH_3 emission (Myers and Benson 1983). Recently it has been shown that dense cores are also the smallest structures in a molecular cloud that are not self-similar. This means that the dense cores are discrete (non-fractal) entities in a filamentary molecular cloud after the formation of which, gravitational collapse becomes important (Borranco and Goodman 1998). Once a young star has formed inside a dense core, there is sufficient material left in the surrounding envelope, a part of which still accretes on to the star through a Keplerian disk (Shu 1987 and references therein). The inner disk is hot with temperatures exceeding 1000K and extends upto 1-10AU and found in almost all young stars (Boss 1998). There are disks that are warm (100-500K) and have radii of 10-300AU. These disks are seen around T Tauri stars that have blown away most of the molecular material around them and therefore do not show much CO emission. The objects of discussion here are a special class of envelopes surrounding young stars and are huge (500-2000AU), cold (10-100K) and contain frozen ices in them. The envelopes are coincident with the dense cores seen in NH_3 emission and are shown to have disk structures (Borranco and Goodman 1998 and references therein). We discuss in this chapter the study of a unique dark cloud L43 which harbours two protostellar objects RNO 90 and RNO 91 that are known to have envelopes containing disk

structures.

RNO 91 is similar in many respects to the archetypal example L1551-IRS5, in particular, for having a poorly collimated outflow (Davis et al. 1995) and a large nebular protostellar envelope. The speciality of RNO 91, however, is due to the presence of a huge envelope of radius 1700AU (10'') that has a disk structure and contains frozen ices. Ices found on dust grains in a protostellar envelope are referred to as "icy mantles" and have importance in the study of planet formation (Chiar et al. 1998 and references therein). RNO 91 has been studied extensively by various researchers independently as an outflow and as a disk. The outflow was shown, currently not to be driven by a jet (Bence et al. 1998). Weintraub et al. 1994 (hereafter W94) concentrated on the central disk portion and showed the presence of ices in the envelope and a 1700AU disk structure.

The following work was motivated towards a search for infrared emission from the center of the cold envelope and the weak outflow of RNO 91 which we believe would help in understanding the disk structures around RNO 90 and RNO 91. We present here, the first near-IR spectroscopic and narrowband imaging studies and describe the implications of having detected extended emission from shocked molecular hydrogen from RNO 91. We bring out the importance of studying the cold disk structures which may likely be associated with dense cores of relatively high density or with certain physical parameters of the cloud. The key to understand poorly collimated outflows also lies in studying clouds like that of L43.

3.2 *The L43 dark cloud*

The L43 dark cloud is situated in the northern part of the Ophiuchus complex at a distance of 160 pc (Herbst & Warner 1981, hereafter HW81) presumably associated with the Scorpius OB complex. It appears as a long strip of extinction with filamentary structure extending over 1000'' in length and 200'' in width. Fig 3.1 shows the POSS red plate which displays extinction over an area $\sim 1.7 \times 0.2 \text{ pc}^2$, at PA 68°.

The cloud was mapped in CO by Elmegreen and Elmegreen (1979) who found that the CO emission from the cloud was extending roughly twice as far as the optical extinction patch in all directions. Their ^{12}CO and ^{13}CO data revealed an elongated core near the center of the molecular cloud, with a mass greater than $14M_{\odot}$. Loren (1981) deduced a density of $1.5 \times 10^5 \text{ cm}^{-3}$ in this core, from H_2CO observations and indicated that the core was a likely site of star formation. Two opaque spots in the core were identified by Myers, Linke and Benson (1983) on the POSS prints (marked A, B in Fig 3.1), that were later shown to be associated with the NH_3 emission (Myers and Benson, 1983) indicating the presence of a dense molecular core of $2.0M_{\odot}$.

The cloud contains two stars surrounded by reflection nebulosities that were catalogued in Cohen's (1980) list of Red and Nebulous Objects as RNO 90 and RNO 91. RNO 91 is situated at the center of the cloud, coinciding with the dense core described above and RNO 90 lies about $5'$ to the west of RNO 91. Optical and infrared photometry of these sources were obtained by HW81. Optical spectrum of RNO 90 (HW81) and RNO 91 (Levreault 1988) classified both the objects as T Tauri stars. The properties of the stars are listed in Table 3.1. Of the two, RNO 91 is seen in the 12, 25, 60 and $100 \mu\text{m}$ maps (identified as IRAS163116-1540) (Beichman et al. 1986) and drives a weak CO outflow (Levreault 1988, Myers et al. 1988, Mathieu et al. 1988). Molecular line studies of the L43 cloud in various species have shown the existence of an outflow and a dense core. The emission from the dense core and the outflow are in perpendicular directions, with the dense core representing the surrounding disk region. We therefore discuss the outflow and the dense core in separate sections.

3.2.1 *The CO outflow in L43*

The CO outflow of the L43 cloud is centered on RNO 91 and has spatially separated red and blue shifted lobes of unequal lengths. This indicates that the outflow may be inclined to the plane of the sky at a moderate angle. The outflow has been

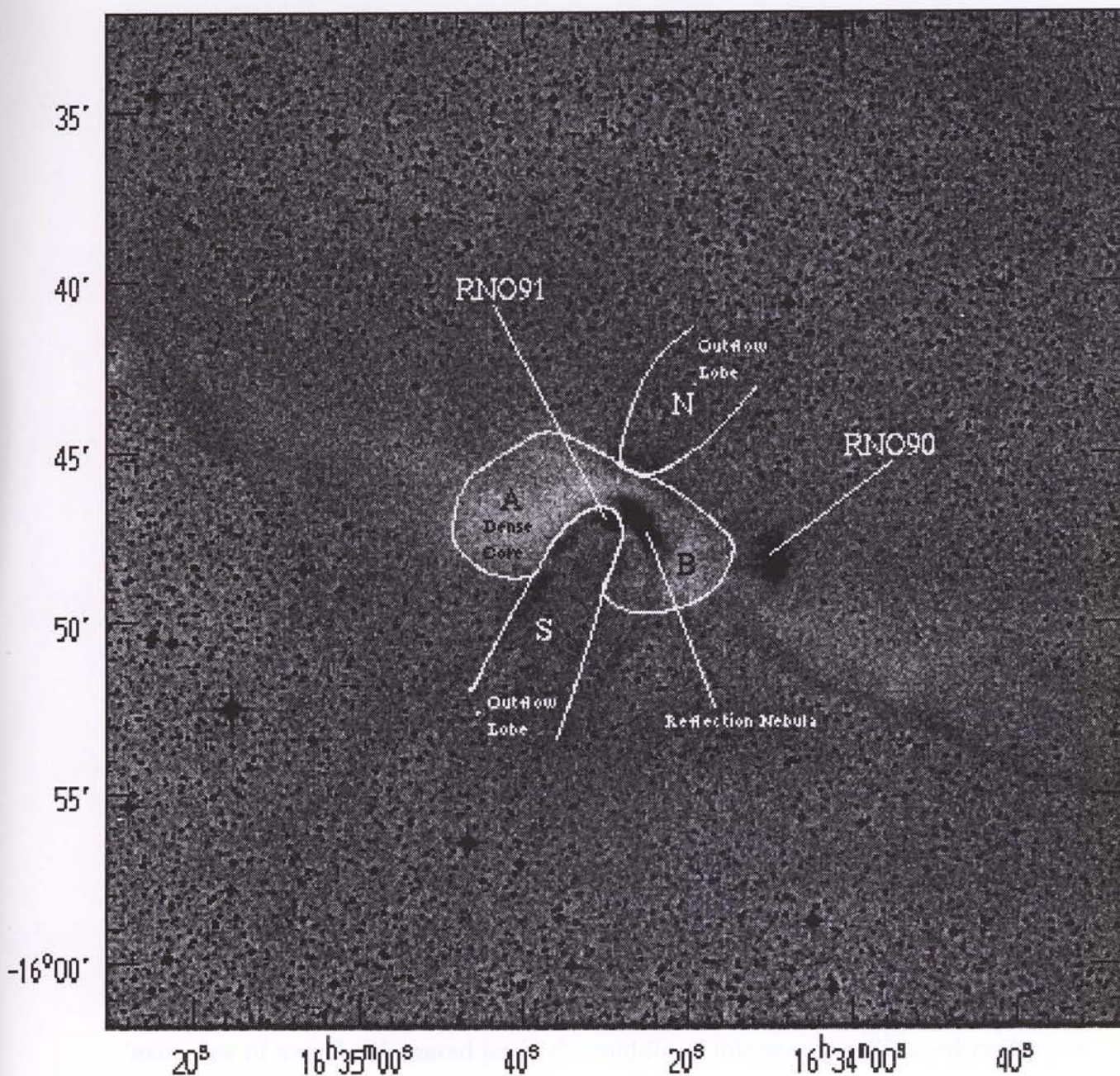


Figure 3.1: POSS red image (negative) of L43 dark cloud. Notice the filamentary nature of the cloud. Dense core is marked by A and B. The outflow lobes are marked N and S representing the north and south lobes respectively.

studied in the millimeter emission of CO molecules by Levreault (1988), Myers et al. (1988), Mathieu et al. (1988), Parker et al. (1988) and Bence et al. (1998). The largest area has been covered by Bence et al. (1998) who show that the extent of the outflow is twice as large as the optical extension of the cloud. The outflow parameters are summarised in Table 3.1. The outflow has a strong asymmetry, with the southern lobe more extended and more intense than the northern lobe. Coincidentally this is true even in the case of L1551-IRS5. The northern lobe in both objects does not show much emission and is much fainter compared to the southern lobe. Some authors attribute this observation to insufficient amount of swept up material to the north, while a few others attribute it to the inclination angle effects. There is also a strong momentum (mv) asymmetry in the lobes. This type of asymmetry is seen in several other outflows like NGC2024 and HH46-47 and is attributed to the lack of available ambient material for sweeping. Latest maps by Bence et al. (1998) show a jet-like feature about $150''$ long, extending to extreme southeast. Optical studies of RNO 91 by Mathieu et al. (1988) and Schild et al. (1989) showed that there were no signatures of shocked emission associated with the outflow. The low values of velocities observed in the molecular maps also supports this observation.

We show in the following sections that there exists an extended $H_2 v = 1 - 0$ S(1) emission at $2.122 \mu m$ associated with this jet-like feature. We note that the existence of a well collimated jet in the middle of this poorly collimated cavity is a common feature between L1551-IRS5 and RNO 91.

3.2.2 L43 dense core

The dense core was identified optically and later in NH_3 emission by Myers and Benson (1983). Mathieu et al. (1988) mapped the core in NH_3 (1.3mm) and CS $J = 2-1$ emission at 3mm. The NH_3 emission is coincident with the opaque spots on the POSS image, which are the regions of high extinction in the east-west direction. They show that the spatial distribution of the NH_3 emission roughly anti-correlates

Table 3.1: Observed parameters of L43 stars and outflow

Star	d (pc)	M (M_{\odot})	Age (yr)	Type	L_{bol} (L_{\odot})	M_k	A_v
RNO 91	160	0.5	1×10^4	M0.5	4.7	7.8	9
RNO 90	160	1.5	6×10^6	G5	3.9	6.5	-
Outflow	M	Age (yr)	\dot{M} ($M_{\odot} \text{yr}^{-1}$)	\bar{V}	V_{wind}	V_{lsr}	
RNO 91	$0.07 M_{\odot}$	2.5×10^4	8.9×10^{-9}	-3.5 km s^{-1}	300 km s^{-1}	0.7 km s^{-1}	

with that of the CO outflow emission. This tendency is notably different from that found around IRS5 and the L1551 outflow, where the large scale NH_3 emission is coincident with and elongated along the axis of the outflow. The CS(2-1) emission is relatively more extended but is still confined along the east-west direction. The NH_3 lines are very narrow having typical widths of 0.3 km s^{-1} outside the physical boundaries of the outflow and upto 0.5 km s^{-1} within the boundaries of the outflow. The CS(2-1) line widths are about twice as large and range from $0.6 - 1 \text{ km s}^{-1}$.

Mathieu et al. (1988) noticed a steep gradient in the velocity field to the east of RNO 91. Beyond $1.5'$ (0.007 pc) east of RNO 91 the velocity field is roughly constant at $0.7\text{-}0.8 \text{ km s}^{-1}$. However, at $1.5'$ a steep gradient begins, with a slope of $\sim 3.5 \text{ km s}^{-1} \text{ pc}^{-1}$ between this point and the star. The gradient exists to the west as well, but not as strongly as it is to the east. A plot of V_{lsr} versus RA offset presented by the above authors shows red and blue shifts in the emission with a spread of 0.4 km s^{-1} . They arrive at a $2 \text{ km s}^{-1} \text{ pc}^{-1}$ gradient in both the NH_3 and CS velocity fields and suggest that if these gradients are associated with a rotation, then the angular momentum vector is perpendicular to the outflow direction. The following sections demonstrate the existence of a disk structure around RNO 91 which supports this suggestion. The central core has been imaged at $450 \mu\text{m}$ by Bence et al. (1998). They show that the emission comes from an elliptical region around the peak that is centered on the FIR source RNO 91. There is also a slight extension to

the south, approximately aligned with the CO outflow axis. The total flux that they measure is 92 Jy. They conclude that the emission is caused by light reflected in the surrounding cloud of RNO 91. This cloud is, in fact, the homogeneous dense core out of which RNO 91 has formed.

3.3 RNO 90: A T Tauri Star in L43

RNO 90 is one of the two lonely T Tauri stars in L43 and is seen to be surrounded by a nebulosity on the POSS red plate (see Fig 3.2). The star is classified by Levreault (1985) to be of G5 spectral type with a mass of $1.5 M_{\odot}$ and an age of 6×10^6 yrs. The properties of the star have been listed in Table 3.1. A spectrum, taken by the same author, also revealed strong H_{α} emission ($EW = 76 \text{ \AA}$) with a flux of $F(H_{\alpha}) = 1.4 \times 10^{-12} \text{ ergs cm}^{-2} \text{ s}^{-1}$. The object was first imaged in the I band by Mathieu et al. (1988) along with RNO 91. The surrounding nebulosity is seen prominently in the I band image. However, there are no optical dark spots seen around RNO 90 that may give a clear indication of the presence of a dense core. It has been shown that there indeed exists a dense core surrounding RNO 90 that is well seen in NH_3 emission. The observations of the L43 dense core by Mathieu et al. (1988) were extended around RNO 91 until the peak line intensity dropped to below $\sim 0.15 \text{ K}$. These observations covered only one side of RNO 90 and therefore could not see the dense core associated with RNO 90. Additional and more extended observations of the L43/RNO 90 region were carried out by Borranco and Goodman (1998) who present the detailed NH_3 maps. As described in section 3.2.2, there are velocity gradients associated with the dense core around RNO 91 which are attributed to the rotation. Borranco and Goodman's data on RNO 90 also bear the same trend but with an additional fact that the axis of the gradients found in the dense cores can be different from that of the surroundings. They find a gradient of $1.07 \pm 0.05 \text{ km s}^{-1} \text{ pc}^{-1}$ oriented at 108 ± 4 degrees east of north associated with the RNO 90 dense core. This is about half the value of what is found for the RNO 91 dense core.

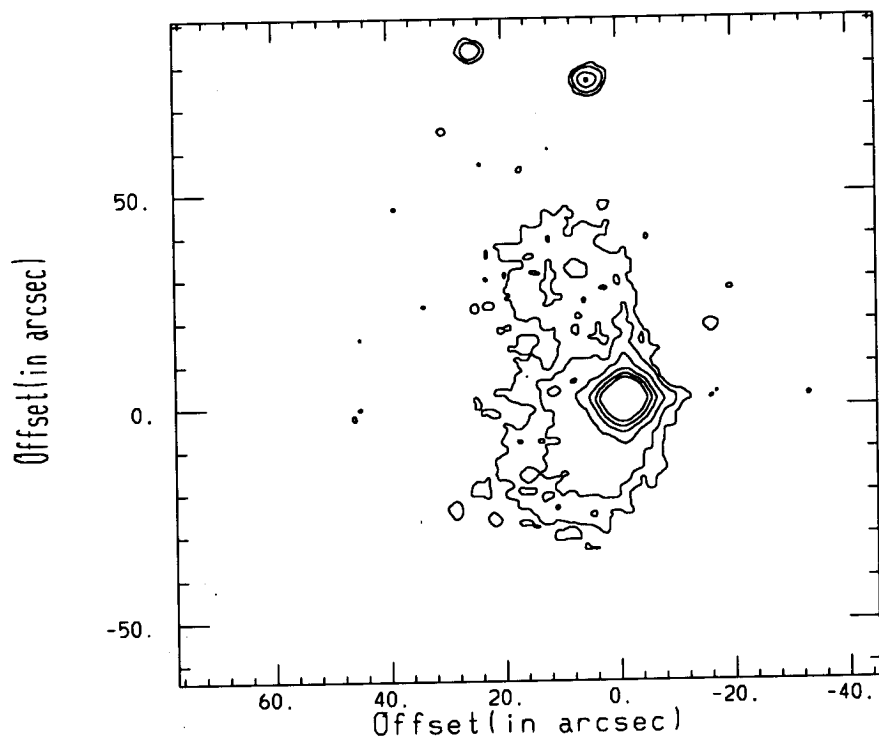


Figure 3.2: Contours of RNO 90 from the POSS prints

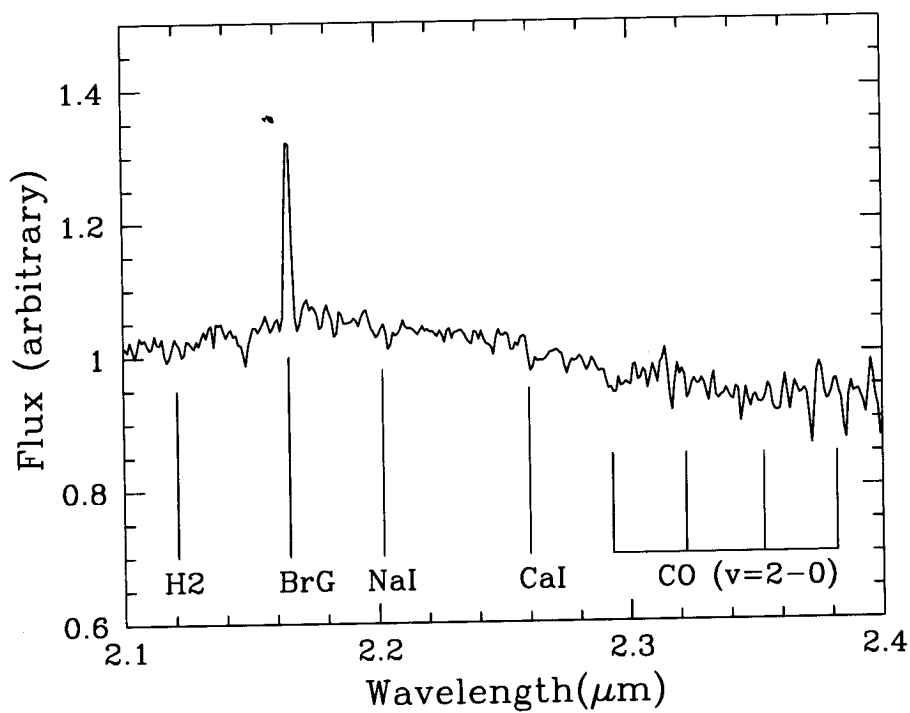


Figure 3.3: Spectrum of RNO 90 taken with PRLNIC and GIRT

The latest optical spectrum of the central star of RNO 90 published by Cieslinski et al. (1998) displays weak red continuum with emission lines of Balmer series, HeI ($\lambda\lambda$ 5876, 6678), H (λ 3968) and K(λ 3934) lines of CaII. These authors refer to a private communication with Quast & Torres for the proof of LiI (λ 6707) absorption line taken with the Coude Spectrograph of the LNA on April 24, 1988. These features are all strongly characteristic of a T Tauri star and confirm the classification of HW81. Aspin et al. (1997) have imaged the central $4'' \times 4''$ region around RNO 90 using the shift-and-add technique in the near-infrared to investigate the presence of a binary companion and reported no obvious sources.

We present a 2.1-2.4 μ m spectrum of RNO 90 in Fig 3.3. Positions of important spectral features in this wavelength region are marked. There is an intense Br γ emission, NaI and CaI absorption that can be just noticed, and no clear CO absorption features. The absence of CO overtone features and very shallow NaI and CaI features are characteristic of typical G type dwarfs and therefore our results reconfirm the earlier classification by HW81. Further, the presence of strong Br γ emission is an indicator of winds in RNO 90. There is no H $_2$ emission seen in our spectrum and therefore do not indicate the presence of any outflow/accretion signatures. There is no associated IRAS emission with this source. Therefore the SED class of this object is not known by IRAS emission. However, the optical and NIR data together suggest that it should be a ClassII or ClassIII source.

3.4 *Shocked molecular hydrogen from RNO 91*

The near-IR molecular hydrogen emission lines are recognised as important tools in studies of star formation (Shull & Beckwith 1982). The excitation of these lines involves mainly two competing processes: (i) shock heating and (ii) UV fluorescence (Burton 1992). It is possible, however, to distinguish between these two processes by measuring the ratios of intensities of lines arising from two different vibrational levels (Sternberg & Dalgarno 1989, Hora & Latter 1994). The origin of shocked molecular hydrogen emission from the spatially unresolved region close to a star

can originate from outflows or from accretion shocks in a disk, as in the case of Infrared Companions (IRC's) (Herbst et al. 1995, Koresko et al. 1997). It is also possible that the emission can arise both from an outflow and accretion shocks, as in the case of T Tauri.

While it is known that almost all outflows are driven by jets, the absence of any shocked emission from RNO 91 and a poorly collimated outflow made it an interesting object where one would expect that a different mechanism must be driving the outflow. It was indeed argued by Bence et al. (1998) that the slowly expanding shell of the outflow was either driven by a wide angled wind or by the thermal pressure of a hot, low emissivity medium interior to the shell. However, the presence of a jet emitting in shocked molecular hydrogen was not looked for. From another viewpoint, the existence of a disk structure and a thick envelope around RNO 91 suggested possible ongoing accretion which can result in shocked emission of molecular hydrogen. The following sections describe the first near-infrared spectra and narrow band images of this object obtained by us in the K band region. The detection of the H_2 $v = 1-0$ S(1) line at the source and its implications are discussed.

3.4.1 *Observations and Data Reduction*

Near-infrared spectroscopic observations were made on March 25, 1998 at Gurushikhar 1.2 m Infrared Telescope (GIRT), Mt. Abu, India. A Near-Infrared Camera/Grating Spectrometer based on a HgCdTe 256×256 focal plane array was used to obtain the observations. The grating spectrometer was used in a configuration that yielded a resolving power of $\lambda/\delta\lambda = 1000$ with a $1''/\text{pixel}$ plate scale. The slit was two pixels wide and oriented along the N-S axis. The atmospheric seeing and image motions were below $2''$ during the observations, which was measured from imaging data obtained just before the spectroscopic observations. Data acquisition and reduction were done using standard procedures described in *Chapter 2*. We used the RNO 91 K band photometric fluxes (0.48 Jy) given by Myers et al. (1987)

for flux calibrating the spectrum.

Narrow band ($\Delta\lambda = 0.02\mu\text{m}$) images through H_2 ($\lambda = 2.122\mu\text{m}$), $\text{Br}\gamma$ ($\lambda = 2.165\mu\text{m}$) and continuum ($\lambda = 2.104\mu\text{m}$) filters were obtained under a United Kingdom Infrared Telescope (UKIRT) Service Observing Program on September 8, 1998 using the facility near-IR imager IRCAM3. IRCAM3 employs a 256×256 InSb array; the optics used gives a pixel scale of $0.140''$. Unfortunately there was a small defocusing problem that occurred during these observations due to variable seeing, resulting in image elongation in the N-E, S-W direction. These uncertainties were estimated to be about $1.2''$. Continuum subtraction was not carried out because of this focusing problem in these images. It should also be noted that there is some ghosting present in these images. The ghosts in 3 different narrowband filters occur at definite positions. These are identified as ghost images since they occur at exactly the same position with respect to the main source both in the object and standard star frames.

A new set of images were obtained again under the UKIRT service program on March 17, 1999 using the new camera, the UKIRT Fast Track Imager (UFTI). UFTI employs a 1024×1024 HgCdTe array; the optics used gives a pixel scale of $0.091''$. The seeing was measured to be $\sim 0.5''$. Continuum subtraction was carried out with these images but uncertainties remain: it is very difficult to do a proper subtraction in the filter images since we were trying to detect faint H_2 emission in the midst of strong IR continuum that is scattered by the surrounding icy envelope. This has led us to use low resolution, longslit spectroscopy to detect extended emission from such objects (see *section 3.8* for details).

3.4.2 Results

The contour map of the spectrum shown in Fig 3.4 displays the extended H_2 emission along the N-S direction (the slit axis) corresponding to the outflow axis. The intensity peaks at $-3''$ and $+2''$ represent H_2 knots in the outflow. From the gaussian fits to the continuum emission profile at different positions along the dispersion

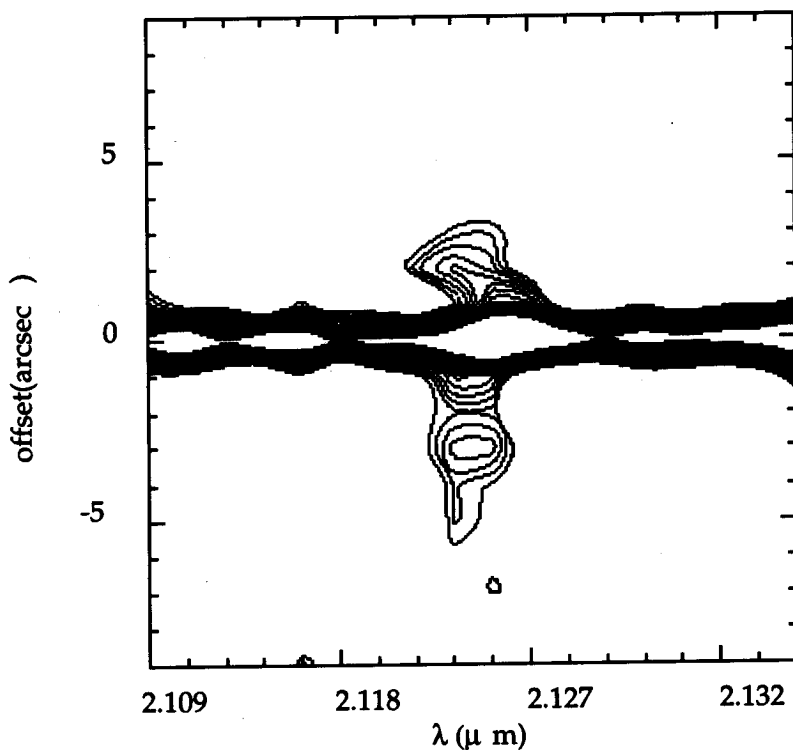


Figure 3.4: Contours of H_2 2.122 μm line from RNO 91 spectrum showing the extended emission. Notice the different lengths of emission in the N-S from the center that indicates the tilt of the outflow axis. Continuum is *partly subtracted* using an adjacent strip of the same spectrum, which has caused the artifact of width variability.

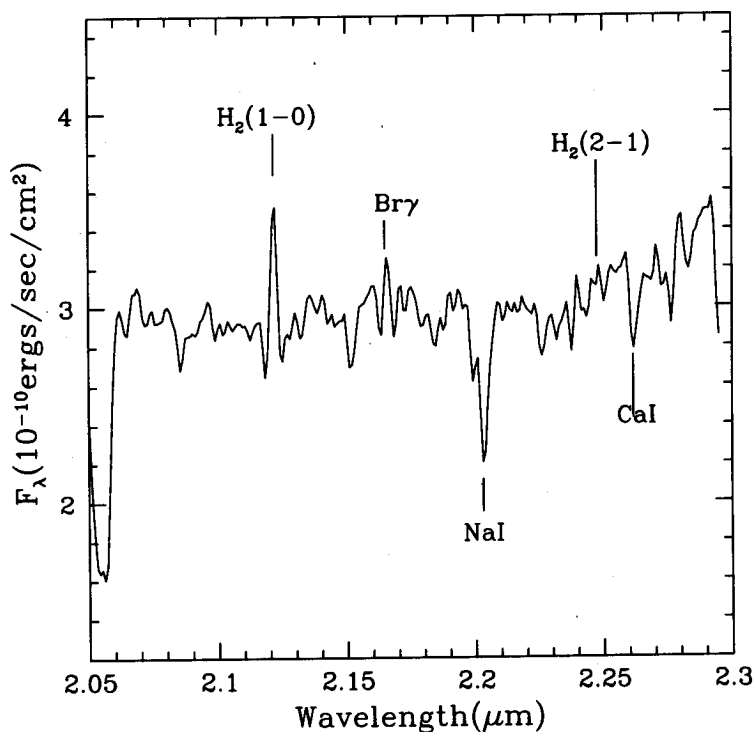


Figure 3.5: Spectrum of RNO 91 integrated over 9 rows representing an area on-source of $2'' \times 9''$.

axis, we find that the FWHM of the continuum strip (measured N-S) is about $3.0''$, although the seeing on the night of observation was between 1.5 - $2.0''$. The extra width in the stellar continuum strip could be attributed to scattered light from the cocoon surrounding the star. We have therefore extracted the source spectrum by integrating the emission along three and then five rows, representing an on-source area of $2'' \times 3''$ and $2'' \times 5''$. The relative intensities of the photospheric NaI and CaI features remained the same in these two extractions. However, in the $3''$ -wide extraction, the $2.122\mu\text{m}$ line intensity was considerably smaller than in the $5''$ extraction, relative to the photospheric features. This shows that most of the H_2 emission comes from outside the stellar close environment (photosphere + circumstellar region). This result confirms that the broadening of the continuum strip is indeed due to scattered star light.

Fig 3.5 shows the spectrum of RNO 91 in the wavelength region $2.05\mu\text{m}$ to $2.3\mu\text{m}$. The spectrum is obtained by integrating nine rows, covering $9''$ along the N-S slit axis centered around the star. The spectrum displays prominently the H_2 $v=1-0$ S(1) line at $2.122\mu\text{m}$ and the photospheric NaI and CaI absorption features at $2.20\mu\text{m}$ and $2.26\mu\text{m}$ respectively. The 2-1 S(1) line at $2.247\mu\text{m}$ is at the noise level (1σ). The spectrum also displays the $\text{Br}\gamma$ emission line at $2.167\mu\text{m}$. These features are marked in the figure. Most of the other features seen in absorption are telluric in nature (Chelli et al. 1997).

The excitation mechanism for H_2 emission can be inferred from the 2-1 S(1)/1-0 S(1) flux ratio (e.g. Luhman et al. 1998). Conventionally, a 2-1 S(1)/1-0 S(1) ratio of less than 0.2 indicates shock excitation and for fluorescence this ratio is about 0.5. An estimated upper limit to the 2-1 S(1) line flux yields this ratio to be 0.16 or less, pointing strongly towards shock excitation. However, fluorescent excitation in a high density regime may also produce a "shock-like" 2-1 S(1)/1-0 S(1) ratio, because of thermalization of low-energy vibrational levels (Sternberg & Dalgarno 1989, Burton et al. 1990). In a high density region one would still expect to see emission from the $v=3$ level at 10% of the 1-0 S(1) line (rather than 1%, as

is expected in a shock; see e.g. Luhman et al. 1998). However, in our spectrum the 3-2 S(3) line is unresolved from NaI absorption, and the 3-2 S(1) line is outside the wavelength range covered in the spectrum.

We resolve this issue by estimating the two most crucial parameters that decide the efficiency of the UV fluorescence, namely, the gas number density and the UV flux scaling parameter χ (see Sternberg and Dalgarno 1989). We estimate an upper limit for the gas number density to be $6 \times 10^5 \text{ cm}^{-3}$, considering an $A_v \sim 9$ (Myers et al. 1987), an outer disk radius of 1700AU (W94), and an inner disk radius of 0.01AU corresponding to the dust evaporating radius for an M0 star. Note that this density is for a gas disk of 1700AU and the actual regions from where we expect the H_2 emission are well below a radius of 200-300AU. On the other hand, the UV flux scaling parameter χ for an M0 type star is much less than 1. From these arguments, we conclude that the UV fluorescence is expected to be of little significance for the excitation of H_2 lines.

3.4.3 Discussion

From the spectrum we measure an H_2 flux of $7 \times 10^{-14} \text{ ergs sec}^{-1} \text{ cm}^{-2}$ (integrated over 3 rows, representing an area on-source of $2'' \times 3''$). If we attribute this flux to shocks, whose origin we do not know at the moment, we can estimate the mass flow rate \dot{M} using the relation

$$\epsilon L = GM\dot{M}/R = 1/2\dot{M}v^2 \quad (3.1)$$

where ϵ is the ratio of the total energy in the shock to the strength of the 1-0 S(1) line, L is the observed H_2 line luminosity, and v the shock velocity. We adopt a value for v of 30 km s^{-1} , a value that is optimum for producing H_2 line emission. We also assume that $\epsilon = 50$ (Smith 1995). Together, these yield an estimate for mass flux of $\dot{M} = 4 \times 10^{-8} M_{\odot} \text{ yr}^{-1}$.

First, we look at the possibilities of an outflow as the source of this emission. As demonstrated in the previous section, the relative change in the intensity of H_2 from that of the photospheric features in the spectra extracted with different widths of the continuum strip shows that the H_2 emission close to the star very likely originates from a region different from that traced by the photospheric lines. The fact that the H_2 line emission is extended along our N-S slit strongly suggests that the H_2 is associated with an outflow. By observing line emission coincident with the RNO 91 stellar continuum, we may therefore be tracing the outflow all the way back to the source. The total flux measured from the observed extended emission (integrated over 9 rows representing an area on-source of $2'' \times 9''$) is 1.5×10^{-13} ergs $\text{sec}^{-1} \text{cm}^{-2}$. This represents an average flux distribution of 3.5×10^{-4} ergs $\text{sec}^{-1} \text{cm}^{-2} \text{sr}^{-2}$. It is known that the total H_2 luminosity (in all vibration-rotation lines) can be approximated to be 10 times the S(1) line luminosity (Davis & Eisloffel 1995). Thus we can write,

$$L_{H_2} \sim 10 \times L_{S(1)} \quad (3.2)$$

The measured luminosity has to be corrected for extinction by using the formula (Davis & Eisloffel 1995)

$$L_{H_2}(\text{Corrected}) = L_{H_2} \times 10^{A_{2.2}/2.5} \quad (3.3)$$

which yields a net H_2 luminosity of $0.002L_\odot$. The kinematic age of the outflow can be simply calculated as $t = R/v$ where R is the measured length of the outflow and v is the velocity for H_2 excitation which turns out to be ~ 200 yrs for a $9''$ long outflow that we observe in the spectrum with an assumed velocity of 30 km s^{-1} . Using this age and the estimated mass flow rate of $\dot{M} = 4 \times 10^{-8} M_\odot \text{ yr}^{-1}$, the H_2 luminosity can be shown to represent a net warm H_2 mass ($M_{H_2} = \dot{M}_{H_2} \times t$) of $\sim 5 \times 10^{-4} M_\odot$.

We shall now investigate accretion shocks in a disk as the possible source

of the emission. The H_2 line flux measured from within the central $3''$ could be associated with the near-IR counterparts of HH knots embedded within the cocoon that are excited by accretion shocks in a disk. This type of situation occurs in Infrared Companions (IRC) where the star is bright in IR due to accretion shocks and almost invisible in optical. Herbst et al. (1995) first studied two IRC's to Haro6-5 and UY Aurigae. They show that if the observed emission of H_2 is due to accretion shocks, then the K band extinction due to such a dense environment can be given by the formula

$$A_k = 2.2 \times 10^5 r^{-1/2} [(\frac{\dot{M}}{10^{-8} M_{\odot} yr^{-1}}) / (\mu_{amu} \sqrt{\frac{M}{M_{\odot}}})] \quad (3.4)$$

where r is the point at which we see the H_2 emission is excited at a velocity v , μ_{amu} is the mass of the excited molecule in atomic mass units, which is H_2 in this case, and \dot{M} is the mass accretion rate. Using this formula for the case of RNO 91 we get $A_k = 1.73$ to the $v=20 \text{ km s}^{-1}$ point. Here $v=20 \text{ km s}^{-1}$ point is situated at the radial distance from the star at which free falling material (under the influence of the star's gravity) will reach that velocity. Assuming the $A_k = 0.1 A_v$ law, this implies an $A_v = 17.3$ which is much higher compared to the measured value of $A_v = 9$ by Myers et al. (1988). Therefore, excitation of all of the observed "on-source" H_2 emission due to infall is not feasible. However, some fraction of the observed emission could originate from accretion shocks, with the rest from the outflow, as in the case of T Tauri.

It is interesting to note that a careful investigation of the high resolution images obtained via Shift-and-Add imaging at UKIRT by Aspin et al. (1997) reveals a nebulous feature which is about $1''$ to the north of the star (not reported by the authors). This could be a shock excited feature in the outflow. Alternatively, this feature – in conjunction with the fainter features to the S-W of the star – could be a part of an ellipse whose major axis is $\sim 200 \text{ AU}$ as measured by us using the published images of A97. In fact these features may be visualized in terms of a disk tilted by 30° to the north. The absence of any feature to the south may be attributed

to the obscuration of the disk by the outflow.

3.5 *RNO 91 disk/outflow*

The disk structure of the envelope surrounding RNO 91 was first identified by Heyer et al. (1990) from their JHK images and H-band polarimetric images. W94 showed in detail that this disk structure is huge (1700AU) with ices contained in it. They obtained a 3-5 μ m spectra of the disk material and found three absorption features at 3.08 μ m, 4.68 μ m, and 4.62 μ m which are identified to be due to frozen H₂O, CO, and possibly XCN occurring along the line of sight towards RNO 91. Further, W94 obtained K' polarimetric images of RNO 91. Whitney and Hartmann (1992) have produced models of scattering in circumstellar disks and bipolar envelopes (1993) surrounding young stellar objects. Their model results are plotted as sets of intensity contours overlaid on polarimetric vector patterns. W94's K' polarimetric images conformed to these model contours from which they concluded that the nebulosity around RNO 91 has a disk structure of radius of 1700AU. They also showed that the polarization center does not coincide with the intensity peak identified as RNO 91. Our speculation that this result might indicate an Infrared Companion to RNO 91 was quickly laid to rest by the Shift-and-Add imaging by A97, which does not show any secondary source within a 3.7'' square region. W94 suggest a scenario with a flared disk and outflow viewed at an angle of 30° with the northern outflow lobe tilted away from the observer.

Fig 3.6 shows a narrow band image taken by us on September 8, 1998 through H₂ filter, without continuum subtraction. Fig 3.7 shows the new images obtained with UFTI on March 17, 1999. Fig 3.8 shows a continuum-subtracted narrowband image of RNO 91 in the 2.122 μ m filter. Continuum-subtraction is an extremely difficult task, since, here we are trying to remove extended continuum emission which is more than 80% of the total light. Also the star is close to the emission regions making it more difficult to discern the emission regions by subtraction of continuum. This is a case which is uncommon and hence, rife with

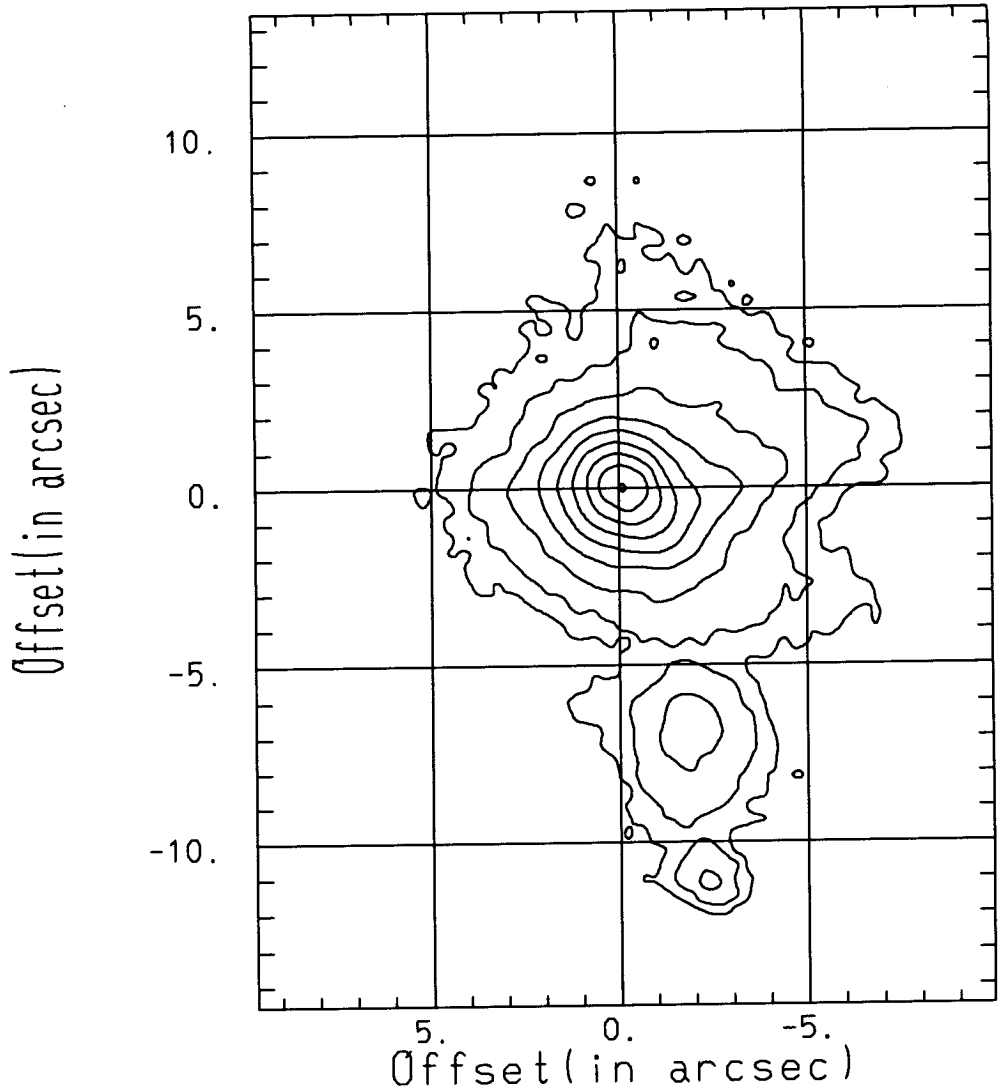


Figure 3.6: IRCAM3 Image (1" seeing) Contour plot of RNO91 taken through H₂ narrowband filter, illustrating an east-west disk associated with the source, as well as nebulous emission to the south. The contours measure 5,10,15,20,40,80,160,320 and 640 times the standard deviation to the mean background level in the images.

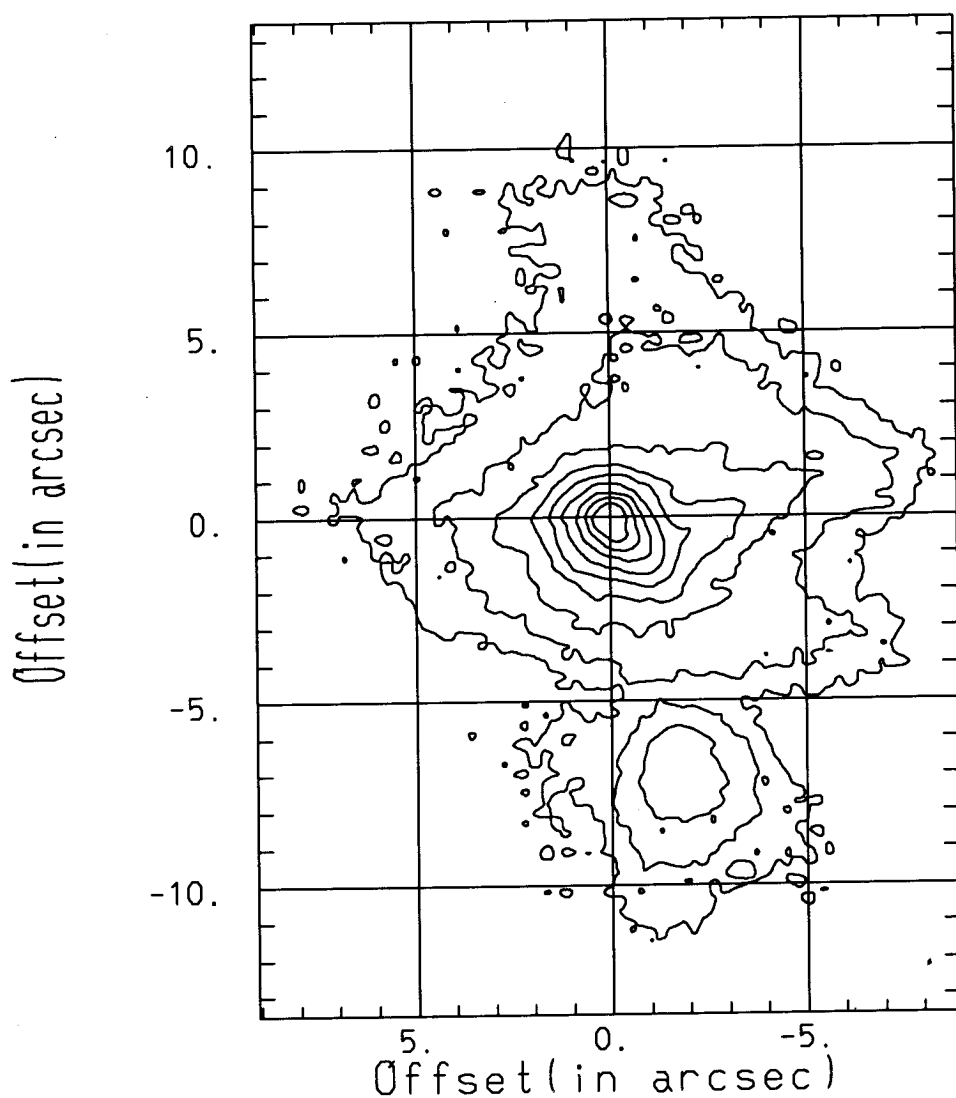


Figure 3.7: UFTI Image ($0.5''$ seeing) Contour plot of RNO 91 taken through H_2 narrowband filter, illustrating an east-west disk associated with the source, as well as nebulous emission to the south. The contours measure 5,10,15,20,40,80,160,320 and 640 times the standard deviation to the mean background level in the images.

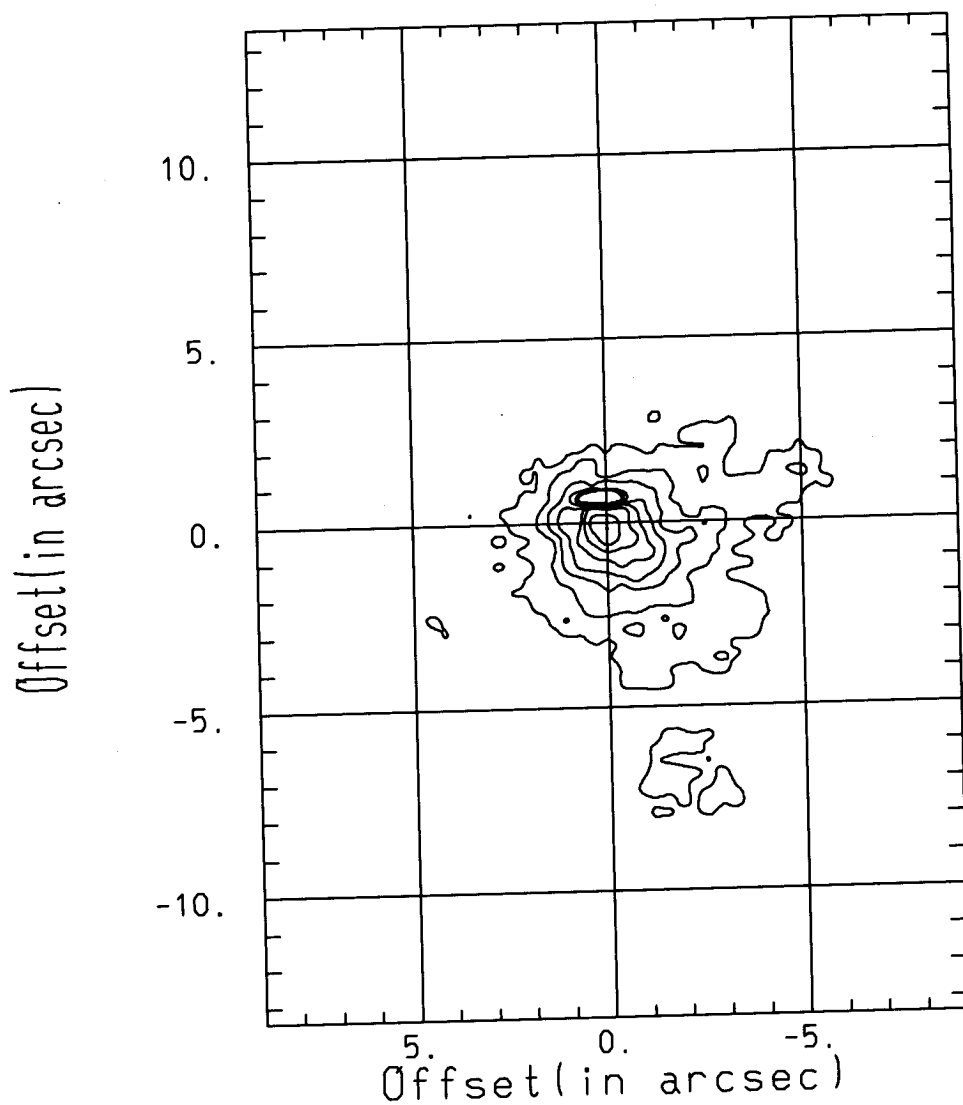


Figure 3.8: Continuum-subtracted narrow-band H_2 images from UFTI. The contours represent 5,10,20,40,80,160,320,640 times the standard deviation to the mean background level in the images.

uncertainties, due to which we do not draw any definitive conclusion based on the continuum-subtracted image. However, we have smoothed the original online and offline images by a 3×3 box, normalised the images to proper intensity and magnification by using the standard star image references and then performed the subtraction. It was much easier to detect the extended H_2 emission through the spectrum than the narrowband images and we learn from this experience that using either longslit spectroscopy at low resolution or Fabry-Perot Imaging can be the best way of detecting extended line emission in the presence of strong continuum emission. Due to this problem, we suspect that Schild et al. (1989) may not have been able to distinguish the H_α emission in their narrowband images, that could be originating in an outflow. On the other hand, Levreault's (1988) detection of intense H_α in his spectrum suggests that a part of it could be originating from a low excitation jet. An optical slit spectrum with the slit oriented along the outflow direction can confirm this fact.

The disk structure and an outflow lobe to the south can be seen clearly in these images (Figures 3.6, 3.7 and 3.8). These structures are more evident in the narrow band image (for instance, Fig 3.7), than in the K' image of Hodapp (1994) or the polarimetric image of W94. The narrow band image (note specifically the patch of continuum emission to the south of RNO91) clearly supports the scenario of W94, that there is a disk structure of size 1700AU, and an outflow whose northern lobe is directed away from us and obscured by the disk structure. In addition, it can be seen from Fig 3.4 that the H_2 emission is extended more in the southern direction than in the northern direction which confirms that the northern lobe of the outflow is directed away from us, being obscured by the disk structure. Notice that the higher resolution image (0.5'' seeing) in Fig 3.7 shows finer features in the disk structure and the outflow. The continuum-subtracted image clearly shows an extended emission from the southern lobe and a 7'' disk structure. However, the central portions of this structure could be contaminated by residual continuum.

As pointed out in *Section 3.1*, RNO 91 falls into the class of disk structures that

contain ices in them, and possess by far the largest icy gas/dust disk structure ($10''$). W94 found the presence of the ices for the first time in RNO 91, with the detection of H_2O absorption features and estimated an optical depth of $\tau = 1.29$. Brooke et al. (1999) have also detected the H_2O absorption features and show that the optical depth derived from this feature is $\tau = 2.1 \pm 0.2$ which is higher than the estimate of W94. They attribute this absorption with amorphous ice rather than crystalline ice. They obtained a $2\text{-}2.5\mu\text{m}$ spectrum as well, that shows CO gas overtone absorptions. This allows them to characterize RNO 91 to have a photosphere that is intermediate between a main-sequence dwarf and a giant, as do several young stellar objects in the ρ Oph cloud. They also point out that this photosphere is consistent with the low bolometric luminosity of RNO 91 ($\approx 3.7 L_\odot$; Chen et al. 1995), a characteristic of young star with low surface gravity. Apart from having an envelope containing ices, RNO 91 also shows shocked H_2 originating in an outflow and possibly an accretion disk. These features make RNO 91 unique and an interesting object for further studies in millimeter and infrared wavelengths.

3.6 Future Work

Our new continuum-subtracted H_2 images of RNO 91 obtained with UFTI show the disk structure extending upto $7''$ in radius. This disk structure contains the scatterers, namely icy mantles, which are ices condensed on the dust grains in this envelope. But the scattering efficiency and density is so high that the disks are seen to a large extent even in the line emission light that forms a small percentage of the total scattered light. The scattering intensity contours is strikingly similar to the theoretical predictions (Wood and Whitney 1998). We shall call this disk with icy mantles as "cold disk". If we assume that there also exists a hot Keplerian disk at the interior, which is a very well founded assumption that has supporting observations, then several questions follow:

- 1) What is the connection between the warm Keplerian disk and the cold disk?
- 2) In what type of environment and at what epoch of star formation can one see

such cold disks ?

- 3) Do they carry signatures of planet formation? (for example fragmented clumps?)
- 4) Is there any correlation between the outflow age and the presence of such cold disks?

Answers to these questions can come from an understanding of the structure of the cold envelopes around young stars. Firstly, the velocity structure of the envelopes is required. For this purpose it is necessary to obtain high spectral and spatial resolution velocity maps of the disk region. It is difficult to do this using the mm emission lines since the emission around RNO 91 region, for example, is optically too thick to give rise to any contrast in the channel maps that can be obtained with an interferometer like IRAM. The emission is very dense and will saturate the detectors. However, the scattered emission lines that we have found should be of great help in making such a study possible. If one obtains a high resolution echelle spectrum at a good spatial resolution also, which is easily possible with facilities like the CGS4 echelle on UKIRT, we believe to get details on the kinematic structure of the disk. If one places the slit at different points on the disk, then the line emission getting scattered from that portion of the disk should contain signatures of the properties of the scatterer which show up as broadening of these lines. This will help, for example, to study the effects of turbulent motions if any at the central regions of the cold disk. Modelling the scattered intensity of light from the cold envelope using radiative transfer should reveal the density distribution in the envelopes. The warm disks are now quite well studied by IR spectroscopy and millimeter imaging. Although the 2-2.5 μ m spectrum obtained by Brooke et al. (1999) shows the CO overtone absorption features, high resolution spectrum will be required to associate the features with the photosphere or a disk. Similar studies of other objects like RNO 90 , L1489IRS, L1551-IRS5 and many others in the line can answer the questions posed above.

3.7 Summary and Conclusions

We have studied the L43 dark cloud that has a few special features. The cloud hosts two dense molecular cores associated with two T Tauri stars RNO 90 and RNO 91, and has a number density that is on the upper side of the known limits ($\sim 10^5 \text{ cm}^{-3}$). These cores contain disk structures which are cold and known to have frozen ices in them.

An infrared spectrum of RNO 90 confirms the classification of the star as a G5 type T Tauri star. RNO 90 is also surrounded by a disk structure as shown by the NH_3 maps of Borranco and Goodman (1998) and also to some extent in the POSS images and I band images of Mathieu et al. (1988).

An infrared spectrum of RNO 91 in L43 dark cloud shows emission of shocked molecular hydrogen from an outflow in the N-S direction and also from a spatially unresolved region close to RNO 91. We estimate a mass flow rate of $\dot{M} = 4 \times 10^{-8} M_{\odot} \text{ yr}^{-1}$, based on the line fluxes from this spatially unresolved region around RNO 91. The line fluxes from the spatially extended outflow yield $L_{\text{H}_2} \sim 0.002 L_{\odot}$, representing a net warm H_2 mass of $\sim 5 \times 10^{-4} M_{\odot}$. The outflow seen here in H_2 emission, extending roughly N-S, appears to support the tilted disk + outflow model of W94, where the northern flow lobe is tilted away from us at an angle of $\sim 30^\circ$ to the plane of the sky. Our narrow band images also support this scenario. We suggest that the H_2 flux from the spatially unresolved region around the source could originate in "HH-type" knots embedded in the cocoon surrounding the star. However, accretion shocks cannot entirely be ruled out based on our observations. These results suggest the possible existence of an infrared jet at the center of the poorly collimated outflow. This is against the proposition of Bence et al. (1998) that the outflow is currently not driven by a jet. However, the results put together can suggest that the outflow is in a stage when the "jet is being turned off". These disk structures hold important clues to understanding warm-cold disk connection and possibly planet formation.

3.8 References

- Aspin, C., Puxley, P. J., Hawarden, T. G., Paterson, M. J., & Pickup, D. A., 1997, MNRAS, 284, 257 (A97)
- Borranco, J., & Goodman, A. A., 1998, ApJ, 504, 207
- Boss, A. P., 1998, Annu. Rev. Earth Planet. Sci., 26, 53
- Beckwith, S. V. W., Gatley, I., Matthews, K., & Neugebauer, G., 1978 ApJ, 223, L41
- Beckwith, S. V. W., Sargent, A. I., Chini, R. S., & Gusten, R., 1990, 99, 924
- Beichman, C. A., Myers, P. C., Emerson, J. P., Harris, S., Mathieu, R. D., Benson, P. J., & Jennings, R. E., 1986, ApJ, 307, 337
- Bence, S. J., Padman, R., Isaak, K. G., Wiedner, M. C., & Wright, G. S., 1998, MNRAS, 299, 965
- Brooke, T. Y., Sellgren, K., Geballe, T. R., 1999, ApJ, 517, 883
- Burton M.G., 1992, Aust. J. Phys., 45, 463
- Burton M.G., Hollenbach D.J., Tielens A.G.G.M., 1990, ApJ, 365, 620
- Cieslinski, D., Steiner, J. E., & Jablonski, F. J., 1998, A&ASS, 131, 119
- Cohen, M., 1980, AJ, 85, 29
- Chelli, A., Cruz-Gonzalez, I., Salas, L., Ruiz, E., Carrasco, L., & Recillas, E., 1997, in eds. Malbet, F., & Castets, A., Low Mass Star Formation - From Infall to Outflow, poster proceedings of IAU Symp. No. 182.
- Chen, H., Myers, P. C., Ladd, E. F., & Wood, D. O. S., 1995, ApJ, 445, 377
- Chiar, J. E., Gerakines, P. A., Whittet, D. C. B., Pendleton, Y. J., Tielens, A. G. G. M., Adamson, A. J., & Boogert, A. C. A., 1998, ApJ, 498, 716

- Davis, C. J., & Eisloffel, J., 1995, A & A, 300, 851
- Davis C. J., Mundt, R., Eisloffel, J., & Ray, T. P., 1995, AJ, 110, 766-775
- Dyck, H. M., Simon, T., & Zuckerman, B., 1982, ApJ, 255, L1 03
- Dutrey, A., Guilloteau, S., & Simon, M. 1994, A & A, 286, 149
Shuster , K.,
- Elmegreen, D. M., & Elmegreen B. G., 1979, AJ, 84, 615
- Herbst, W., & Warner, J. W., 1981, AJ, 86, 885 (HW81)
- Herbst, T. M., Koresko, C. D., Leinert, C. 1995, ApJ, 444 , L93
- Herbst, T. M., Beckwith, S. V. W., Glindemann, A., Tacconi-Garman, L. E.,
Kroker, H., & Krabbe, A. 1996, AJ, 111, 2403
- Heyer, M. H., Ladd, E. F., Myers, P. C., & Campbell, B., 1990, AJ, 99, 1585
- Hodapp, K. W., 1994, ApJSS, 94, 615
- Hora J.L., Latter, W.B., 1994, ApJ, 437, 281
- Koresko, C. D., Herbst, T. M., & Leinert, Ch., 1997, ApJ, 480, 741
- Levreault, R. M., 1985, Ph.D. thesis, University of Texas at Austin.
- Levreault, R. M., 1988, ApJ, 330, 897
- Loren, R. B., 1981, AJ, 86, 69
- Luhman K.L., Engelbracht C.W., Luhman, M.L., 1998, ApJ, 499, 799
- Mathieu, R. D., Benson, P. J., Fuller, G. A., Myers, P. C., & Schild, R., 1988,
ApJ, 330, 385-398
- Myers, P. C., & Benson, P. J., 1983, ApJ, 266,309
- Myers, P. C., Linke, R. A., & Benson, P. J., 1983, Apj, 264, 517

- Myers, P. C., Fuller, G. A., Mathieu, R. D., Beichman, C. A. , Benson, P. J., Schild, R. E., & Emerson, J. P., 1987, ApJ, 319, 340
- Myers, P. C., Heyer, M., Snell, R. L., & Goldsmith, P. F 1988, ApJ, 324, 907
- Parker, N. D., Padman, R., Scott, P. F., & Hills, R. E., 1988, MNRAS, 252, 442
- Schild, R., Nicholas, W., & Mathieu, R. D., 1989, AJ, 97, 1 110
- Shu, F. H., Adams, F. C., & Lizano, S., 1987, ARA&A, 25, 23
- Shull, J. M., & Beckwith, S., 1982, ARA&A, 20, 163
- Smith, M. D. 1995, A & A, 296, 789
- Sternberg, A., Dalgarno A., 1989, ApJ, 338, 197
- Weintraub, D. A., Tegler, S. C., Kastner, J. H., & Rettig, T., 1994, ApJ , 423, 674 (W94)
- Whitney, B., & Hartmann, L., 1992, ApJ, 395, 529
- Whitney, B., & Hartmann, L., 1993, ApJ, 402, 605
- Wood, K., & Whitney, B., 1998, 506, L43

Warm and Hot Disk Structures in Protostellar Envelopes

4.1 Introduction

In *Chapter 3* we discussed a special class of envelopes around young stars that have cold disk structures. This chapter describes the study of the warm and hot disks that can exist interior to the cold disks. The hot disks ($\sim 1000\text{K}$) are generally extending from 1AU to 10AU and are not spatially resolvable with the existing facilities. Warm disks are known to be Keplerian, of sizes around 150-300AU but extend upto 1000AU in a few cases. The sources discussed here are generally found at the edges of the molecular clouds where the ambient cloud material is very less or totally out of molecular regimes. They generally fall into the category of Class II sources and are T Tauri stars with disks and jets. We utilize the power of near-infrared spectroscopy to study these disks, as it happens to be the only means by which one can study the circumstellar disks even with a 1m class telescope. It is important to understand the hierarchy of the disk structures to form a coherent relation between the hot, warm and cold disks. The data discussed in this chapter forms a subset of a larger sample, the coverage of which is not yet complete. We therefore discuss the individual objects and draw general conclusions from the current data set. We present the first near infrared spectra of the disk candidates that are covered in our sample.

4.2 The Sample Set

The choice of the disk candidates can be made based on several hypotheses and thumb rules. Using Lada's classification of YSO's (see *Chapter 1*), it is possible to identify the sources at various stages of their evolution. According to their classification Class II sources have circumstellar disks and have expelled their infalling envelopes. Optical polarization studies of the dark cloud regions resulted in the identification of a high degree of electric polarization vectors around the YSO's, aligned in different directions that was attributed to the existence of circumstellar disks (Bastien 1982). Beckwith et al. (1990) showed that the disks can be identified and characterized using the millimeter continuum emission at 1.3mm and 2.7mm from the YSO's. They made an extensive survey of 86 sources in Taurus-Auriga region and showed that 42% of the sample had disks. The main problem in studying these disks lies in their small sizes (100-300AU) that subtends about 1"-2" at a distance of 140pc in the nearest star forming regions of Taurus-Auriga. Adaptive optics can just resolve the disks into elliptical blobs . With the advent of high angular resolution (0.5"-1") imaging in millimeter lines that was possible with the IRAM interferometer, a sample of 33 stars were imaged in the 2.7mm continuum emission by Dutrey et al.(1996)(hereafter D96). These authors detected 2.7mm emission in 12 systems, some of which were later imaged by HST using the Wide Field Planetary Camera (Stapelfeldt et al. 1997, hereafter S97). The physical properties of these disks are fairly well characterized using the millimeter emission data. Our sample consists of 10 out of these 12 stars that showed strong and extended 2.7mm emission. We have also included a few other sources from the catalog of Herbig and Bell (1988), that are suspected disk candidates due to other reasons described above. We started with these sources since they have flattened disk structures whose masses are estimated and shown to be in Keplerian motion. The temperatures determined by millimeter emission, range between 70K and 300K. The near-infrared spectra are expected to trace the inner hot disks that have temperatures of $\sim 1000\text{K}$.

Table 4.1: Observed Sample of YSO's

Star	SED	Type	K_{mag}	L_{bol}	L_{FIR}	$T^{\circ} K$
CI Tau	II	K7	7.82	1.4	0.23	156
CY Tau	II	M1	8.49	0.49	0.05	79
DG Tau	II	K7-M0	6.74	6.36	3.81	
DL Tau	II	K7	7.97	1.12	0.37	158
DO Tau	II	M0	7.44	2.7	0.64	204
GM Aur	II	K3	8.48	1.0	0.2	167
FS Tau	II	M4	9.8			
V836 Tau	III	K7	8.87	0.51	0.06	80

We present the first near-infrared spectra of the disk candidates in our sample. Observations were made using PRLNIC with the 1.2m Gurushikhar telescope during two observing runs in the months of Jan-Feb 1999. The Spectrograph has a resolving power of 1000 and the slit width is 2" (Refer *Chapter 2* for details of the instrument and data reduction). The stars have been flux calibrated using the photometry provided by Kenyon and Hartmann, (1995). The sample set presented in this chapter are listed in Table 4.1 along with some of their known properties. The quoted temperatures refer to that of the disk and are derived by the millimeter data by D96.

4.3 Infrared Spectroscopy of YSO's

Spectroscopic studies have been one of the most important methods of understanding the stellar photospheres. Studies of absorption features in the optical spectra have made it possible to classify the photospheres of different spectral types. Spectroscopic studies of optical emission lines have also been the main tool in understanding the rotation, abundances and classifying spectral types of T Tauri star photospheres. However, embedded objects that are faint in the visible could not be studied until the beginning of this decade since there were no good infrared spectrographs. The advent of NIR focal plane arrays made it possible to obtain

good quality NIR spectra after which such studies have begun. Some of the early workers in the field noticed the important CO overtone bands in the K band spectra (Carr, 1989, Casali and Matthews, 1992). Hodapp and Deane (1993) used the NIR lines in a first attempt to derive spectral types of the embedded objects from NIR spectra. The power of infrared spectroscopy to study the YSO's has been realised more seriously in the last 5 years due to a better understanding of the interpretation of the spectral features. Greene and Meyer (1995) studied a sample of objects in the ρ Ophiuchi cloud using both spectroscopic and photometric techniques to derive the masses, ages and spectral types of several embedded objects. Casali and Eiroa (1996) present an extensive study of the infrared CO absorption bands and showed that these bands originate in the stellar photospheres of the observed low luminosity embedded sources. They arrived at this conclusion based on the Echelle data that showed the broadening of the CO bands by 17 km s^{-1} which could be attributed to stellar origin rather than a disk. They also showed that the CO absorption depths are correlated with the Spectral Energy Distribution (SED) (see *Chapter 1*) index and suggested that this correlation could result from veiling produced by continuum emission from a hot circumstellar disk. Greene and Meyer (1995) had also discussed the effects of continuum veiling from the hot disk. Greene and Lada (1996) conducted an extensive survey of sources of various SED spectral classes from different molecular clouds. They also observed a large sample of spectral standards. They show that the strengths of the atomic and CO absorption features are closely related to the evolutionary status of the YSO's and the depths of the features are indicative of the relative amounts of veiling of an underlying photosphere by the continuum emission from the surrounding hot envelope.

To summarize the interpretation of CO features in the K band spectrum; Class I objects are embedded, in the sense that they are optically invisible, have infalling envelopes around them that generally causes heavy extinction. The CO absorption features are not found in Class I objects due to strong veiling from the continuum emission of the infalling envelopes. Class II sources are relatively more evolved objects with revealing photospheres and possess accretion disks. These are

mostly the Classical T Tauri stars (CTTS). The atomic and CO absorption features are found in the spectra of these YSO's but are not intense. The veiled features appear weaker than in similar type stars without IR excesses, causing errors in the determination of the spectral types via equivalent width analysis. However, the equivalent widths of suitable line pairs (at similar wavelengths) can be divided to produce ratios which are independent of this veiling (Greene and Meyer, 1995). Class III sources have expelled most of the material and show the atomic and CO absorption features clearly which allow spectral type determination without much confusion.

$\text{Br}\gamma$ emission is another important spectral feature in the K band wavelength range. It was thought until recently that this emission arises in disk winds from young stars (Natta et al. 1988; Hartmann et al. 1990). Recently Najita et al. (1996) have shown that $\text{Br}\gamma$ emission actually originates in the stellar magnetosphere due to the infalling matter. This assumes an X-wind model (see *Chapter 1*) with funnel flows from the disk onto the star. $\text{Br}\gamma$ emission from the YSO's have unusually large linewidths at $400\text{-}700 \text{ km s}^{-1}$ which is more than one should expect due to free fall from infinity to these low mass stars. These large wing emission is attributed to the large scale turbulence in the infalling material. The broad wings are also believed to be partly due to scattering of photons by electrons (Stahl & Wolf 1980). Adding to these observations, Muzerolle et al. (1998) have shown that $\text{Br}\gamma$ line emission can serve as an important probe to the disk accretion in T Tauri stars and embedded YSO's. They show that the accretion luminosity follows a linear relation with the $\text{Br}\gamma$ line luminosity.

4.4 Results and Discussion

Figure 4.1 displays the $2.1\text{-}2.4\mu\text{m}$ spectra of the sample listed in Table 4.1. Tables 4.2 and 4.3 list the measured equivalent widths of $\text{Br}\gamma$ emission and the CO overtone bands. The negative values indicate emission and positive values indicate absorption. The 1σ levels of the spectra vary from $3\text{-}8 \times 10^{-15} \text{ watts m}^{-2} \mu\text{m}^{-1}$

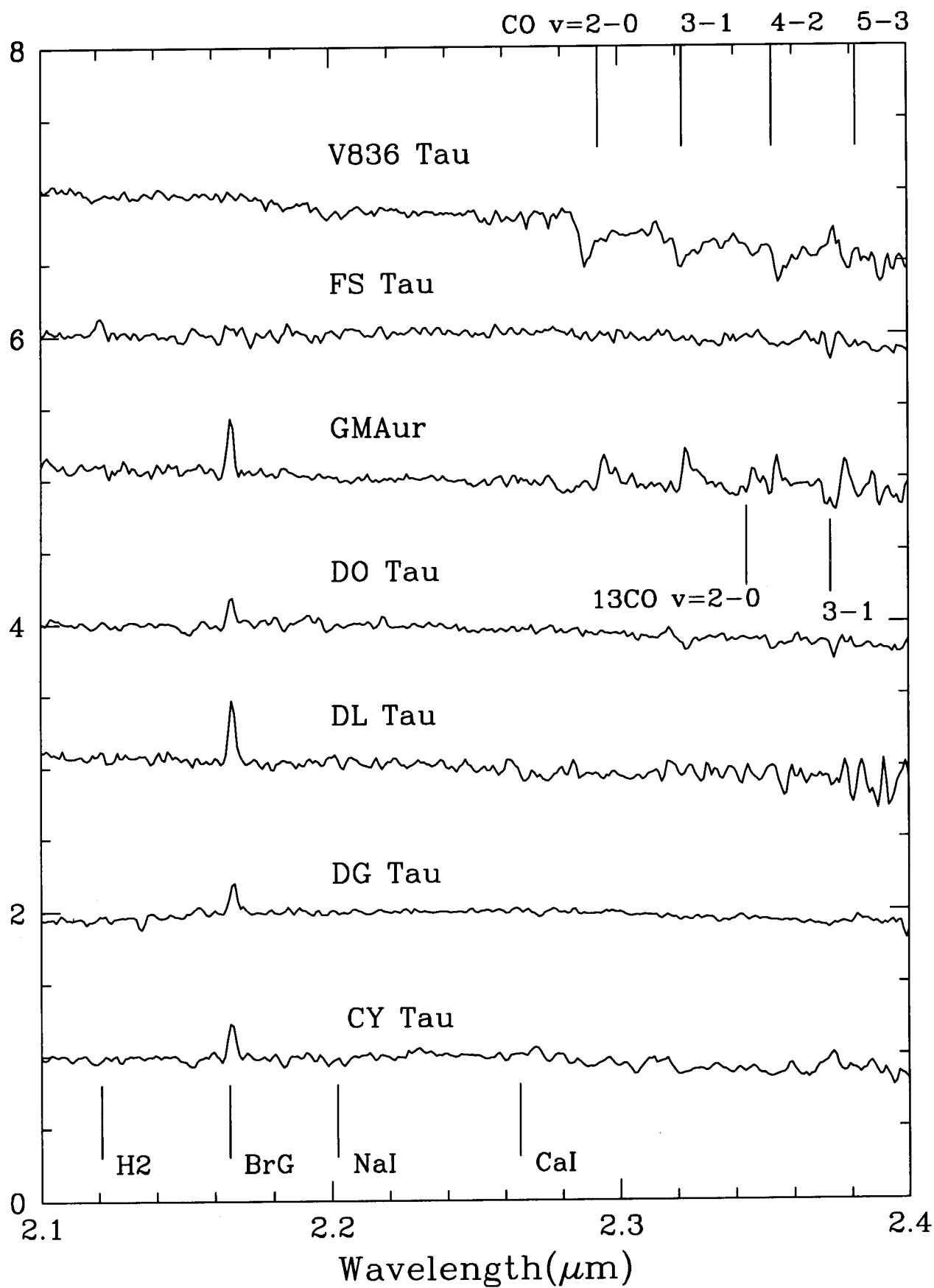


Figure 4.1: K band Spectra of Disk Candidates.

Table 4.2: Br γ Equivalent widths of the sample

Star	CI Tau	CY Tau	DG Tau	DL Tau	DO Tau	FS Tau	GM Aur
Br γ eqw (in Å)	-8.2	-8	-6.7	-11.6	-8	-	-10

Table 4.3: CO Equivalent widths of the stars with significant features

	$^{12}\text{CO } v=2-0$	$v=3-1$	$v=4-2$	$v=5-3$	$^{13}\text{CO } v=2-0$	$v=3-1$
GM Aur	-22	-21	-27	-8	-10	-16
V836Tau	45	45	59	34	-	12
DO Tau	-	7	7	4	-	-

depending upon the magnitudes of the sources. We observed all the sources with almost the same integration time which has resulted in this varying noise level. Out of the observed 7 sources, 4 reveal smooth spectra without any CO features. H₂ emission at 2.122 μm is found only in one source namely FS Tau. Discussion of individual objects is given below.

4.4.1 FS Tau

FS Tau or FS Tauri A (Haro 6-5) is the brighter one of the FS Tau pair, the other component being the well known Haro6-5b that has been imaged both in optical and infrared bands by the HST. Lunar occultation observations of this object revealed a binary system with a companion 0.25'' away (Chen et al. 1990, Simon et al. 1992). The spectral type is therefore composite and was estimated to be M1 type by Cohen and Kuhi (1979). This is one of the relatively highly polarized ($\sim 10\%$) T Tauri stars indicating the possible presence of a circumstellar disk (Gledhill & Scarrott 1989). HST images in the V, R and I bands have been discussed by Krist

et al.(1998). They also publish the photometry of the individual sources in the FS Tau system.

Our spectrum (Fig 4.1) shows that there are no absorption features of either atomic or molecular origin. However, H₂ emission is the only feature seen in this spectrum and this is the only object in our sample that has detectable H₂ emission at 2.122 μ m. Given that the star is M1 type and has a SED of type II, the absorption features should have been present in the spectrum. The absence of the CO overtone features therefore clearly indicates veiling due to the continuum emission from a hot circumstellar disk. This observation supports the large polarization values measured by Gledhill & Scarrott (1989) in confirming the existence of a disk. The observed H₂ emission coming from the unresolved binary system (0.3'') strongly indicates the possibility that the companion is an Infrared Companion (IRC) (Herbst et al. 1995, Koresko et al. 1997). The Kinematic data shows the presence of a low velocity component of -5 km s⁻¹. However, the detection of [NII] at 6583Å suggests the presence of a high velocity component (HVC)(\sim 50 - 150 km s⁻¹) (see Hirth et al. 1997 and references therein). It is not possible to associate the H₂ emission to either of these components since the HVC's dissociate H₂ and the low velocity component is not significant enough to excite H₂. Further, the interpretation that the binary companion to FS Tau A is an IRC is supported by the photometric observations of this source by HST/WFPC2 observations. K98 report that the fainter companion of FS Tau A which they refer to as FS Tau E is redder than the brighter companion that is referred to as FS Tau W. The flux ratio of the W/E is 18.5 in the V band and 7.3 in the I band. They also note that the flux ratio of the W/E stars is 8.2 obtained by using the photometry provided by Simon et al.(1992). Therefore we believe that the observed H₂ emission from the FS Tau binary system must be originating in accretion shocks associated with an IRC, which should be the fainter companion identified as FS Tau E.

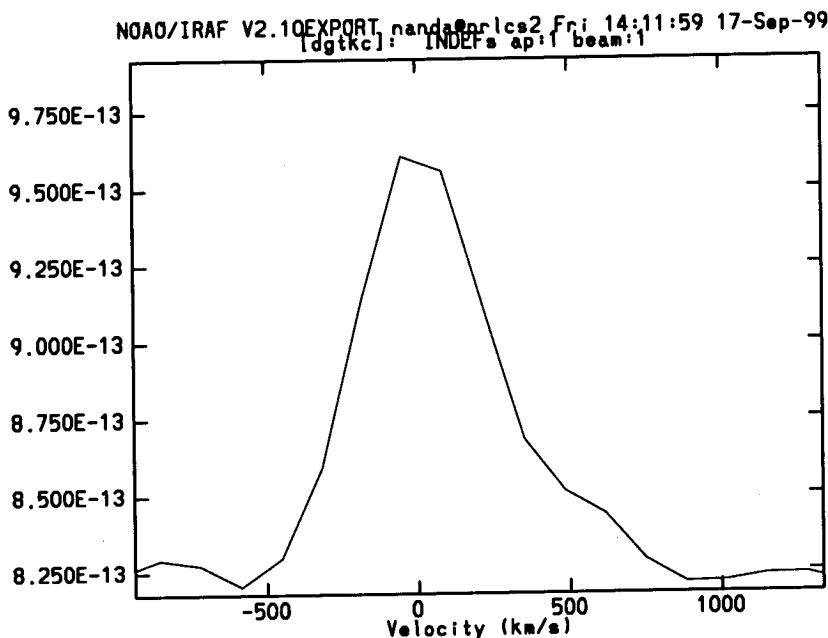


Figure 4.2: Br γ line profile of DG Tau. The y-axis represents flux in units of watts $\text{m}^{-2} \mu\text{m}^{-1}$.

4.4.2 DG Tau

DG Tau here is actually referred to as DG Tau A that is the brighter one of the pair DG Tau A and B. DG Tau B is 1' southwest of DG Tau A and has been imaged by HST. DG Tau B is one of the strongest sources seen in the 2.7mm maps of D96. The 2.7mm continuum emission contours clearly show a face-on disk. DG Tau A was first identified by Mundt and Fried (1983), as the source of an HH jet. Their H α CCD frame shows a bright HH knot 8" SW of DG Tau A (P.A. = $228^\circ \pm 2^\circ$) apparently connected by a jet. A coude spectrogram shows direct evidence for a stellar wind provided by the NaD lines which show broad blue absorption troughs with velocities up to -200 km s^{-1} . Bastein (1982) presented optical polarization data of this star which shows 6% polarization with the electric vectors oriented at an angle of P.A. = $135^\circ \pm 1^\circ$. This direction is perpendicular to the direction of the observed jet and therefore Mundt and Fried attribute it to the presence of a disk around DG Tau.

DG Tau is the next spectrum in our sample that is remarkably smooth with no spectral features except for Br γ emission. The argument of continuum veiling of the

photospheric features holds in this case too, since the star is classified to be of spectral type K7-M0 type where one would expect to see these features. The absence of these CO features therefore confirms the presence of a disk supporting the polarization data of Bastein (1982). A 2.1-2.4 μ m spectrum of DG Tau was obtained by Hamann et al. (1988) who reported CO bandheads in emission. The observations of Carr (1989) and Tokunaga (1995) showed the CO in emission whereas Greene and Lada (1996) observed this object during 1993-1994 and found that the CO is in slight absorption. Our spectra do not show any emission of CO bandheads but indicate a possible weak absorption. These observations point to alternate phases of emission and no emission of the CO bands in the spectra. DG Tau is one of the two objects in the survey of D96 that showed detectable CO emission from the disk whereas the other sources had no emission.

The Br γ emission line is clearly broadened and assymmetric. Najita et al. (1996) have presented the Br γ line profiles of DG Tau. The line profile of the Br γ emission of DG Tau from our spectra is presented in Fig 4.2. The assymmetric nature of the profile is clearly seen with a possible second component that is red shifted at $\sim 450 \text{ km s}^{-1}$. The FWHM of the lines are $\sim 400 \text{ km s}^{-1}$. The broad line wings can be attributed to large scale turbulence in the stellar magnetosphere and can partly be due to scattering of photons by electrons as described in *section 4.3*.

4.4.3 *GM Aurigae*

The object is well known since it was one of the first objects to be mapped in the ^{13}CO J=2-1 line at 1.3mm using the IRAM interferometer at 0.6'' resolution by Dutrey et al.(1998). These authors demonstrate the Keplerian nature of the disk using CO images and also resolve a dust disk (using 2.7mm continuum) at the center of the CO disk. A 2.7mm image of GM Aur is published by D96. It has been imaged in the optical bands by HST/WFPC2 (S97). There is a remarkable correlation in the morphology of the interferometer image and HST image. The WFPC2 image reveal a flattened circumstellar reflection nebula extending symmetrically

from the star to radial distances of 3" (450AU) along position angle 60°. This nebulosity is attributed to the illuminated upper surface of a flared, optically thick disk observed from $\sim 25^\circ$ above the equatorial plane of the disk (S97). D98 have derived several parameters of the disk from their studies and estimate a dust disk mass of $0.025 M_\odot$ extending upto ~ 200 AU. Their CO maps, however, show a large Keplerian disk extending upto ~ 525 AU from the star.

A near-infrared spectrum of this source has been obtained by us. Our spectrum of GM Aur in Fig 4.1 shows the CO overtone features to be strongly in emission. This result is in support of the presence of CO gas in the disk seen by the HST and mm emission images. Also, the description of the disk as "flared" by S97 is supported by the emission features in our spectrum. The excitation of the CO gas within the optically thick disk can result in the strong emission of these overtone features. Our spectra also show intense Br γ emission that is explained using magnetospheric infall fed through a disk. The atomic absorption features are totally missing in our spectra. This can be accounted for by continuum emission from the central hot disk overfilling the photospheric atomic features.

4.4.4 *DL Tau*

This is a class II source which has been included in many surveys as a sample source from the Taurus-Auriga molecular cloud. However, to the best of our knowledge it has been studied as an individual object only by D96 through their millimeter continuum maps. The 2.7mm dust emission from an associated Keplerian disk is prominent and extended. The morphology suggests a face-on disk. Our spectrum shows intense Br γ emission and the CaII absorption feature at a 2σ level. The Br γ emission profile is asymmetric towards the red, suggesting infall signatures in a magnetosphere. The CO overtone features are missing in this object too, suggesting the presence of a disk and thus conforming to the millimeter images of D96.

4.4.5 DO Tau

This classical T Tauri star is associated with an arc-like reflection nebula. The 2.7mm continuum images of D96 shows a face-on Keplerian disk with an estimated dust disk mass of $0.019 M_{\odot}$. Hirth et al. (1997) have studied the forbidden line emission in visible from this object and demonstrated the existence of an outflow with the blue shifted lobe oriented at $\text{P.A.} = 250^{\circ} \pm 10^{\circ}$. This is nearly perpendicular to the optical polarization angle of $\text{P.A.} = 175^{\circ} \pm 2^{\circ}$ found by Bastien (1982). Our spectra of DO Tau reveal shallow ^{12}CO absorption features. This maybe due to the fact that the CO features are not veiled sufficiently owing to the inclination angle(face-on) of the disk. It also shows $\text{Br}\gamma$ in emission with a broadened profile at 400 km S^{-1} .

4.4.6 CY Tau

CY Tau is a class II source and a CTTS. The 2.7mm continuum emission images of D96 show a tilted disk with intense emission. The tilt appears to be about 30° to the line of sight. Our spectrum shows $\text{Br}\gamma$ emission and the photospheric absorption features are at the 1σ level. The $\text{Br}\gamma$ line profile is broad with FWHM of $\sim 400 \text{ km s}^{-1}$.

4.4.7 V836 Tau

This is the only SED class III source and a weak-line T Tauri star in our sample. This is a single star which shows very faint 2.7mm continuum emission (that too, not in a disk pattern) in comparison with the other strong sources discussed above. Our spectra display strong absorption features of CO bands and also those of NaI and CaI. The features are in accordance with the K7-M0 type photosphere of this star. This verifies the anti-correlation result of the association of CO features with the dust emission in disks. As a Class III source it is expected that this star has expelled most of the circumstellar material. Hence the photospheres are revealed,

the features of which are clearly seen in our spectrum.

4.5 Conclusions

We obtained near-infrared spectra of stars that are known to have Keplerian disks by direct imaging in the millimeter by IRAM interferometer or those which had strong observational evidences for having disks. In this process we provide direct verifications of the interpretations of the spectral features in the $2.1\text{-}2.4\mu\text{m}$ band with regard to the presence of disks and flows in the near environments of the YSO's. The hot inner disks and warm outer disks appear to co-exist and are in Keplerian motion. The presence of $\text{Br}\gamma$ line emission in almost all cases suggests ongoing accretion through funnel flow in the magnetosphere of the young star. Some specific results on individual objects have been obtained. We identify that one of the companions in the FS Tau binary to be an Infrared Companion, since we find molecular hydrogen emission at $2.122\mu\text{m}$ from this unresolved pair. We point out that HST/WFPC2 results provide supporting proof to the characterization of the FS Tau companion as an IRC. We note that DG Tau, which is known to show CO overtone bands in phases of emission and absorption during the last several years is currently showing neither absorption nor emission. The existence of CO in the disk of GM Aur is confirmed by the presence of CO overtone emission bands in our near-IR spectra.

पुस्तकालय THE LIBRARY
भौतिक अनुसंधान प्रयोगशाला
PHYSICAL RESEARCH LABORATORY
नवरंगपुरा, अहमदाबाद 380 015
NAVRANGPURA, AHMEDABAD-380 005
भारत / INDIA

4.6 References

- Bastien, P., 1982, A&ASS, 48, 153
- Basri, G., & Bertout, C., in Eds., Levy, E. H., & Lunine, J., 1993, Protostars and Planets III, University of Arizona Press.
- Beckwith, S. V. W., Sargent, A. I., Chini, R. S., Gusten, R., 1990, AJ, 99, 924
- Carr, J. S. 1989, ApJ, 345, 522
- Casali, M. M., & Matthews, H. F., 1992, MNRAS, 258, 399
- Casali, M. M., & Eiroa, C., 1996, A&A, 306, 427
- Chen, W. P., Simon, M., Longmore, A. J., et al. 1990, ApJ, 357, 224
- Cohen, M., & Kuhl, L. V., 1979, ApJS, 41, 743
- Dutrey, A., Guilloteau, S., Duvert, G., Prato, L., Simon, M., Schuster, K., & Menard, F., 1996, A&A, 309, 493.
- Dutrey, A., Guilloteau, S., Duvert, G., Prato, L., et al., 1998, A&A, 338, L63
- Greene, T. P., & Lada, C. J., 1996, AJ, 112, 2184
- Greene, T. P., & Meyer, M. R., 1995, ApJ, 450, 233
- Gledhill, T. M., & Scarrott, S. M., 1989, MNRAS, 236, 139
- Hartmann, L., Calvet, N., Avrett, E. H., & Loeser, R., 1990, ApJ, 349, 168
- Hamann, F., Simon, M., & Ridgway, S. T., 1988, ApJ, 326, 859
- Herbig, G. H., & Bell, K. R., 1988, Lick Obs Bull No. 1111.
- Herbst, T. M., Koresko, C. D., Leinert, C. 1995, ApJ, 444, L93
- Hirth, G. A., Mundt, R., & Solf, J., 1997, A&ASS, 126, 437.
- Hodapp, K.-W., & Deane, J. 1993, ApJS, 88, 119

- Kenyon, S. J., & Hartmann, L., 1995, *ApJSS*, 101, 117.
- Koresko, C. D., Herbst, T. M., & Leinert, Ch., 1997, *ApJ*, 480, 741
- Krist, J. E., Stapelfeldt, K. R., et al. 1998, *ApJ*, 501, 841
- Mundt, R., & Fried, J. W., 1983, *ApJ*, 274, L83
- Mundt, R., Buhrke, T., Fried, J. W., et al. 1984, *A&A*, 140, 17
- Muzerolle, J., Hartmann, L., & Calvet, N., 1998, *AJ*, 116, 2965
- Natta, A., Giovanardi, C., & Palla, F., 1988, *ApJ*, 332, 921
- Najita, J., Carr, J. S., & Tokunaga, A. T., 1996, *ApJ*, 456, 292
- Simon, M., Chen, W. P., Howell, R. R., et al. 1992, *ApJ*, 384, 212
- Stahl, O., & Wolf, B., 1980, *A&A*, 90, 338
- Stapelfeldt, K., Burrows, C. J., Krist, J. E., & WFPC2 Science Team, in B. Reipurth, & C. Bertout, (Eds.). *Herbig-Haro Flows and the Birth of Low Mass Stars*, 355, IAU 187, Kluwer Academic Publishers.
- Tokunaga, A. T., 1995, Private Communication to Greene & Lada

L1340 : A star forming cloud

5.1 Introduction

This chapter describes the optical and near-infrared studies of an active star forming cloud in the constellation of Cassiopeia. The regions of Cassiopeia and Cepheus have been recently surveyed by Yonekura et al. (1997), in the CO lines using the 4 m radio telescope of the Nagoya University, with a grid spacing of 8'. The large scale survey has identified several molecular clouds in this region that were previously unknown. These authors have presented the detailed CO maps of the molecular clouds in the region and have identified the associated IRAS sources. These IRAS sources represent young objects in these molecular clouds and therefore indicate star formation activity. Based on these maps, and other factors that are symbolic of star formation activity, we selected some of the regions to survey for new Herbig-Haro objects. Herbig-Haro objects are optical counterparts of molecular outflows and are clear sign-posts of on-going star formation activity (see *Chapter 1*).

One of the most interesting molecular clouds we chose for our study (from Yonekura et al. 1997) is identified as L1340 in the catalog of dark clouds by Lynds (1962). It is a small cloud of area 0.01 square degrees with central coordinates of $\alpha(1950) = 02^h26^m$, $\delta(1950) = +72^\circ44'$. The cloud has been studied extensively for the first time by Kun et al. (1994)(hereafter K94). They made detailed ^{13}CO and C^{18}O maps of this cloud and conducted objective prism observations and photoelectric photometric studies of several young stellar objects in this cloud. These

authors estimate a distance of 600pc to L1340, and a mass of 1100 M_{\odot} using the ^{13}CO and C^{18}O maps of the molecular cloud. They also identify three dense cores of masses 280, 470 and 180 M_{\odot} using the C^{18}O observations identified as A, B, C by K94. NH_3 maps of the dense cores associated with the cloud are discussed by Kun et al.(1999) (hereafter K99). The objective prism plate studies of K94 resulted in the identification of 13 H_{α} emission stars and 22 IRAS point sources within the 1 square degree area of the CO cloud. The visible area of the cloud is associated with three red and nebulous objects namely RNO7, RNO8 and RNO9 listed in the catalog of Cohen (1980). Indeed, these objects are closely associated with the three cores of the cloud. The identification of 17 low and intermediate mass stars in this region by K94, indicating a high rate of star formation, strengthened our motivation to look for new HH objects in this region. Cohen's red and nebulous objects associated with this cloud were also promising objects for a detailed study in the optical and NIR. The results of such a study are presented in this chapter along with a picture gallery of the newly discovered HH objects.

5.2 *Observations and Data Reduction*

The initial study of some regions of this cloud were made using the optical observations obtained with the 2.3 m telescope and a $1\text{k} \times 1\text{k}$ CCD at Vainu Bappu Observatory, Kavalur, India in a collaborative effort with Kajal Ghosh of Indian Institute of Astrophysics, Bangalore. Follow up observations that included a much larger area of the cloud were made possible by Bo Reipurth, John Bally and Ka Chun Yu of CASA, Colorado, USA. These observations were made using the new MOSAIC camera on the 0.9 m telescope of the Kitt Peak National Observatory. The MOSAIC camera is a $8\text{k} \times 8\text{k}$ mosaic consisting of eight thinned $2\text{k} \times 4\text{k}$ CCD's that provides a plate scale of $0.423''/\text{pixel}$ covering approximately one degree field of view on the sky. A log of the observations is given in Table 5.1. Near-infrared images of the RNO7,8 and 9 regions were obtained using PRLNIC on the 1.2 m Gurushikhar telescope (see *Chapter 2*).

Data reductions of the MOSAIC images were carried out in parts at PRL by the author and at CASA by Kachun Yu, using the *MSCRED* IRAF external package which is exclusively meant for handling MOSAIC data. MOSAIC raw data comes in the form of eight inter-connected "fits" files that are due to the eight $2k \times 4k$ CCD's. These individual images are reduced using standard CCD routines with the exception that they are performed on the mosaicked image. Flat fielding was carried out by using a sky flat that was generated by combining 40 frames taken during the night. Dome flats are relatively ineffective for MOSAIC images since the large scale variations become prominent over the wide field of view of the CCD camera. Each reduced image is 279MB in size and consumes a considerable amount of memory and processing time depending on the computer. The reduced image was calibrated using DSS for performing astrometry. Results from the analysis of the central regions of the CO cloud are presented in this chapter. A small region of the cloud associated with the RNO9 outflow was mapped in the emission lines of ^{13}CO , C^{18}O , and CS molecules in the millimeter region. These data were obtained and reduced for us by Rafael Bachiller, OAN, Spain, at the 30 m IRAM telescope at Pico Veleta, Spain.

5.3 *L1340 cloud and the Cohen's objects*

Three among the Red and Nebulous Objects (RNO's) cataloged by Cohen (1980) are closely associated with the dense cores of the L1340 cloud. These objects were included in the FOV of our CCD enabling us to study their optical properties. Near-infrared K' observations of all the three objects were carried out to identify deeply embedded sources and to check for star formation activity. As described by K94, L1340 has three dense cores identified as A ($280 M_{\odot}$), B ($470 M_{\odot}$), and C ($180 M_{\odot}$). Core A has two parts with a bright peak and a relatively fainter peak that is well separated from the brighter peak. We reproduce in Table 5.2, some important parameters of these cores from K94. T_{ex} , τ , R , n represent excitation temperature, optical depths, radius and number density respectively in Table 5.2.

Table 5.1: Exposure Log for the KPNO Mosaic Images

Filter	CWL (\AA)	FWHM (\AA)	Exp (sec)
GunnZ	9400	2000	250
H $_{\alpha}$	6559	80	1000
[SII]	6730	81	1000

Table 5.2: Observed properties of L1340 Cores

Core	T $_{ex}$ (K)	$\tau(^{13}\text{CO})$	$\tau(\text{C}^{18}\text{O})$	n(H $_2$) (10^{21}cm^{-3})	Mass (M_{\odot})	Size pc \times pc	R (pc)
A	10.2	0.33	0.06	850	280	2.8 \times 1.2	0.9
B	13.1	0.24	0.07	830	470	3.3 \times 1.5	1.1
C	9.1	0.56	0.13	1200	180	1.7 \times 1.3	0.7

5.3.1 RNO7

RNO7 is described in the Cohen's catalog as "*star, bright, red, closely nebulous*" and the spectrum of this object reveals H $_{\alpha}$ emission line. There are two H $_{\alpha}$ emission stars and a couple of IRAS sources associated with this object. The object is a cluster of stars embedded in optical nebulosity as seen on the POSS prints. Figure 5.1 shows the contour maps of GunnZ, [SII] and H $_{\alpha}$ images along with a grey-scale K' image of RNO7. The most striking feature in this object is a candidate HH jet marked in Fig 5.1. The jet-like feature is seen strongly in [SII], relatively weak in H $_{\alpha}$, and missing from the GunnZ image. The feature appears to originate from the IRAS source 02236+7224 which also happens to be a bright H $_{\alpha}$ emission star identified by K94. Although these properties satisfy the criteria for an HH jet, the relative faintness and the fact that it is embedded in the surrounding optical nebulosity, calls for deeper images and continuum-subtraction to prove the HH nature.

Within the observation limits, our K' image does not reveal any apparent nebulosity associated with the cluster. It shows 33 stars with 20 stars concentrated in the central region ($\sim 2' \times 2'$). 3 sources appear to be infrared sources since they

are seen only in the K' image and 2 other sources are relatively bright in K' image compared to the GunnZ image. The C¹⁸O maps of K94 show relatively thin emission from the core associated with RNO7 and the NH₃ maps of K99 do not show any emission from this region. These results imply that the density of molecular material is low in the region surrounding RNO7. The relative absence of the K' nebulosity, the presence of bright infrared sources and a cluster of stars that are bright in the red and infrared together suggest that RNO7 could be an young cluster that has formed out of a dense core. The stars are most likely in the process of dispersing the surrounding material. The relatively low density of the molecular material surrounding this object can be explained by this argument. However, photometry of the RNO7 stars in the near-IR bands can clearly prove their youth and properties as a cluster.

5.3.2 RNO8

RNO8 is described in the Cohen's catalog as faint and purely nebulous. It is found close to the reflection nebula DG9 seen as a star + nebulosity. RNO8 has an appearance of a bipolar nebula with a faint star situated at the center of the nebula. Figures 5.2, 5.3, 5.4 & 5.5 show the GunnZ, K', H_α and [SII] images of the RNO8 region respectively. There is no noticeable difference in the images except that the nebulosity is not registered in our infrared image. The bipolar nebulosity is relatively brighter in the H_α and [SII] images as compared to the GunnZ image and these images are not presented here. This suggests that the nebulosity is due to hotter gas. The relative brightening of the nebula in the H_α and [SII] bands suggests the influence of a wind that is most likely originating from the central star which is known to be a bright IRAS source. According to K94, this star is the most luminous source of the cloud and they classify it as a protostellar source of intermediate mass. RNO8 is situated closely on the core B of L1340. Surrounding RNO8 and associated with core B are stars R1-4 identified as A and B type stars by K94. Core B is thus shown by K94 to be forming intermediate mass stars.

5.3.3 RNO9

RNO9 is described as "two stars, brighter is redder, very faint nebula to the south" in Cohen's catalog. The second generation POSS prints show a clear arc-like nebulosity associated with the star. RNO9 falls on the edge of the Core C which is the densest core of L1340. The ammonia emission is very thick and show 4 individual clumps that coincide with the C¹⁸O core. Two optically invisible IRAS sources are identified with this core by K94 and K99. Figures 5.6, 5.7, 5.8 & 5.9 show the GunnZ, K', H α and [SII] images of the RNO9 region respectively. The H α and [SII] images do not show any discernable differences in comparison to GunnZ image and therefore not presented here. The K' image was created by mosaicking two frames each of field of view 4' \times 4' with sufficient overlap between the two frames such that the central regions have a higher S/N ratio when mosaicked. The nebulosity associated with RNO9 is purely a reflection nebula and does not show any H α or [SII] emission. However, one of the nebulous blobs that coincides with the invisible IRAS source reveals an interesting object in our K' image. Figures 5.11 & 5.12 show the GunnZ and K' images of this object, with contours overlaid. The associated IRAS source is identified as F02267+7226 in the IRAS Faint Source Catalogue. The IRAS colors indicate an embedded source that is cooler and likely to be a driving source of an outflow. The colors for this source are $\text{Log}(F_{25}/F_{12}) = 0.209$ & $\text{Log}(F_{100}/F_{60}) = 0.301$ and is typical of Class I protostars. The K' contours show an elongated source with two features that appear to be outflowing from the source. Millimeter maps obtained with the 10" beam of IRAM centered on this object (see Fig 5.14 and 5.15) show very weak C¹⁸O emission, ¹³CO at a level of 4.5K and asymmetric profiles in CO. The CO line indeed shows a double component with a separation of about 3 km/s indicative of a weak outflow. Therefore, the object appears to be a class I source that is driving a weak outflow. There are no Herbig-Haro objects anywhere near this region that can be associated with this outflow. A second blob of nebulosity (marked c in 5.6) seen in the GunnZ image and POSS prints appears to be associated with a bright K' source (see figures 5.14 & 5.15). This source does not have any associated IRAS PSC listing.

Figures 5.12 and 5.13 show the ^{12}CO and ^{13}CO maps made around the RNO9 star, 5.14 and 5.15 show the C^{18}O and ^{13}CO maps made around the candidate outflow, 5.16 and 5.17 show the C^{18}O and ^{13}CO maps made around an infrared star (marked C in Fig 5.6). The velocity scale on the X-axis is from -18km/s to -12km/s and the brightness temperature on the Y-axis scale is from -1K to 6K, these scales being common to all the millimeter data presented in the figures. The ^{13}CO maps of K94 show a sudden velocity change at the edge of Core C, where the velocity changes from -14.5 to -12.8 km/s which is about 1.7km/s variation. This is the only positive velocity component of the cloud identified in their maps. RNO9 and the two nebulous blobs associated with infrared sources (marked B and C in Fig 5.6) all lie along the boundary of the velocity gradient in the ^{13}CO maps. Notice that the C^{18}O emission abruptly falls to the north-west direction in Figures 5.14 and 5.16. This represents the edge of the dense core. Fig 5.15 represents the ^{12}CO emission near the region of the outflow seen in the near-IR and the double profile is seen to the south-west direction. The millimeter maps were made prior to detecting the infrared sources and therefore the outflow shown in Fig 5.13 is not centered in the millimeter maps. However, all the maps, together suggest that the optical identification of RNO9-star, B and C blobs, all lie along the boundary of the dense core and along a line where there is a sudden velocity change. The double components separated closely at velocities of 2-3 km/s agree closely with the observations of K94. K94 suggest that this positive component in the velocity maybe associated with a small clump of cloud that is different from the main molecular cloud. But our K' images that revealed an outflow source, put together with our millimeter maps suggest that the velocity difference could be arising due to a weak outflow originating from the infrared source IRAS F02267+7226. Deeper images in the near-infrared are required to prove the exact nature of this source.

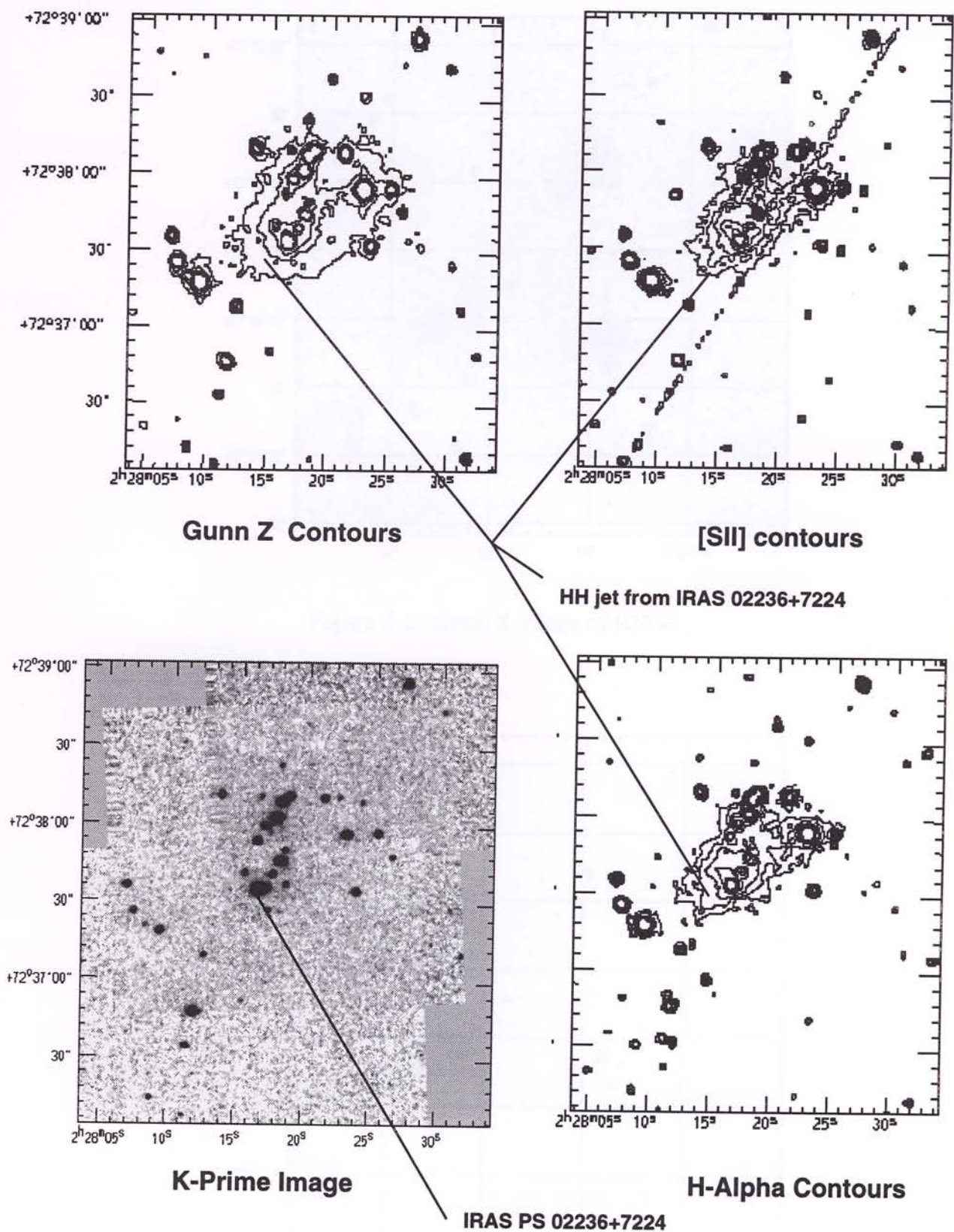


Figure 5.1: RNO7 Cluster and the embedded HH jet. The lowest contours represent 3σ levels above the mean background and are adjusted subsequently to show the HH candidate jet clearly.

Figure 5.3: K Prime Image of RNO8

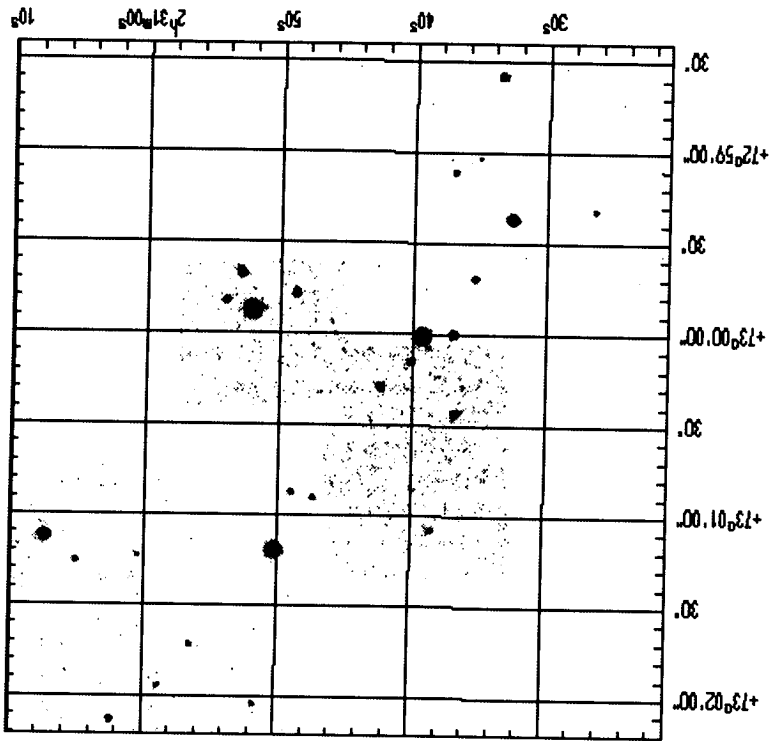
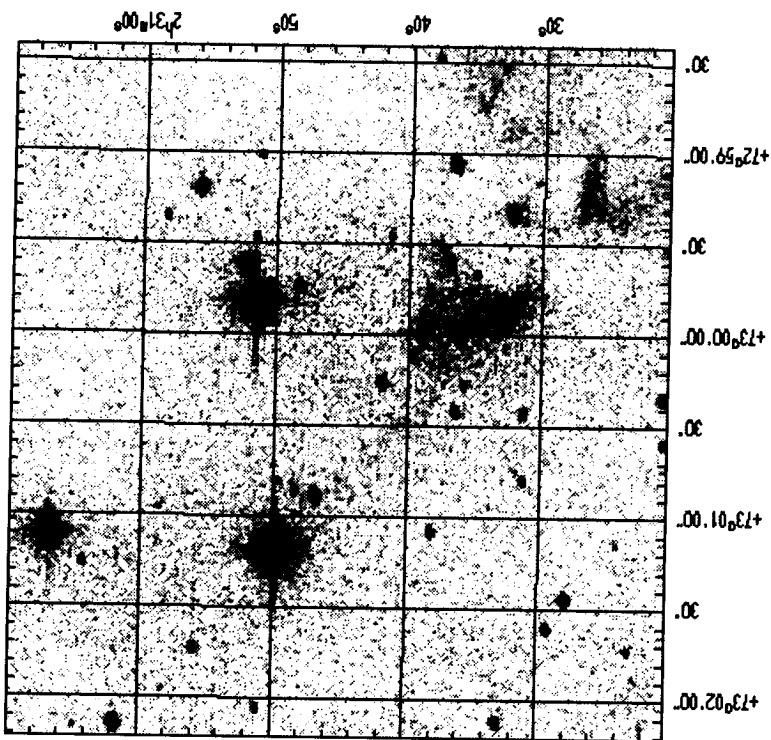


Figure 5.2: Gunn Z image of RNO8



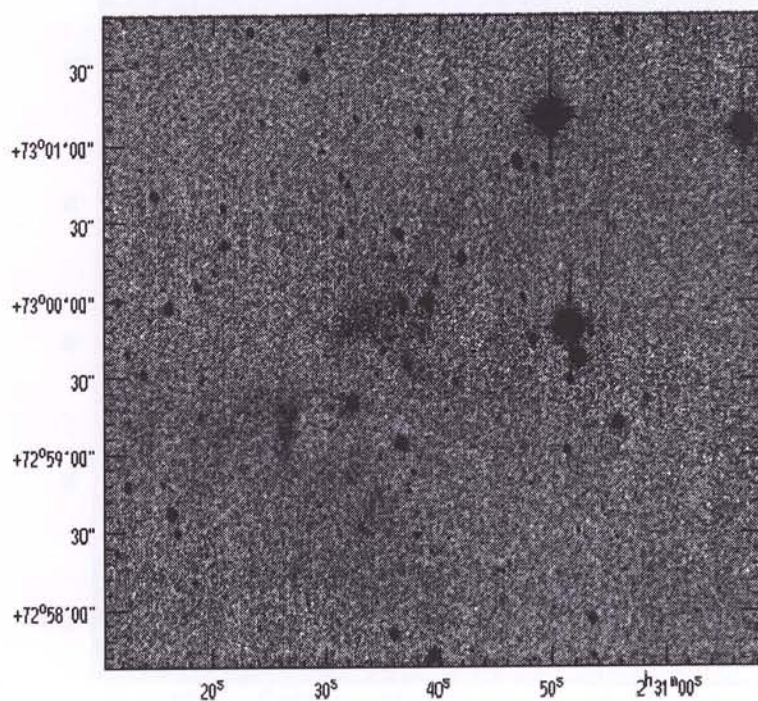


Figure 5.4: H α image of RNO8

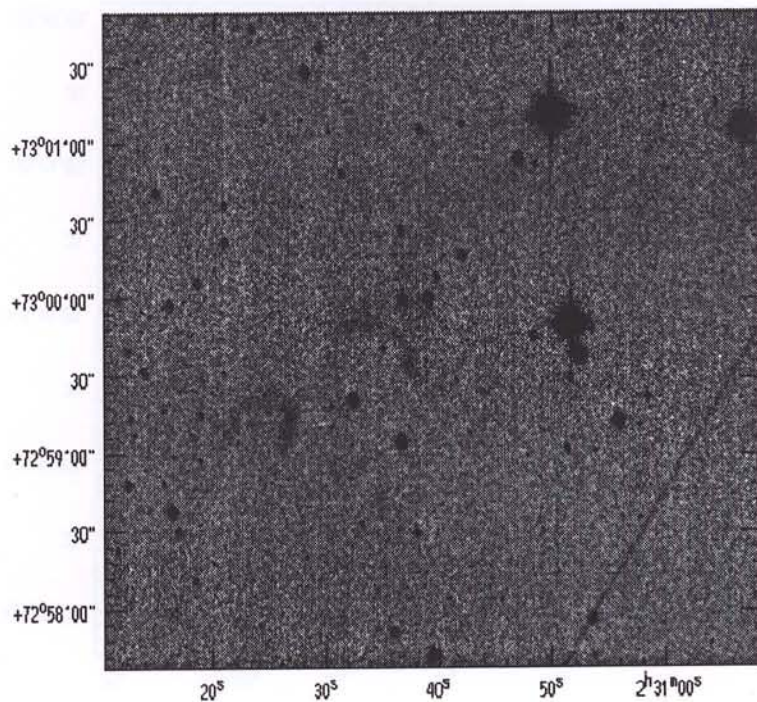


Figure 5.5: Sulphur Image of RNO8

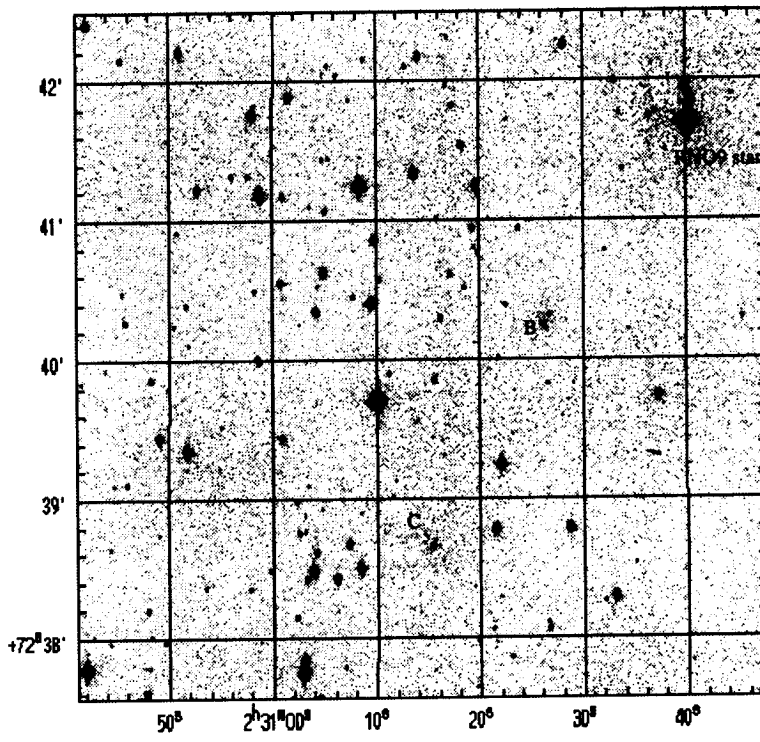


Figure 5.6: Gunn Z image of RNO9

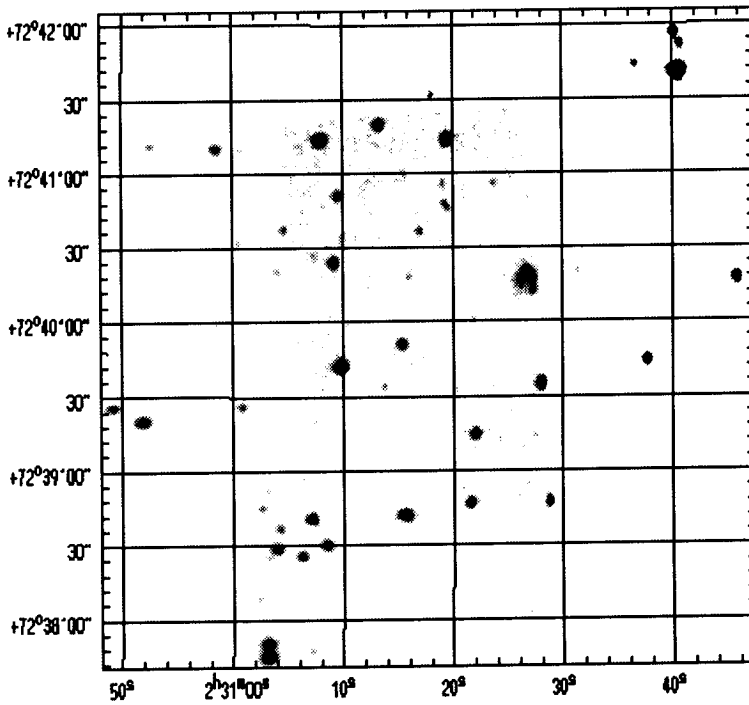


Figure 5.7: K Prime Image of RNO9

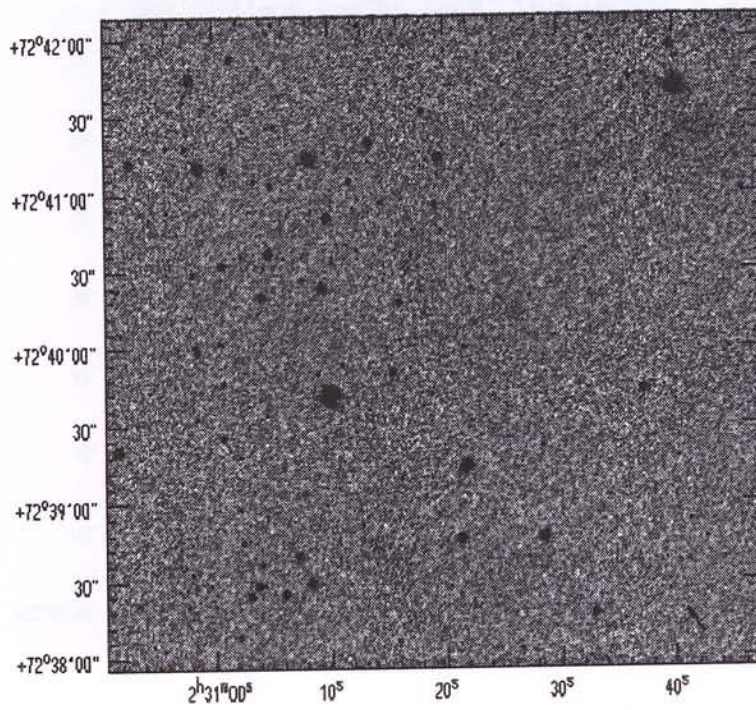


Figure 5.8: H α image of RNO9

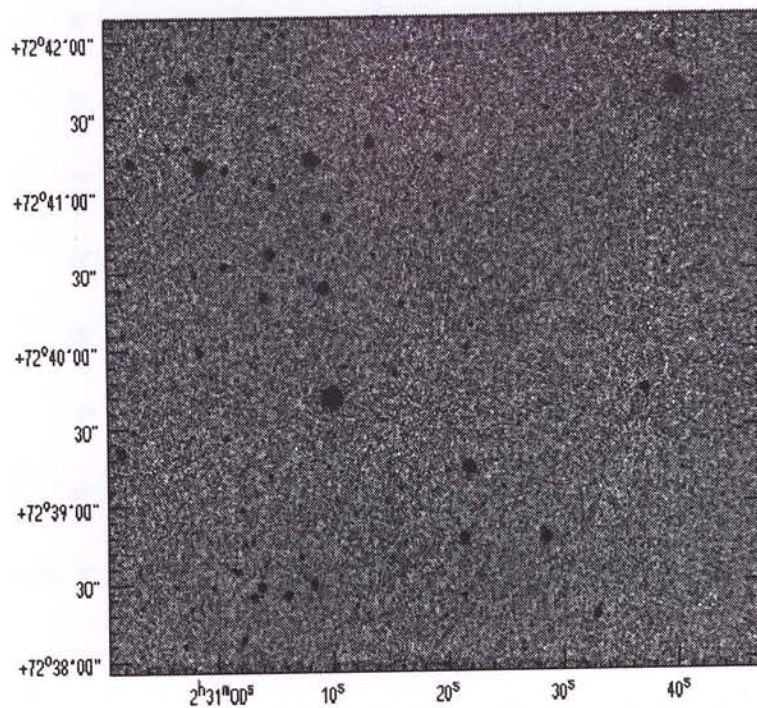


Figure 5.9: Sulphur Image of RNO9

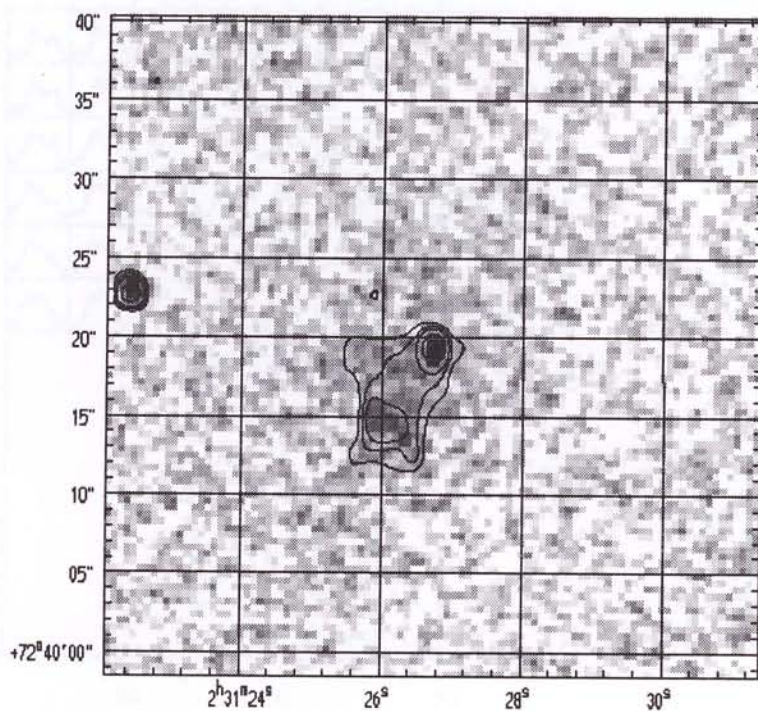


Figure 5.10: RNO9 Outflow Candidate (Gunn Z Contours)

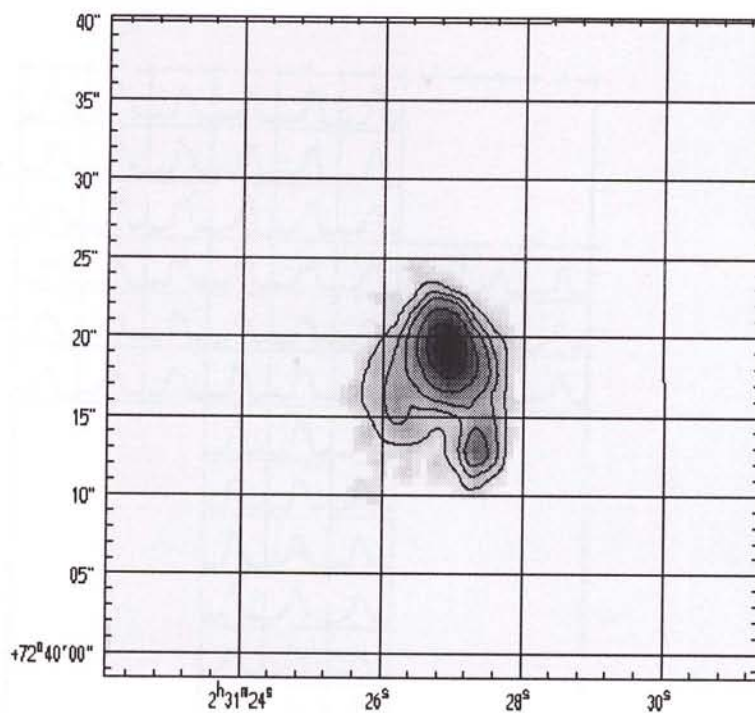


Figure 5.11: RNO9 Outflow Candidate (K Prime Contours) The lowest contour is 3σ above the mean background and adjusted subsequently to show the structure clearly.

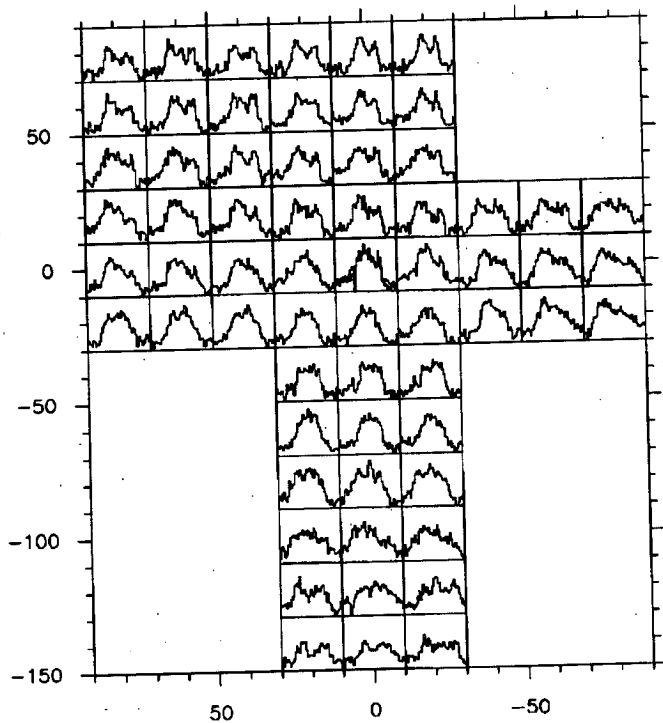


Figure 5.12: ^{12}CO emission around RNO9 star. The x-axis scale is from -18 to -12 km/s and y axis scale is from -1 to 6 K in each block. (0,0) corresponds to $\alpha = 02^h 31^m 42^s$ $\delta = 72^\circ 41' 24''$. Offsets are in arcsec.

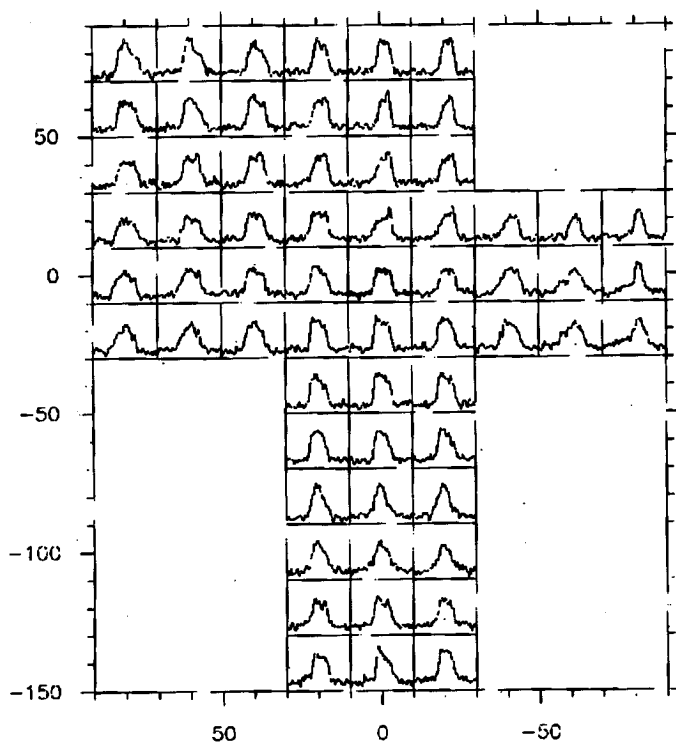


Figure 5.13: ^{13}CO emission around RNO9 star. x-y axis and offsets are same as above. Refer to text on page 85.

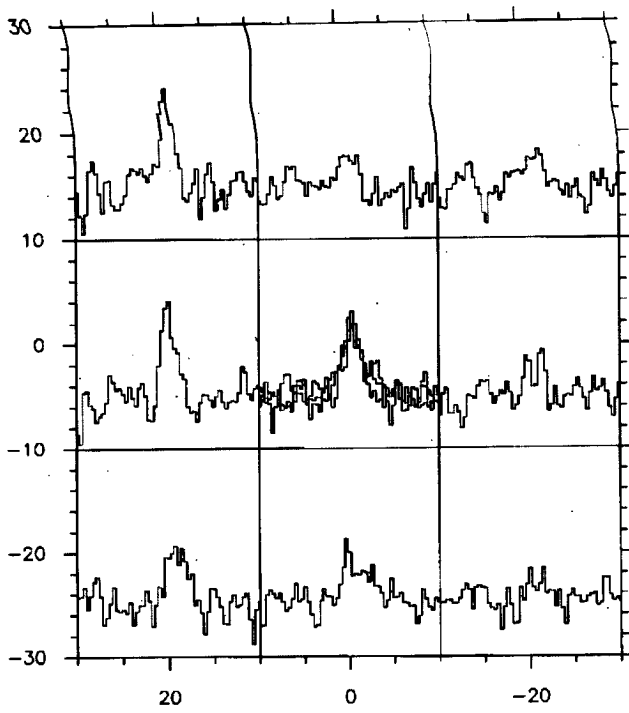


Figure 5.14: C^{18}O emission around RNO9 outflow candidate (RNO9-B) (ref Fig 5.6). (0,0) corresponds to $\alpha = 02^{\text{h}} 31^{\text{m}} 27^{\text{s}} \delta = 72^{\circ} 40' 17''$. Offsets are in arcseconds.

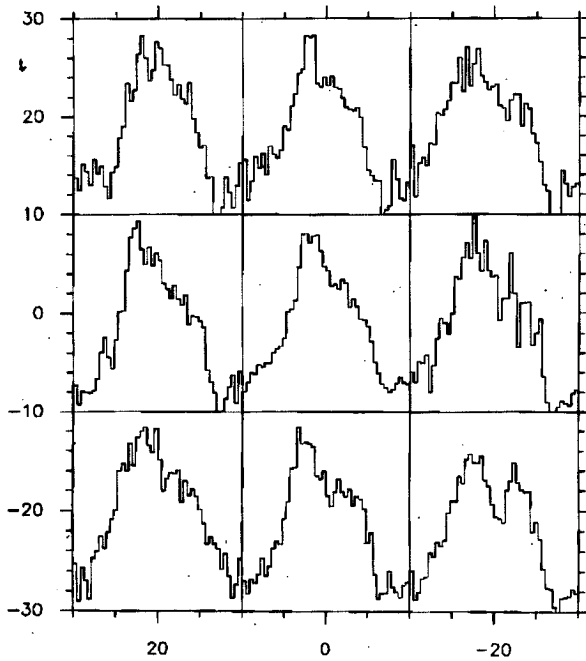


Figure 5.15: ^{13}CO emission around the outflow candidate. (0,0) is same as above

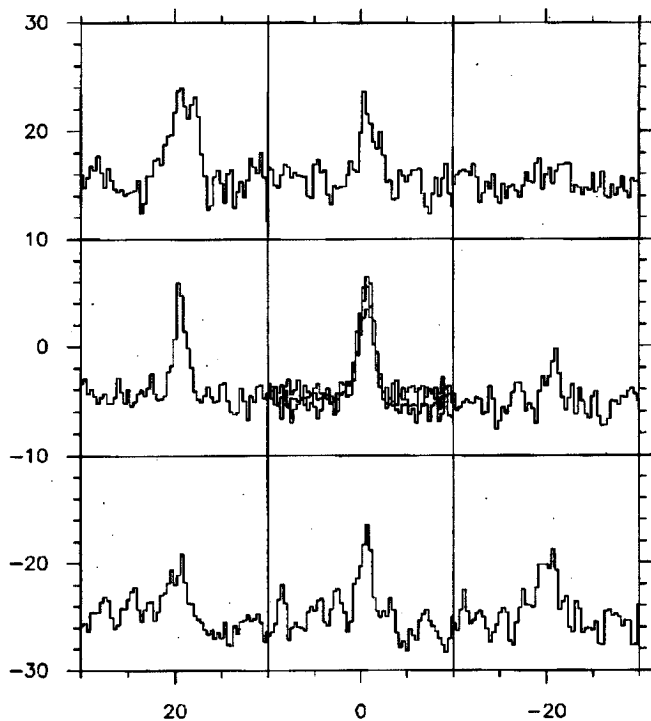


Figure 5.16: C^{18}O emission around RNO9-C (ref. Fig 4.4). (0,0) corresponds to $\alpha = 02^{\text{h}} 31^{\text{m}} 14^{\text{s}}$ $\delta = 72^{\circ} 38' 40''$

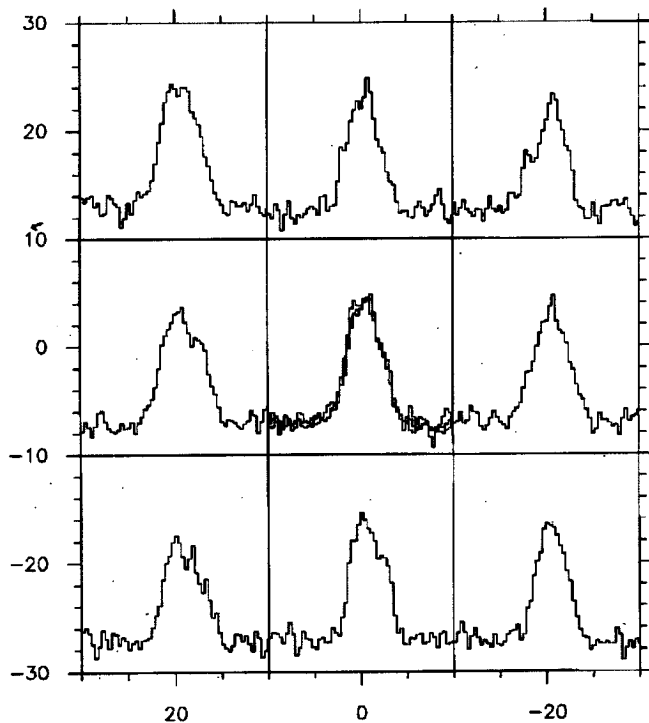


Figure 5.17: ^{13}CO emission around RNO9-C. (0,0) is same as above

5.4 *New Herbig-Haro Objects in L1340*

Herbig-Haro (HH) objects are known to astronomers as compact emission nebulae closely associated with young stars and represent regions of shocked material in the molecular clouds. Although there is no exact definition for these objects, a general consensus is that these are shocked regions closely associated with young stars and not with evolved stars. They are now understood to be due to an outflow from a young stellar object. The most complete catalog of these objects is published electronically by Reipurth (1994) which contains nearly 250 HH objects. HH objects show characteristic lines of shocked emission from [SII], [OII], and H. Although the clear proof for an HH object comes from a spectrum, a simpler method adopted by many astronomers to identify the HH objects, is to obtain narrowband images in the light of [SII] and H_α emission lines and a broad band image to measure the red continuum level. Objects that are seen only in the emission line images and not in the continuum images are identified as HH objects (see Reipurth 1994 for a detailed discussion). There are mainly two classes of HH objects that are known as high and low excitation objects based on the excitation level of the shocked material (Bohm & Goodson 1997). High excitation HH objects have typically higher ratios of H_α to [SII] in comparison with low excitation objects. Low excitation objects are brighter in [SII] emission as compared to H_α emission. Our search for new HH objects in the L1340 cloud has resulted in the discovery of HH objects associated with three flows. The new HH objects associated with these three flows are designated as HH487, HH488 and HH489 by Reipurth, and will be used as such in the following description. All the three flows appear to be associated with high excitation HH objects since they are brighter in H_α compared to [SII]. Note that the images are already normalized in the sense of S/N ratio by choosing the bandwidths of the filters (see Table 5.1) and appropriately scaled integration times. The co-ordinates of the individual features associated with these flows are listed in Table 5.2. The criteria used for identifying the driving sources are (i) a clear morphological connection between the features and the source and (ii) the presence

of a young stellar object like an IRAS point source or H_α emission star in the near vicinity of the HH objects.

5.4.1 HH487

Figures 5.18, 5.19 & 5.20 show the H_α , GunnZ and [SII] images of HH487 respectively. The GunnZ image is reproduced in Fig 5.21 to make the comparison with the [SII] image convenient. These are the brightest HH objects found in the region and have clear bowshock features and wisps. These are strong in the H_α emission and tips of the bowshock features are seen to be emitting in [SII]. The driving source of these shocks is still unclear since there are no known IRAS point sources or H_α emission stars in the nearby 1.2pc of these bowshocks nor any other HH objects that can be used to trace the origin. There is an IRAS source identified as 02224+7227 situated at about 1.3pc from these bowshocks and wisps with characteristics of an outflow driving source (see K94). The curvature of the bowshocks points to this source, but there are no obvious nebulous features that form a link between the source and the bowshocks which are separated by the large distance of 1.3pc. It is, therefore, difficult to associate the IRAS source with this HH object as the driving source.

5.4.2 HH488

Figures 5.22 & 5.23 show the H_α and GunnZ images of the HH488 region. Figures 5.24 & 5.25 respectively show the [SII] and H_α contours of source+jet. The flow HH488 is associated with a source that is lying to the south-east of RNO7 and at the boundary of the weaker component of the dense core A of the L1340 molecular cloud. The source is clearly associated with a jet-like feature that is connected to the seeing disk (see Figures 5.22, 5.24 & 5.25). Two HH knots, appearing as a binary star at about 0.8 parsec away from the source and a long strip of very faint nebulosity ending in a broadened bowshock-like structure can be associated with this flow. These features fall in a line that can be traced upto the source (see Fig

Table 5.3: New HH objects in L1340

Name	R. A. (J2000) h m s	Dec (J2000) ° ' "
HH487		
Bow 1	02 26 19	72 34 42
Bow 2	02 26 27.2	72 35 03
HH488		
Source+jet	02 28 00	72 35 58
knot 1	02 28 22.5	72 34 56
knot 2	02 28 40	72 34 16
HH489		
Source	02 29 43.2	72 43 59
IRASPSC 02249+7230	02 29 41.5	72 43 52
Knot	02 29 37.7	72 44 50

5.22). The boundary of these features are marked in Fig 5.22 to identify them clearly. A small tail from the source in this direction joins with the traced line. The "tail"-like feature is seen in the [SII] image contours (see Figure 5.24). The bowshock feature at the bottom right edge of Fig 5.22 is bright at the tip. Deep imaging of the region is required before a conclusive statement can be made about the association of these features to the driving source. The source can be seen to appear as a double star. The fainter companion is seen on the left of the brighter source in Figures 5.24 & 5.25. Interestingly, the brighter source that appears to be driving the jet is strong in the H_α and [SII] emission and not seen in the GunnZ image. The fainter source is seen in all the three filter images. The [SII] emission (Fig 5.24) shows a second flow that appears to be originating from the fainter companion. We note that this flow points to the bowshock features of HH487. Although there are no known IRAS PS's near this region, the jet+star shown in Figures 5.24 & 5.25 appear to be the source since there exists a clear morphological connection between all these features.

5.4.3 HH489

This is the most clearly identified optical flow so far in this region. Figures 5.26, 5.27 & 5.28 show the H_{α} , GunnZ and [SII] images respectively. The GunnZ image is reproduced in Fig 5.29 for a clear comparison of features with the [SII] image. The driving source is at the center of the frame and seen in all the three images. A HH knot is seen towards 1' north of the driving source. A faint wisp of nebulous material bridges the void between the knot and the source forming a connection. The nebulous wisp extends to the south of the driving source as well, but there are no HH objects found to the south, in these frames. The driving source is identified as IRAS 02249+7230.

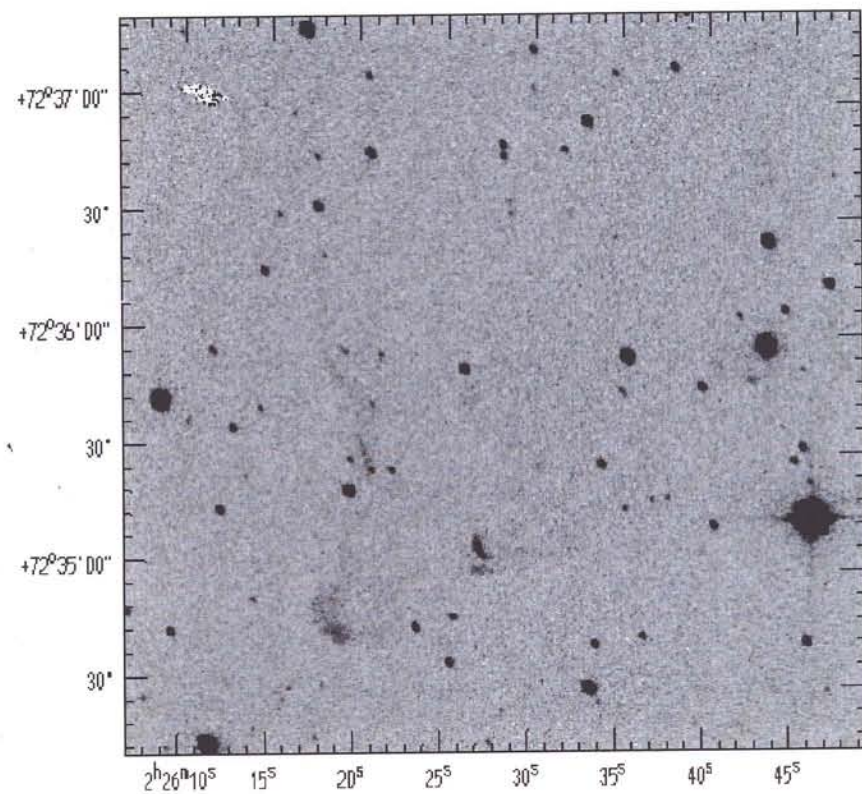


Figure 5.18: HH487 H α Image

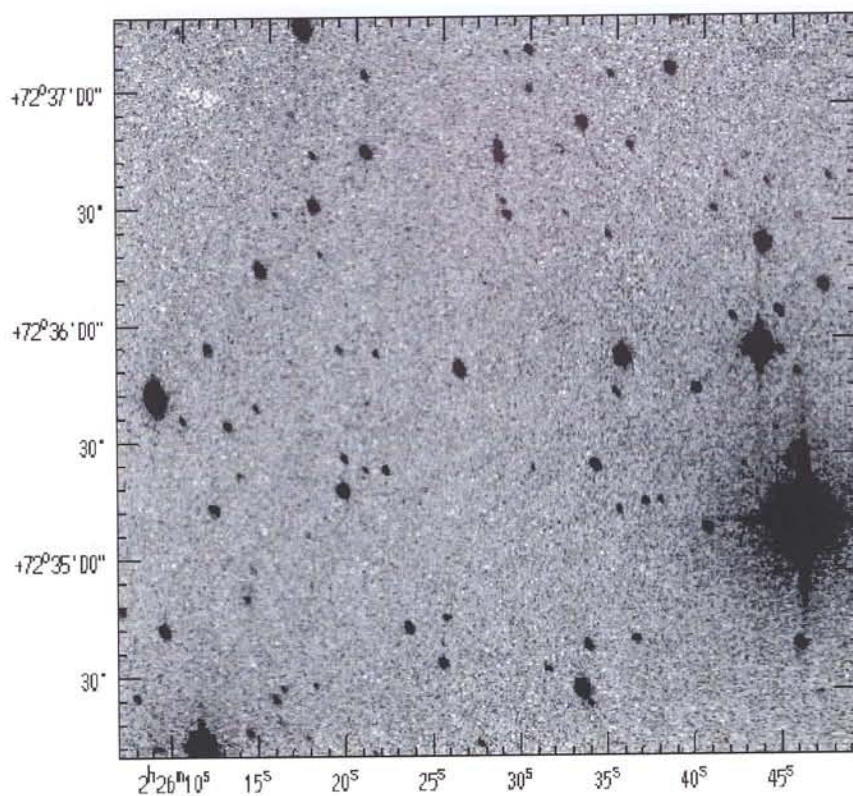


Figure 5.19: HH487 GunnZ Image

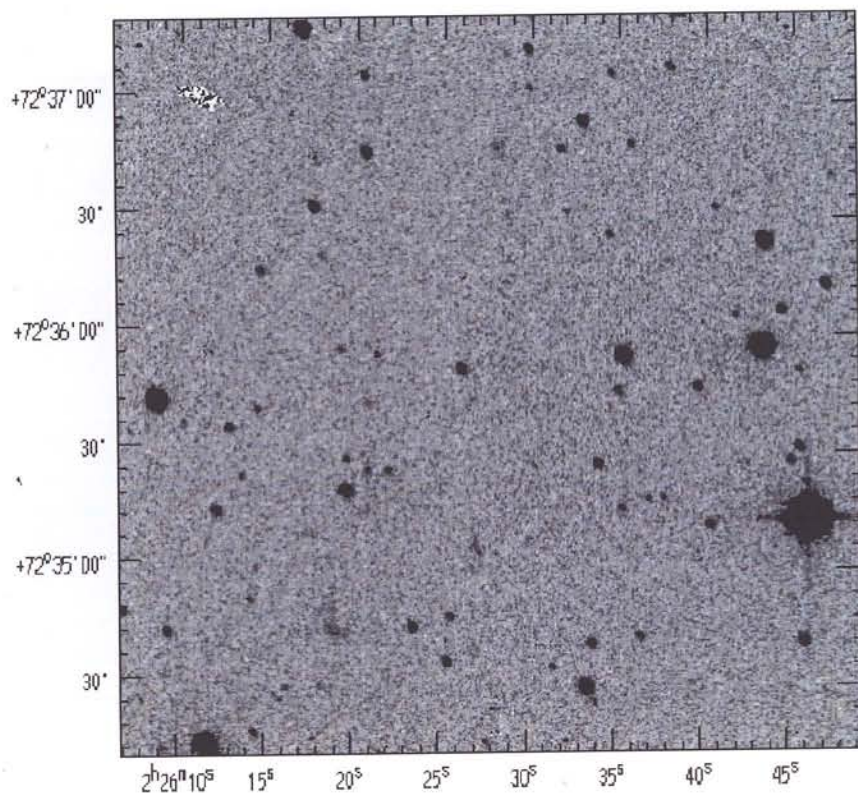


Figure 5.20: HH487 [SII] Image

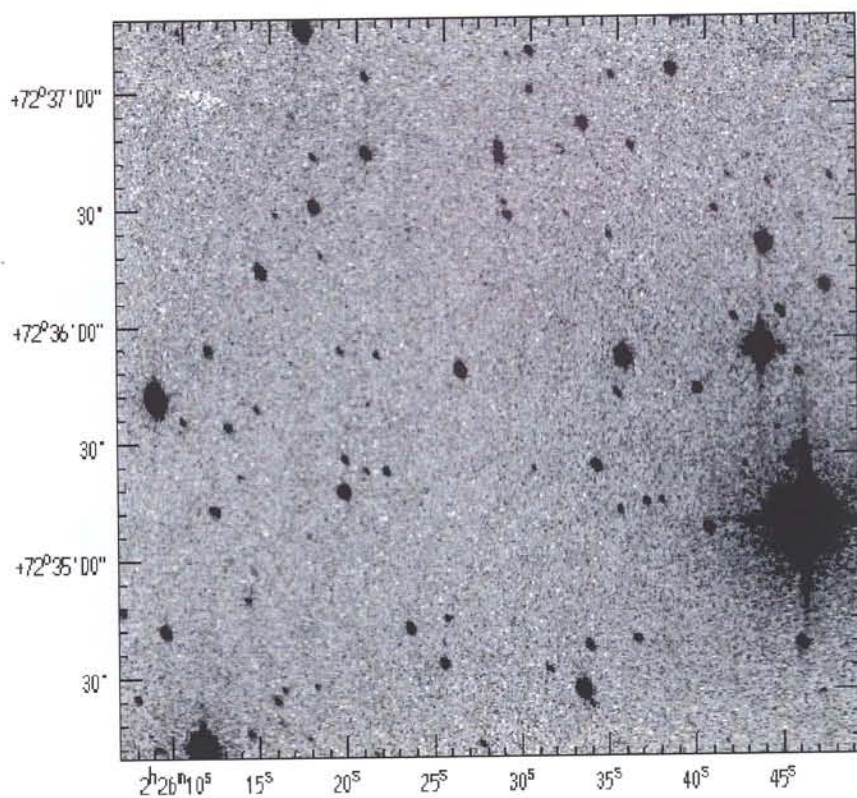


Figure 5.21: HH487 GunnZ Image

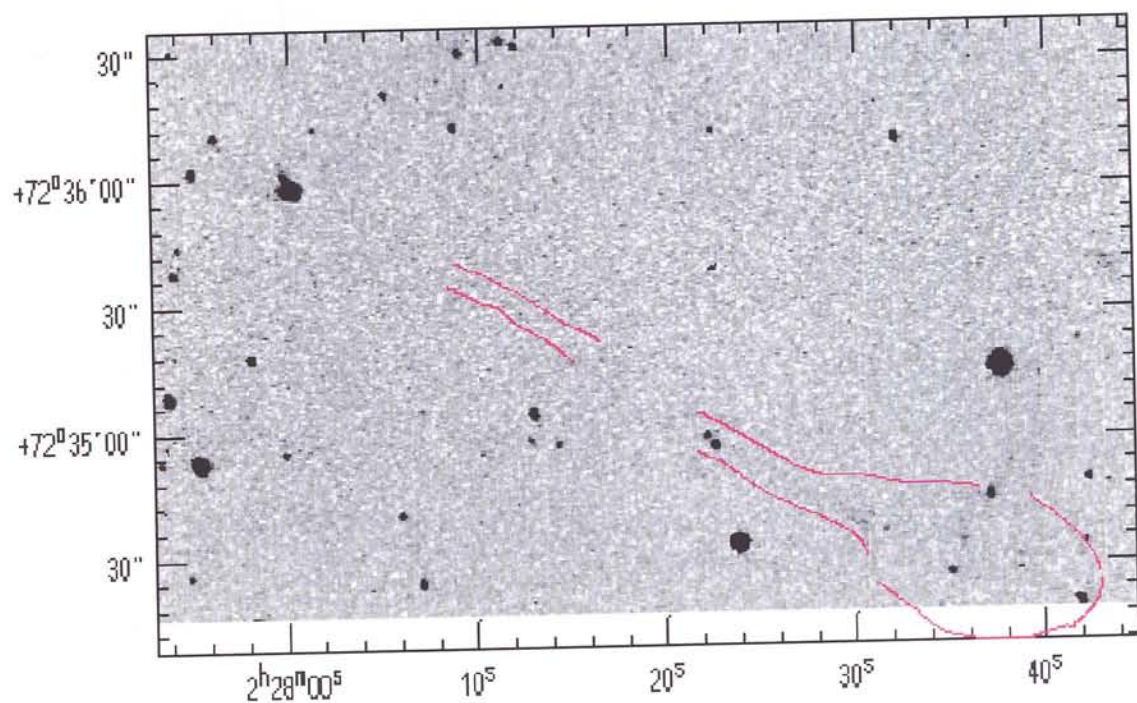


Figure 5.22: HH488 H $_{\alpha}$ Image. The lines mark the faint features of the long jet

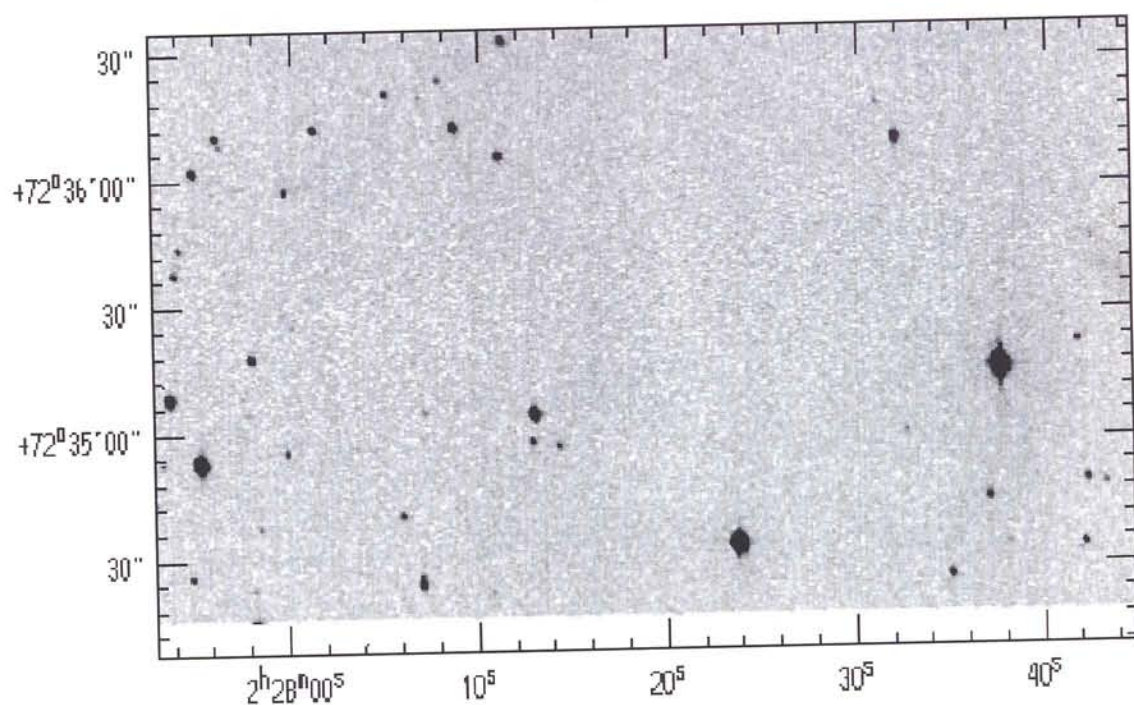


Figure 5.23: HH488 GunnZ Image

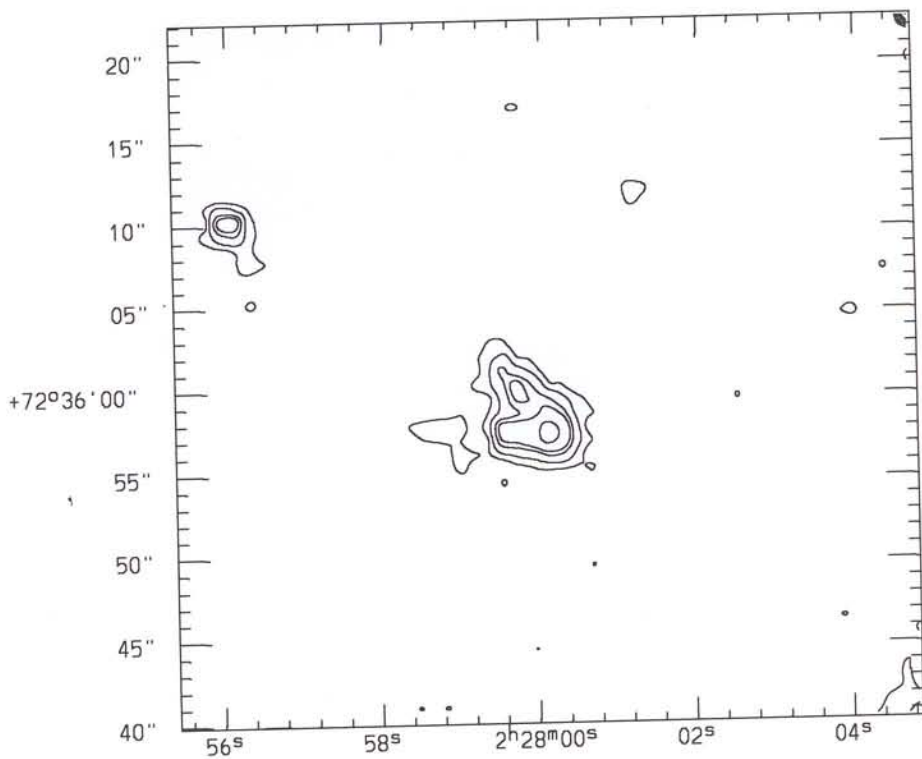


Figure 5.24: HH488 Driving source, [SII] contours

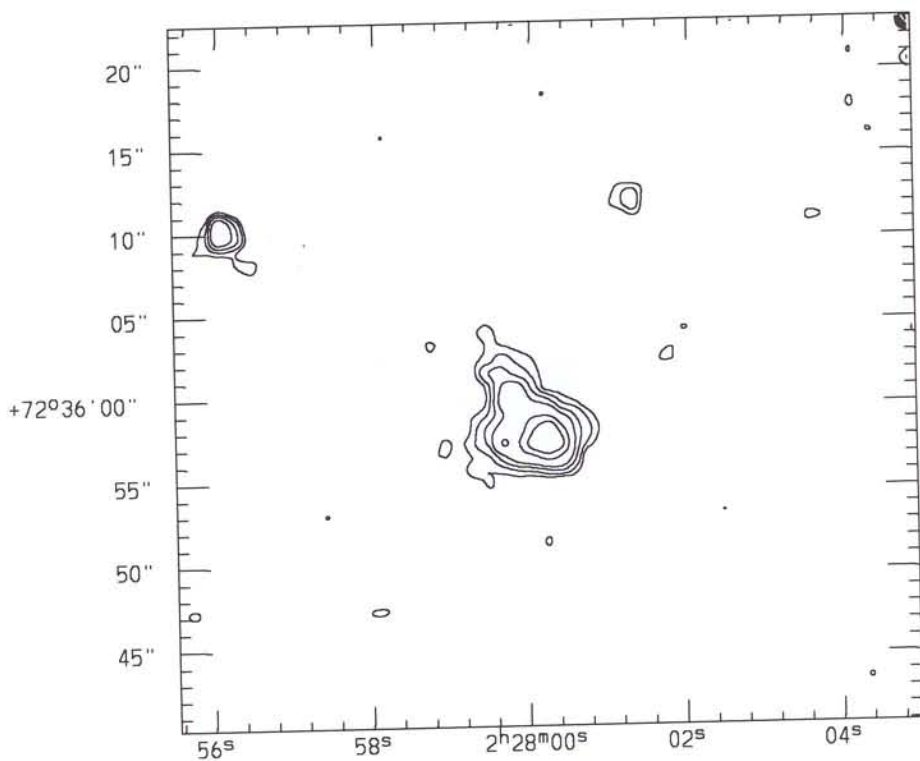


Figure 5.25: HH488 Driving source, H_{α} contours

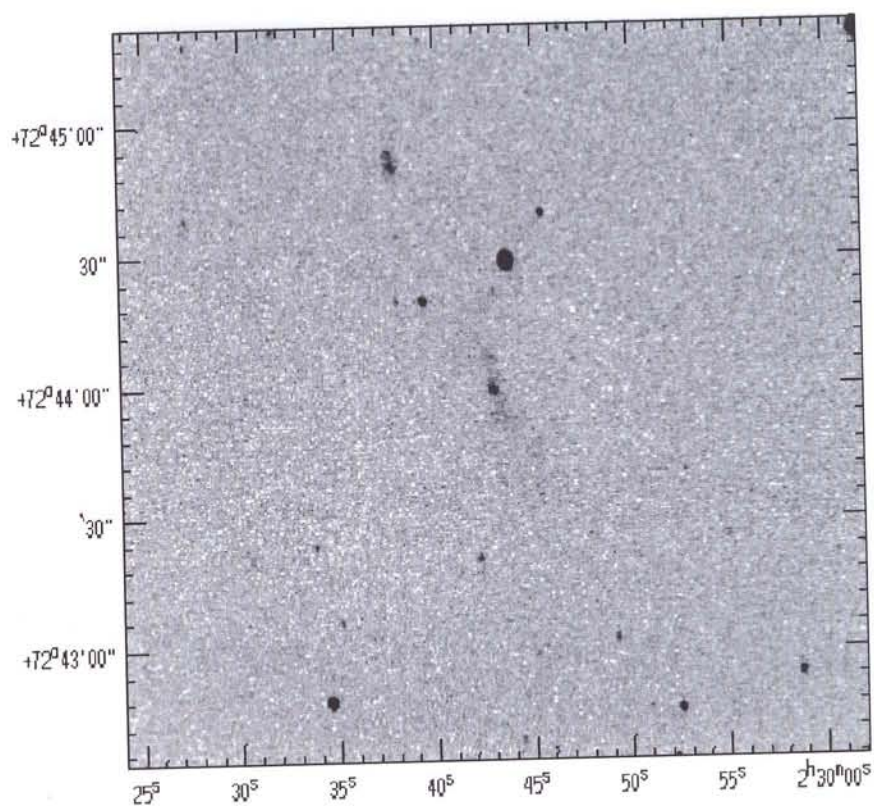


Figure 5.26: HH489 (H_{α} Image)

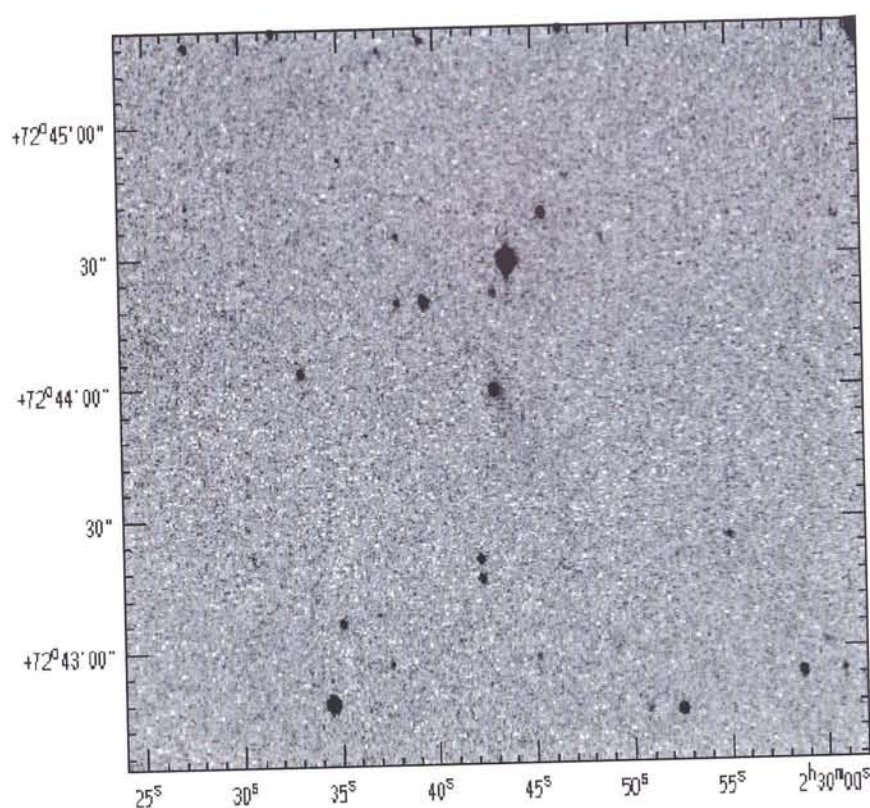


Figure 5.27: HH489 (GunnZ Image)

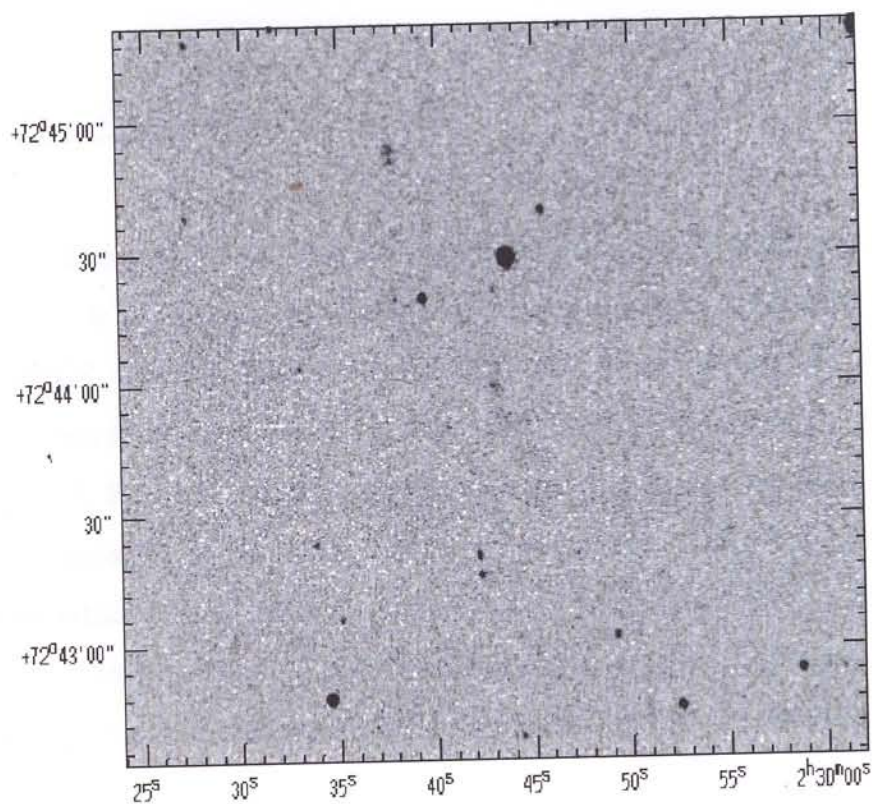


Figure 5.28: HH489 ([SII] Image)

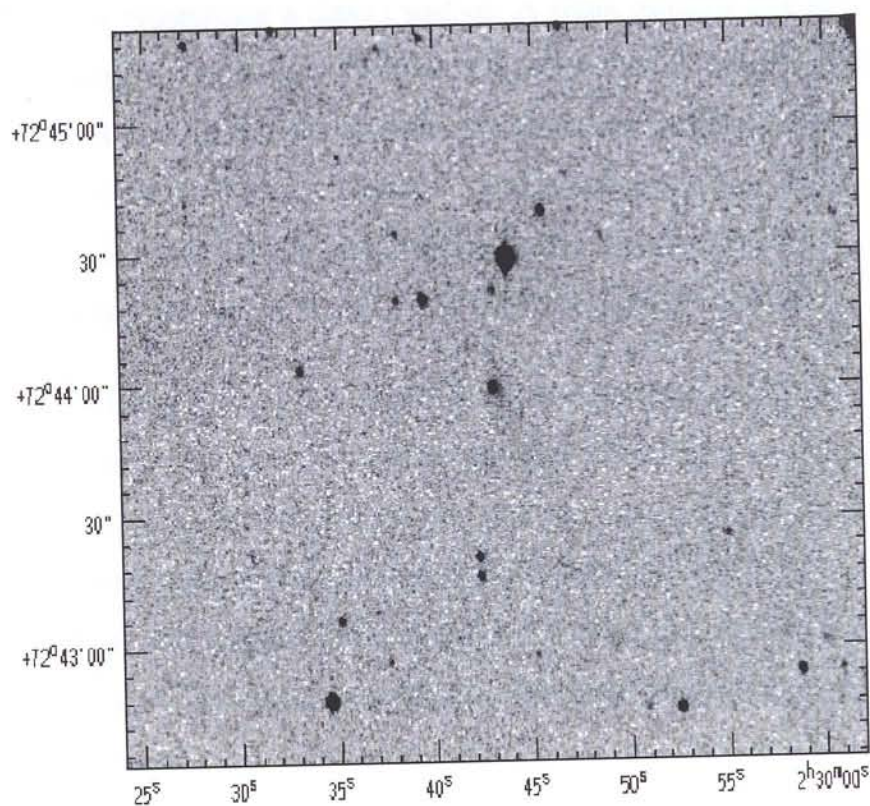


Figure 5.29: HH489 (GunnZ Image)

5.5 Conclusions

L1340 is a molecular cloud at high galactic latitude with a high rate of star formation activity. It consists of three dense cores that are associated with three Cohen's objects RNO7, 8 and 9. The cloud is shown (K94) to be forming both low and intermediate mass stars. Our optical and infrared images have made a clear association of the RNO7, 8 and 9 objects with the cores of this cloud. We identify that RNO7 is a young loose cluster of stars that is in the process of blowing off the molecular core from which it had formed. Although K94 identified RNO8 as the most interesting object in this cloud, it turns out that RNO8 is just a reflection nebula with a bipolar appearance that is possibly partly excited by a stellar wind from the central intermediate mass young star. RNO9 is associated with the densest core of L1340, namely core C and is the only region of L1340 that shows two component emission in the CO isotopic lines. Our K' image reveals an outflow candidate source that has IRAS fluxes suggesting a class I source. A weak outflow-like feature is seen in our infrared image that is not visible in the optical CCD images. Millimeter maps made around RNO9 region clearly show the double component emissions that are separated in velocities by $\sim 2\text{--}3 \text{ km s}^{-1}$. The relative absence of CS emission and weak C¹⁸O emission from the region along RNO9 clearly indicates that this region is not very dense and it is situated along the boundary of the core C.

The southern part of the L1340 cloud containing cores C and B are forming several low mass stars. We have discovered new HH objects in this region that are associated with three independent flows. This is a clear indication of on-going star formation activity. Two of the three identified flows (HH487, HH488), are suspected to be giant flows with typical dimensions of 1pc. A jet and 3 bowshock features are among the newly discovered HH objects. We have identified the sources of two flows HH488 and HH489, whereas the driving source of HH487 seems ambiguous. All the HH objects are lying along the boundary of the dense cores identified by molecular emission. These flows are excellent candidates for further deep imaging in the H α and [SII] lines.

5.6 References

- Bohm, K. H., & Goodson, A. P., 1997, in Reipurth, B and Bertout, C.,(eds) Herbig-Haro Flows and the Birth of Low Mass Stars, 47, IAU187, Kluwer Academic Publishers.
- Cohen, M., 1980, AJ, 85, 29
- Kun, M., Obayashi, A., Sato, F., Yonekura, Y., Fukui, Y., Blazs, L. G., Abraham, P., Szabados, L., & Kelemen, J., 1994, A&A, 292, 249 (K94)
- Kun, M., Wouterloot, J. G. A., & Toth, L. V., 1999, in poster proceedings, IAU Symposium on Astrochemistry, Cheju Islands, Korea.
- Reipurth, B., 1991, in Eds. Lada, C. J., & Kylafis, N., The Physics of Star Formation and Early Stellar Evolution, 497-538
- Reipurth, B., 1994, A general catalogue of Herbig-Haro objects, electronically published via [anaon.ftp](ftp://anaon.ftp.hq.eso.org) to [ftp.hq.eso.org](ftp://ftp.hq.eso.org), directory /pub/Catalogs/Herbig-Haro
- Lynds, B. T., 1962, ApJS, 7, 1
- Yonekura, Y., Dobashi, K., Mizuno, A., Ogawa, H., & Fukui, Y., 1997, ApJS, 110, 21

A Near Infrared Imaging Fabry-Perot Spectrometer

6.1 Introduction

Kinematics of star forming regions is one of the important studies of current interest. It helps in understanding the energetics of the outflows, their driving sources and other manifestations of star formation. Imaging spectroscopy is one of the most powerful tools to study kinematics of nebulous objects. The importance of Fabry-Perot spectrometers in studying Planetary Nebulae, interacting galaxies and HII regions in the optical wavebands is well known (Atherton et al. 1982, Bland and Tully 1989, Desai 1984, Anandarao and Banerjee 1988, Seema et al. 1992 Chakraborty and Anandarao 1999). Star forming regions, particularly low mass star forming regions emit weakly at optical wavelengths. However, they are the strongest emitters in the near-infrared region. Therefore, near-infrared Fabry Perot Spectrometers are essential to study the kinematics of star forming regions. This has been possible with the advent of the near-infrared focal plane arrays in the past one decade and there are only a few near-infrared Imaging FP Spectrometers operating in the world today (e.g. Krabbe et al. 1993, Satyapal et al. 1995, Ryder et al. 1998).

This chapter describes the construction, testing and performance of a Near-IR Imaging Fabry-Perot Spectrometer (NIRFPS) currently operative with the Infrared Camera of Gurushikhar 1.2m telescope at Mt. Abu, W. India. In this chapter,

a brief introduction to the essential theory of Fabry-Perot spectrometers, an evaluation of the different modes of operating them and finally, description of NIRFPS are given.

6.2 The Fabry-Perot Interferometer

A spectrometer is characterized by the parameter called *Throughput* or *etendue* ($= A\Omega$, where A is the spectrometer area and Ω is the acceptance solid angle of the spectrometer) which was first introduced by Jacquinot (1954, 1958) who made a comparative study of different spectrometers and showed that the product

$$L \times R = \text{Constant} \quad (6.1)$$

for a given type of spectrometer, where L is the luminosity ($= \epsilon A\Omega$, with ϵ as the spectrometer efficiency) and R is the resolving power of the spectrometer. Luminosity of the spectrometer is essentially a measure of the total light grasping efficiency in a single resolution element. Further, Jacquinot showed that this $L \times R$ product is much higher in the case of the Fabry-Perot spectrometer compared to other spectrometers. The only other spectrometer that shares this property with the FPS is the Michelson interferometer. This is because, the FP has a higher solid angle of light acceptance compared to a grating or any other spectrometer, for a given resolution. It is this property of FPS that makes it an ideal instrument to study kinematics of extended objects like star forming regions, planetary nebulae and galaxies. A detailed discussion and comparisons of different spectroscopic devices can be found in Meaburn (1976). It suffices to mention here that the advantage of an FP over other devices is as follows:

$$(L \times R)_{FP} \approx 30 - 100 \times (L \times R)_{grating} \approx 300 - 1500 \times (L \times R)_{prism} \quad (6.2)$$

Fabry-Perot Interferometer works on the principle of multiple beam interference and consists of two highly reflecting optically flat parallel plates (surface errors are better than $\lambda/100$). An incident ray of wavelength λ , impinging at an angle θ on the plates undergoes multiple reflection within the cavity of the parallel plates and the emerging beam forms an interference pattern that satisfies the condition,

$$n\lambda = 2\mu t \cos\theta \quad (6.3)$$

where t is the gap thickness between the parallel plates, μ the refractive index of the material between the plates (1 for air), and n is the order of interference. The intensity distribution of the resulting interference pattern is a plot of intensity vs wavelength called Airy Function represented by

$$I_{t,\theta,\mu} = I_\lambda T^2 [(1 - R)^2 + 4R(\frac{2\pi\mu t \cos\theta}{\lambda})]^{-1} \quad (6.4)$$

where I_λ is the maximum incident intensity at λ , T and R are the fractional transmission and reflection coefficients of the reflecting surfaces ($T + R = 1$ for negligible absorbance). This intensity distribution consists of periodically spaced peaks, separated by the *Free Spectral Range* (FSR) given by

$$\Delta\lambda = \frac{\lambda^2}{2\mu t} \quad (6.5)$$

The full width at half maximum (FWHM) ($\delta\lambda$) of the Airy Profile is given by

$$\delta\lambda = \frac{\Delta\lambda}{F_{eff}} \quad (6.6)$$

where the effective finesse F_{eff} is given by,

$$F_{eff}^{-2} = F_R^{-2} + F_D^{-2} + F_A^{-2} \quad (6.7)$$

with F_R , F_D , F_A as reflective finesse, defect finesse and aperture finesse respectively. The reflective finesse or simply finesse of the FP is defined as

$$F_R = \frac{\pi\sqrt{R}}{1 - R} \quad (6.8)$$

In practice, the finesse which is a measure of the resolving power of the FPS deteriorates due to several factors. The microscopic flatness and curvature defects of the FP plates, the parallelism errors of the plates (all these define F_D), and the effect of a finite aperture (defined by F_A) contribute to the broadening of the line profile, reducing the effective finesse. Excellent discussion of the detailed theory of Fabry-Perot Spectrometers can be found in the classics by Born & Wolf (1987), Meaburn (1976) and Vaughan (1989).

6.3 *Imaging Fabry-Perot Spectrometers*

Figure 6.1 shows a schematic of an IFPS in the classical configuration. The object in this case is a real image formed by a telescope. The rays from this image are collimated by a lens and passed through the FP etalon and re-imaged by the imaging lens. The ratio of the focal lengths of the collimator and imaging lenses will decide the magnification factor by which it is possible to expand or compress the original image. A set of concentric fringes is formed on the image plane. This fringe system acts like a window which allows a very narrow wavelength range from the original image. A pre-filter (order sorting filter) helps to isolate a narrow wavelength window of interest. For a given wavelength the different fringes represent different orders. The angular dispersion of the FP etalon is given by

$$\frac{d\lambda}{d\theta} = -\lambda \tan\theta \quad (6.9)$$

For a given gap setting " t " the fringe system schematically shown in Fig 6.1 is covering only parts of the image space covered by the fringes. However, changing

the etalon gap t by the modern servo-controlled, piezo-electric scanning will allow to cover the entire image space. This will result in a set of interferograms which will form a 3 dimensional data cube with two spatial dimensions and one spectral dimension.

6.3.1 Scanning and phase correction

In order to cover the entire spatial extent of an extended source, the etalon needs to be scanned by changing the cavity gap t . As the gap is changed in suitable steps, the diameter of the fringes keeps changing covering the spatial extent in its entirety. Then, the intensity variation on a single pixel at a given location (corresponding to a particular spatial position) will constitute the line profile at that location. This profile is a convolution of the FP instrument function with the object spectrum incident on that pixel. If $I_{x,y}(t)$ represents the intensity recorded by the detector at a particular pixel (x, y) and gap t , then for an etalon of finesse F ;

$$I_{x,y}(t) = (1 + \frac{4F^2}{\pi^2} \sin^2[2\mu t \cos\theta / \lambda])^{-1} \times F_{x,y}(\lambda) \quad (6.10)$$

where $F_{x,y}(\lambda)$ is the prefilter transmission function. Thus, for the central on-axis pixel (x_o, y_o) the maximum transmission at λ_o would occur for $t_o = n\lambda_o/2\mu$. For any off-axis pixel, a different wavelength λ will be transmitted at the same t which is separated in wavelength by

$$\delta\lambda_{x,y} = \lambda_o(1 - \cos\theta) \quad (6.11)$$

This is called a geometric phase factor and can be computed for any arbitrary pixel transmitted at a different value of t given by

$$t = t_o(\sec\theta - 1) = P_{x,y}a \quad (6.12)$$

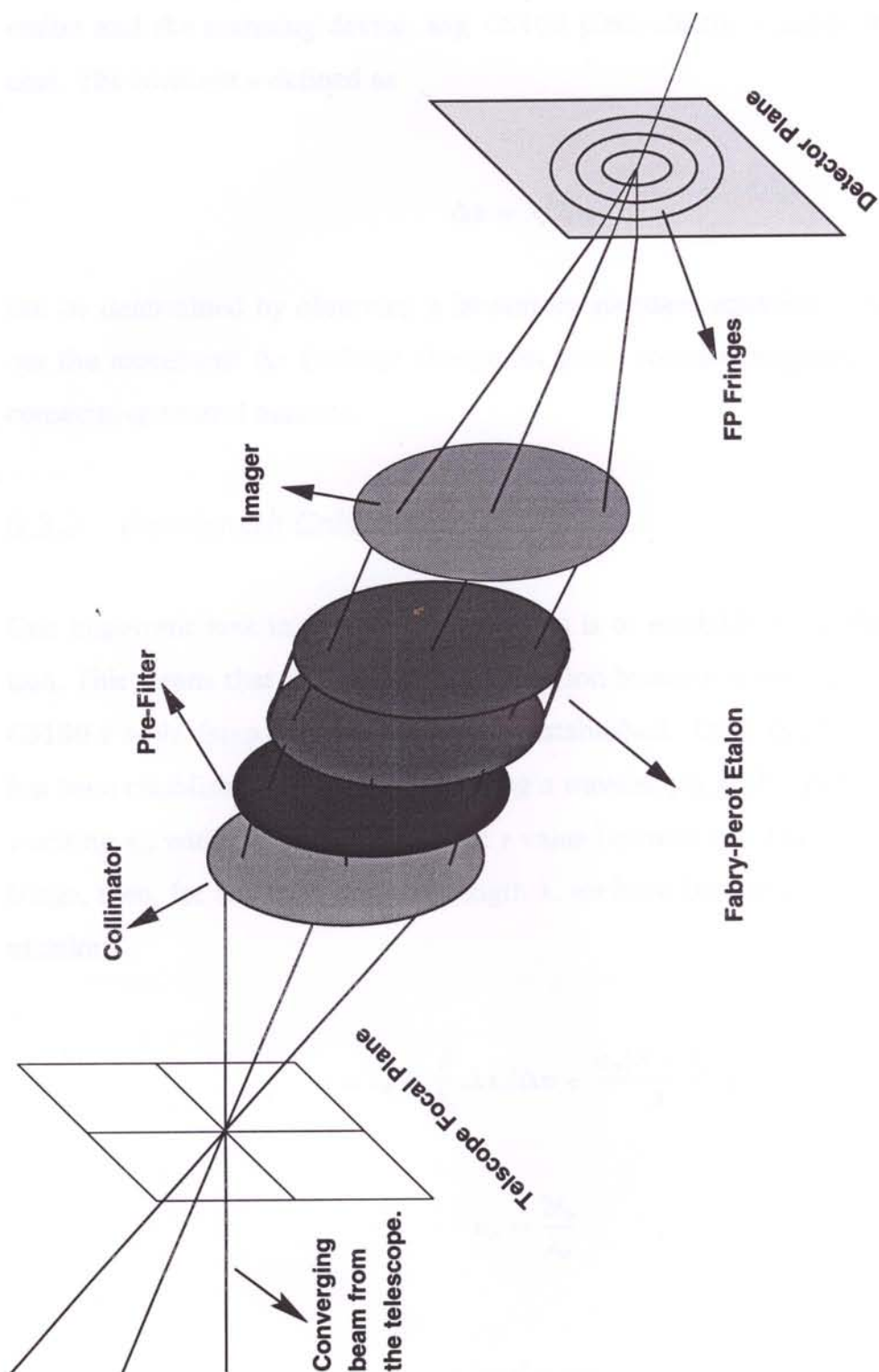


Figure 6.1: Imaging Fabry Perot Spectrometer in Classical Configuration

where $P_{x,y}$ is the phase factor at pixel x, y and a is a constant characteristic of the etalon and the scanning device, say, CS100 piezo-electric scanner in the present case. The constant a defined as

$$\Delta z = \lambda / 2\mu a \quad (6.13)$$

can be determined by observing a laboratory standard emission line, and finding out the movement Δz (voltage change for piezo scanner) required to obtain two consecutive central maxima.

6.3.2 Wavelength Calibration

One important task in the FPS observations is to establish a wavelength calibration. This means that a correspondance relation between wavelength scale and the CS100 z scale (step numbers) has to be established. Once the CS100 constant a has been established (see eqn 6.13), using a wavelength λ_o that peaks at the CS100 z -setting z_o , with Δz_o as the change in z value between two maxima of the central fringe, then, for any arbitrary wavelength λ , we have (Anandarao, private communication),

$$z = z_o + \frac{\lambda}{\lambda_o} \Delta z_o \left[\Delta n + \frac{n_o(\lambda - \lambda_o)}{\lambda} \right] \quad (6.14)$$

$$n_o = \frac{2t_o}{\lambda_o} \quad (6.15)$$

$$t_o = d + az_o \quad (6.16)$$

where d is the default spacing of the FP etalon, set and quoted by the manufacturer according to user specifications. The parameter Δn is the fractional order of the central fringe which is taken as 1 in the general case. Ideally, one should establish

this number by repeating the experiments with two appropriately spaced spectral lines and finding the difference $\Delta n = n - n_o$ where n and n_o are the orders of for any two wavelengths λ and λ_o .

6.4 *Astronomical Observations with an IFPS*

The following steps describe a standard sequence of observing with an Imaging Fabry-Perot Spectrometer operating in the classical configuration and in the optical wavebands. The following steps assume that the continuum levels of the program sources are much less compared to the emission line fluxes as in the case of Planetary Nebulae. The presence of a high level of continuum deteriorates the fringe contrast and hence the resolution due to leakage in the Airy profile wings.

- Obtain Standard Frames with a lab source before beginning observations on the program object. This is required to perform phase correction of the program source interferograms.
- Obtain interferograms on the program object. This involves obtaining N images at different gap settings where the minimum value of N is equal to the finesse of the FP etalon which is typically 20. Ideally N should be $2.3 \times \text{finesse}$ to have Nyquist criterion satisfied. It is assumed that the sky does not vary significantly during this procedure.
- Acquire Interferograms with a lab source at two different wavelengths for absolute wavelength calibration.

To complete this sequence of operation in one night on the sources of interest, a minimum of 2-4 m class telescopes are required. It is difficult or sometimes impossible to obtain FP data with smaller telescopes. This constrains observations to only relatively bright sources or to do a minimal sampling of one finesse. It is not possible even to see the full image on the detector unless one covers this minimal

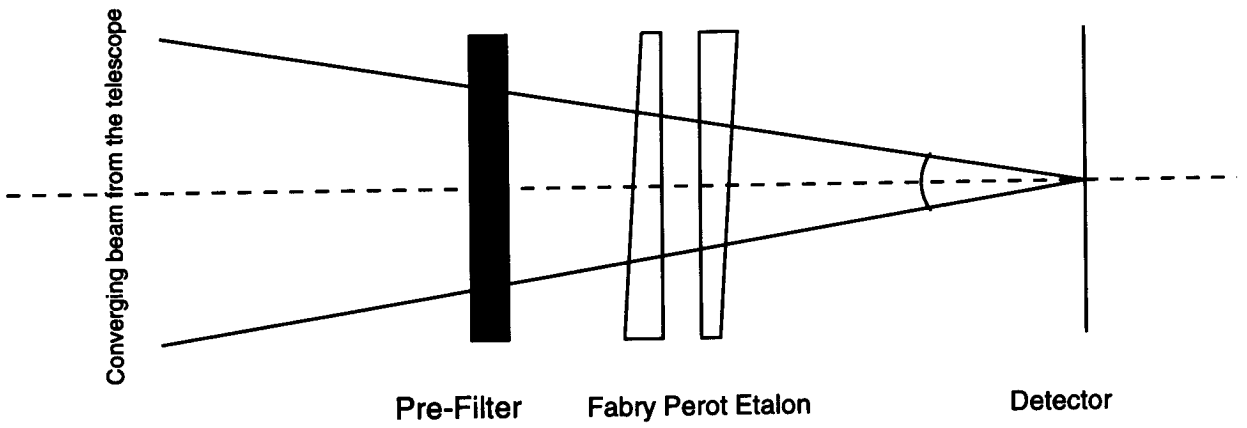


Figure 6.2: Telecentric Mode of Operation

sampling. It is in view of these practical difficulties that the telecentric mode of operation of the Fabry-Perot etalon becomes important.

6.5 Telecentric Configuration

Figure 6.2 shows the telecentric mode of operating an FP etalon. Unlike the classical mode this mode does not produce fringes on the detector plane. Instead the entire image is seen on the detector at any gap setting t (or equivalently at a particular λ) and the intensity of different pixels vary with scanning t that will result in a wavelength profile at each pixel. The FP etalon is simply inserted in the converging beam of the telescope and the FP acts as an extremely narrow band tunable filter. As described in Section 6.2, the $L \times R$ product for a given spectrometer is constant and so is the case for FPS. This imposes a limit on the acceptance solid angle ($\Omega \sim \theta^2$) for a FP etalon which is a function of the resolving power R alone and can be written as

$$\frac{\theta^2}{8} = \frac{1}{R} \quad (6.17)$$

Therefore, the acceptance angle θ plays an important role in the operation of the FP in telecentric mode. The resolving power of an FP depends upon its reflective

finesse and the free spectral range(FSR). However, in order to fully realize this resolving power, the incident beam should have a solid angle which is less than the acceptance solid angle defined by the equation above. If the solid angle of the incident cone of light is larger than the acceptance solid angle, the resulting resolving power is lesser than the actual resolving power of the FP etalon and can be computed by using the equation 6.17. While using the FP in the telecentric mode this criterion puts a constraint on the beam speed or the f-number of the telescope beam. Alternatively, the available f-number of the telescope beam decides the maximum resolving power of the FP. Generally the resolving power available with the commonly used f-numbers are between 300-1000. This is not very useful to make detailed kinematic maps as in the case of classical configuration, but remains a powerful technique in practice for reasons discussed below.

6.6 *Telecentric vs Classical Configuration*

The main concern in imaging spectroscopic observations is to obtain a reasonable S/N ratio over the required spectral coverage in a limited time of one night. In the classical mode of operating the FP, the etalon needs to be scanned by changing the cavity gap to cover the entire spatial extent of an extended source. As the gap is changed in suitable steps, the diameters of the fringes keep changing providing the spectral and spatial coverage. Now, the intensity variation with step size at any single pixel will constitute the line profile corresponding to that particular spatial position. The phase variation of the line profile across the field of view is then determined by using a standard laboratory source. During the observations at the telescope, this calls for obtaining images at 40-50 steps(gap settings) of the FP (for a nominal finesse of 20-25). Given the problems of large sky background in the infrared, that requires sky subtraction for every frame, the time factor gets doubled which makes the procedure equivalent to obtaining images at 80-100 steps.

In the telecentric mode, since the image is formed by the converging beam directly on the array, one can dispense with the statutory phase correction required

due to the non-linear dispersion of the etalon. Hence, it suffices to obtain images only at 5-10 steps around the spectral line of interest to which the FP is tuned (see *Section 5*) and still get what is required. This infact gives more than one Nyquist sampling in the spectral domain. Considering the sky subtraction factor, the total time amounts to obtaining images at 10-20 steps, which is a factor of 5 smaller compared to the classical mode. It is therefore highly advantageous to use the telecentric mode while operating FPS in the infrared at moderate resolutions. Another important advantage of the telecentric mode is the relatively simple data reduction procedure that can be carried out using regular CCD processing routines in the astronomical image processing softwares like IRAF or MIDAS. Analysis of the data obtained in the classical mode requires specially written software packages like the one used for TAURUS (Atherton et al. 1981).

6.7 *PRL Infrared FP Etalon*

The manufacturer-quoted parameters of the PRL near-infrared FP etalon are summarized in Table 6.1. It is coated to perform best in the $2\text{-}2.5\mu\text{m}$ region. Infrared etalons transmit very little in visible and therefore one can not see through the etalon easily to identify fringes, like in the case of optical etalons. However, our experience shows that the Helium spectral lamp has some strong emission lines that pass through different orders and form reasonably sharp fringes that can be seen visually. In fact, the etalon coating is such that there exist a few broad-band low transmission windows in the visible. However, this is of great help while doing parallelism adjustments.

The scanning of the FP etalon is done by the computer generated pulses fed through a RS232 interface in to the servo-control system CS100 (Queensgate, UK). The scanning step size and the scanning length can be chosen through the computer. At each step of the scanning the signal can be integrated for a chosen time. Typically a total of 135 steps of scanning are required to cover one FSR which is $0.0225\mu\text{m}$ at $2.121\mu\text{m}$ for the present case. Each such step effects a gap

Table 6.1: Manufacturer-quoted parameters of the PRL IRFP

Usable aperture	50 mm
Wavelength range	2 - 2.5 μm
Reflectivity	95%
Free spectral range (FSR)(at 2.2 μm)	0.02 μm (3000 km s^{-1})
Resolving power ($\lambda/\delta\lambda$)	5000
Velocity resolution	60 km s^{-1}
Resolution($\delta\lambda$)	$4 \times 10^{-4} \mu\text{m}$

change of $1.67 \times 10^{-4} \mu\text{m}$ corresponding to a Doppler velocity resolution of 23.6 km s^{-1} . The FWHM of the instrumental function was measured to be $\delta\lambda = 0.0014 \mu\text{m}$ or 212 km s^{-1} in Doppler velocity having a sampling of 9 steps. A finesse of 16 has been realised with this mode of operation. By decomposing the profiles using gaussian fitting (Anandarao & Rao 1985) it is possible to resolve features separated by around 90 km s^{-1} in cases of high S/N ratios. In such cases a resolving power of about 2500-3000 can be achieved.

6.7.1 Characterization

The FP needs to be adjusted for parallelism before inserting into its chamber. Although the parallelism adjustments are made by using pre-determined standard CS100 settings, it is possible to make a quick confirming test before starting the night observations. A simple technique by which one can adjust the parallelism to a very good extent is by visually looking at the fringes formed by using a standard Helium source. The thumb rule is that, if the etalon is perfectly parallel, the fringe pattern should remain steady when one scans with the eye across the etalon face in two orthogonal directions.

The characterization test for the telecentric mode is different from the conventional classical configuration. As described in Section 2.4 the resolution of the FP is decided by the acceptance angle and therefore on the telescope f-number. Characterization of the FP involves determining a few parameters in operating conditions.

Table 6.2: PRL IRFPS parameters in telecentric mode

Free spectral range (FSR)	$0.0225\mu\text{m} (\sim 3000\text{km s}^{-1})$
Instrument FWHM ($\delta\lambda$)	$0.0014\mu\text{m}$
Finesse	16
Resolving power ($\lambda/\delta\lambda$)	2500
Velocity resolution	212km s^{-1}

To do this, it is possible to artificially generate a beam similar to the telescope beam and perform these tests. Alternatively, the tests can be done in real time observing conditions; i.e., FPS attached at the back-end of the telescope along with the IR camera. This is the best way since it would simulate real time conditions and will show up problems related to alignment and that of ghosting due to internal reflections if any. The FP etalon was mounted in its chamber at the telescope after parallelism adjustments were made. The aim was to determine the effective parameters of the spectrometer namely FSR, finesse and CS100 etalon constant. The telescope was pointed to the flat-fielding screen which was illuminated with a Krypton lamp source. Images were acquired with appropriate integration time (typically 1-2sec) at each scanning step while keeping all external conditions constant. The FP is scanned between extreme limits that can be achieved using the CS100 controller. Table 6.3 is a summary of the resulting parameters in the telecentric mode with the Gurushikhar 1.2m telescope.

6.7.2 *Tuning of the FP*

Once the emission line of interest is chosen, the appropriate pre-filter is brought to position inside the camera and the FP is tuned to the line of interest. It is customary to adjust the CS100 z dial settings to the standard values that are pre-determined in the laboratory. We have found that this laboratory calibration has remained stable to an accuracy of less than one step in more than 3 months. However, in cases where it is required to do the tuning from scratch, the following method maybe adopted. The telescope is aimed at the flat-fielding screen illuminated with a Krypton lamp

and the FP is scanned until the Krypton line ($2.1165 \mu\text{m}$) peaks up. This can be done by setting the camera into movie mode (continuous display) and monitoring the mean counts of the frames. Now, since the relation between any wavelength and the Krypton line known by laboratory experiments, the same can be used to compute the required CS100 z settings. A short cut to this procedure is possible if a bright planetary nebula or an HII region like the Orion nebula is available in the sky during observations. For example, z values at which emission lines like H_2 and $\text{Br}\gamma$ will peak-up can be found in less than 2-3 minutes with a 1.2 m telescope using Orion nebula. This technique works well for resolving powers of upto 2000 which is equivalent to about 150 km s^{-1} since the velocity dispersion in these nebulae are not more than this value. Most IRFP's operative elsewhere today are used at resolving powers in this range and for the purpose of very narrowband imaging. It is therefore practical to use simpler calibration procedures as described above. For instance, the H_2 S(1) line from Orion peaks at step number 67 and 200 with the PRL IRFP control software, while scanning at the 192 step resolution.

6.8 *Observations and data analysis*

Once the FP is tuned to an appropriate line, it is required to obtain images at different gap settings of the FP, spaced equally around the line. Although a minimum of 3 steps will suffice the purpose, the choice of the total number of steps is left to the observer and depends on the type of the object. An object and a sky frame has to be obtained for each FP setting. The median-combined sky frames at each FP setting form the respective flat frames. The data is reduced using standard CCD processing routines like CCDPROC of IRAF. Reducing the frames at each FP setting will result in a stack of images that form a data cube. The data cube consists of the XY plane of the image and a Z dimension which is the image number (wavelength). The Z dimension is the spectral dimension and the pixel-to-pixel variation across this dimension gives the wavelength profile. Preliminary observations were carried out using the 1.2 m Gurushikhar Infrared Telescope Facility (GIRT) at Mt.

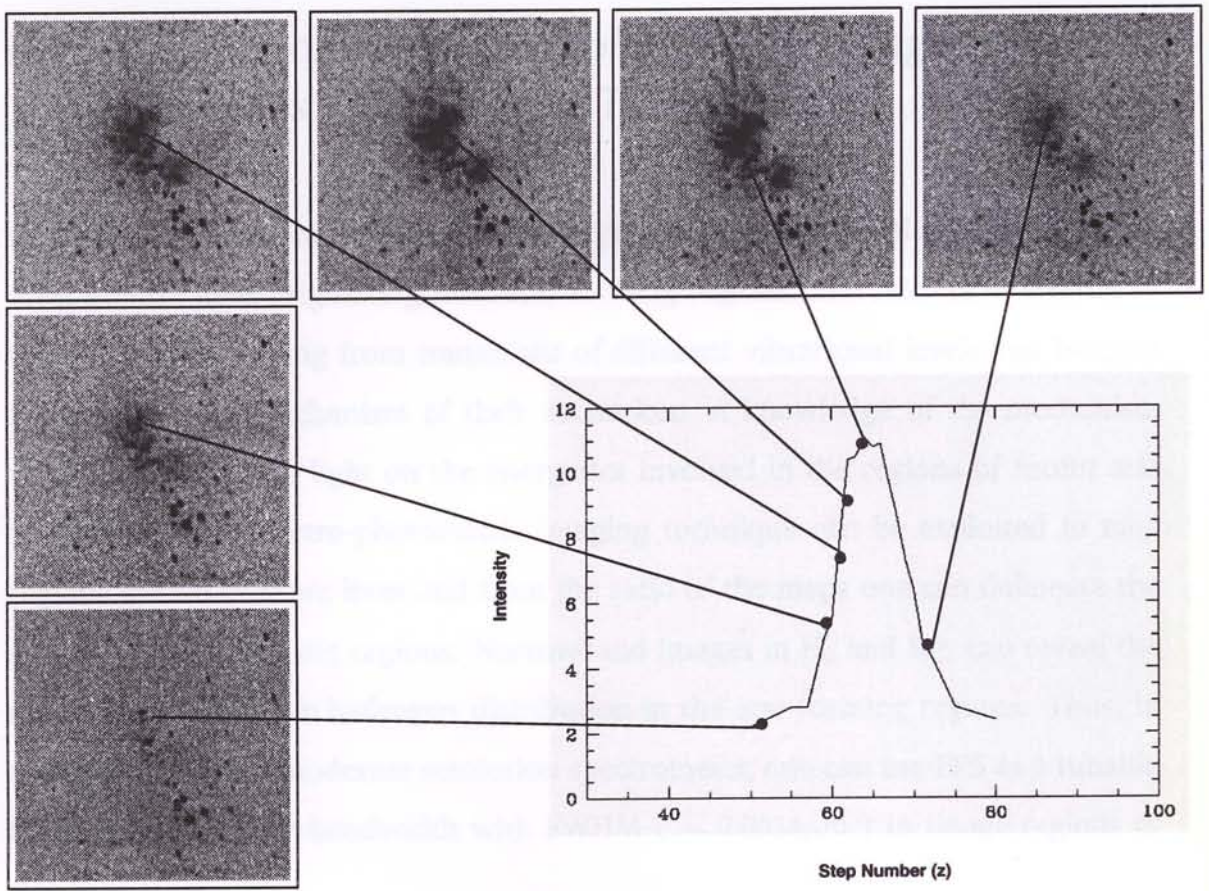


Figure 6.3: Orion Nebula through different steps of PRL IRFP

Abu. We have imaged a $4' \times 4'$ region centered on the well known BN-KL region of the Orion nebula. Fig 6.3 shows the resulting images at different steps of the etalon gap. One can notice the brightening of the nebular matter emitting the $v = 1-0$ S(1) vibrational transition of molecular hydrogen at $2.121 \mu\text{m}$ as the etalon gets gradually tuned to the emission line by the process of scanning. Using the line profiles obtained on this source we estimate a finesse of 16, that reconfirms our result obtained with laboratory standard spectral source.

6.9 *High-Resolution Spectrophotometric Imaging in Emission Lines - NIRFPS as a Tunable Filter*

Near-infrared emission lines of the hydrogen atom and molecule are some of the most intense lines originating from star forming regions. The ratio of intensities of molecular lines arising from transitions of different vibrational levels can be used to recognise the mechanism of their excitation. A knowledge of the mechanism would in turn throw light on the energetics involved in the regions of recent star formation. The spectro-photometric imaging technique can be exploited to map regions in two or more lines and from the ratio of the maps one can delineate the shocked/UV fluorescing regions. Narrowband images in H_2 and $Br\gamma$ can reveal the molecular and atomic hydrogen distribution in the star forming regions. Thus, in addition to being a moderate resolution spectrometer, one can use FPS as a tunable filter of very narrow bandwidth with FWHM ($\sim 0.0014\mu m$) to image regions of star formation.

Depending on the typical line width from the source and the resolving power of the FPS, it is required to obtain one or two images to form a narrowband image. If the FWHM of the FPS is comparable to or smaller than the source line widths, then a single image with a good wavelength centering will form a narrowband image. If the FWHM of the FP is much larger than the source linewidths then it is required to obtain two images to produce a good narrowband image. One image with the FP tuned to the on-line wavelength and another by detuning the FP to an off-line wavelength. The difference image results in a continuum-subtracted line image. Continuum-subtraction is a difficult and relatively inaccurate procedure while doing with conventional narrowband filters. But the Fabry-Perot technique gives a better way of subtracting the continuum. This is due to the fact that FP provides exactly the same filter profile (in shape and transmission) both at the on-line and off-line wavelengths unlike the interference filters that can have different shapes and transmissions for on-line and off-line bands. Also the FPS has a great advantage while imaging the close environments of young stars, where the regions

of interest are highly contaminated by the continuum emission from the star. The extremely narrow bandwidth of the FPS can select the emission line of interest critically and reject the continuum very efficiently. For this reason, the FPS is very useful even while studying jets that are seen tracing all the way upto the stellar seeing disk. The technique is also very useful in making accurate observations of galaxies with closely-spaced adjacent redshifts.

6.10 References

- Anandarao, B. G., & Banerjee, D. P. K., 1988, *A&A*, 337,253
- Anandarao, B. G., & Rao, S. R., 1985, *BASI*, 14, 34
- Atherton, P. D., Reay, N. K., Ring, J., & Hicks, T. R., 1981, *Opt.Engg.*, 20,806
- Atherton, P. D., Taylor, K., et al. 1982, *MNRAS*, 201,661
- Born, M., & Wolf, E., 1987, *Principles of Optics*, 6th Edition, Pergamon Press.
- Bland, J., and Tully, B., 1989, *AJ*, 98,723
- Chakraborty, A., & Anandarao, B. G., 1999, *A&A*, 346, 947
- Desai, J. N., 1984, *Proc. Indian Acad. Sci.*, (Earth Planet Sci.) 93, 189
- Jacquinot, P., 1954, *J. Opt. Soc. America.*, 44, 761
- Jacquinot, P., 1958, *J. Phys. Rad.*, 19, 223
- Luhman, M. L., Jaffe, D. T., Keller, L. D., & Pak, S., 1995,107,184
- Krabbe, A., Rotaciuc, V., et al. 1993, *PASP*, 105, 1472
- Meaburn, J., *Detection and Spectrometry of Faint Light* (Dodrecht, Reidel)
- Persson, S. E., Geballe, T. R., & Baas, F., 1982, *PASP*, 94, 381
- Ryder, S. D., Ashley, M. C. B., Sun, Y. S., Burton, M. G., Allen, L. E., Storey, J. W. V., 1998, *PASA*, 15, 228
- Shull, J. M., & Beckwith, S., 1982, *ARA&A*, 20, 163
- Satyapal, S., Watson, D. M., et al. 1995, *ApJ*, 448, 611
- Seema, P., Anandarao, B. G., et al. 1992, *PASP*,104, 1091
- Vaughan, J. M., 1989, *The Fabry-Perot Interferometer*, Adam Hilger Series on Optics and Optoelectronics, Bristol, England.

Epilogue

This thesis is an outcome of our efforts to start a viable programme on low mass star formation studies at Physical Research Laboratory. The acquisition of the country's first Near-Infrared Camera by PRL (PRLNIC), based on the NICMOS3 concept, made it possible to begin our programme. In this context, myself and Anandarao initiated the studies on low mass star formation that are among the brightest sources in the sky and an ideal topic to pursue with a small telescope like that of 1.2m Gurushikhar telescope (GIRT). This pursuance also had the background of our prior interest in star formation studies, in particular, those carried out by Raju et al. (1993), Seema (1994), Chakraborty and Anandarao(1997, 1999) using Fabry-Perot techniques in the optical wavelengths. A new FP etalon that was purchased by the division was awaiting to form an instrument for the future that would operate with the Infrared Camera. The construction of this instrument, namely, a Near-Infrared Fabry-Perot Spectrometer (NIRFPS) has been completed during this period (Anandrao et al. 1999).

Naturally, our research was aimed at the current problems in low mass star formation and therefore, the outflows and disks associated with young stars were our prime targets. We started with an optical survey for new Herbig-Haro objects with the 2.3m Vainu Bappu Telescope at Kavalur in 1997 that yielded positive results in L1340 dark cloud and further studies were pursued at KPNO, USA that was made possible by Bo Reipurth. We discovered HH487,488 and 489 in L1340. The NIR camera on GIRT was used to study L1340 in the near-infrared. Meanwhile, outflow candidates that were to be studied solely in NIR bands were chosen and observed with the PRLNIC at Gurushikhar. RNO 91 was among the first of those objects, that has opened up several projects to be continued in the future. We detected

extended shocked molecular hydrogen in the midst of a cold protostellar envelope using our PRLNIC grating spectrometer. Narrowband images of RNO 91 were obtained with IRCAM3 on UKIRT in a collaborative program with Chris Davis, and the results of the work were summarized in a paper by NandaKumar et al. (1999). The narrowband imaging of RNO 91 clearly resulted in the realization that it is impossible to make a good continuum-subtracted image in cases like that of RNO 91 where more than 80% of the light is continuum. This has opened up a challenging and "appropriate" project for our new instrument NIRFPS.

The work on RNO 91 immediately brought to our notice that there exists disk structures in the cold envelopes (Weintraub et al. 1994) too, which are common and have a host of questions that need to be answered. Several other objects also have properties similar to RNO 91 and therefore we found there exists an important sample of objects that are useful in studying the disks. The heirarchy of disks is an important aspect in the studies of star formation and therefore we went on to study the classical Keplerian disks also, in connection with the new "Cold Disks" that we found. At this juncture, came in the results of Dutrey et al. (1996) of imaging the Keplerian disks in the millimeter emission with the upgraded IRAM interferometer. The work of Greene and Meyer (1995) and Greene and Lada (1998) had demonstrated the power of infrared spectroscopy to study circumstellar disks and was also an ideal project that could be carried out on a 1m class telescope. We therefore chose a sample that would result in a comparative study of hot and warm disks for which multiwavelength information could be made available, although a subset of the sample still needs to be observed in the coming observing season.

These efforts have finally resulted in a set of ongoing and new projects to study the hierarchy of disks, to understand the cold disks and their connection with the warm and hot disks, and to study poorly collimated outflows like RNO 91 which may have an important relation to cold disk structures in protostellar environments.

References

- Anandarao, B. G., NandaKumar, M. S., et al. 1999, Submitted to BASI.
- Chakraborty, A., & Anandarao, B. G., 1999, A&A, 346, 947
- Chakraborty, A., & Anandarao, B. G., 1997, A J, 114, 1576
- Dutrey, A., Guilloteau, S., Duvert, G., Prato, L., Simon, M., Schuster, K., & Menard, F., 1996, A&A, 309, 493.
- Greene, T. P., & Meyer, M. R., 1995, ApJ, 450, 233
- Greene, T. P., & Lada, C. J., 1996, AJ, 112, 2184
- NandaKumar, M. S., Anandarao, B. G., & Davis, C. J., 1999, A&A, 344, L9
- Raju, K. P et al. 1993, ApSS, 39, 1
- Seema, P., 1994, Ph D Thesis, M. S. University, Baroda, India
- Weintraub, D. A., Tegler, S. C., Kastner, J. H., & Rettig, T., 1994, ApJ , 423, 674

List of Publications

1. Shocked Molecular Hydrogen from RNO91

M. S. Nanda Kumar, B. G. Anandarao, C. J. Davis, 1999, A&A, 344, L9-L12

2. NIFS: A near-IR Imaging Fabry-Perot Spectrometer

B. G. Anandarao, M. S. Nanda Kumar, 1999, to be submitted to BASI.

3. L1340: A multiwavelength Study

M. S. Nanda Kumar, B. G. Anandarao, & Kachun Yu, 1999, To be submitted to AJ.

4. 2-2.5 μ m spectra of T Tauri stars with Keplerian disks

M. S. Nanda Kumar, B. G. Anandarao, 1999, in preparation.

5. Near Infrared Studies of Jets and Outflows from Young Stars

M. S. Nanda Kumar, B. G. Anandarao, 1999, Bull.Astron.Soc.India, Proceedings of the XIXth Astronomical Society of India Meeting.

6. Star formation studies with a Large Telescope

B. G. Anandarao, M. S. Nanda Kumar, 1999, Bull.Astron.Soc.India, Proceedings of the XIXth Astronomical Society of